TIME-DOMAIN BASED FINITE DIFFERENCE TECHNIQUE AND ITS APPLICATIONS TO ELECTROMAGNETIC PROBLEMS

By 56

Mousa Issa M. Hussein

A Thesis
Submitted to the Faculty of Graduate Studies
in Partial Fulfilment of the Requirements
for the Degree of

Doctor of Philosophy

Department of Electrical and Computer Engineering
University of Manitoba
Winnipeg, Manitoba, Canada 1995

©Mousa Issa M. Hussein 1995

National Library of Canada

Acquisitions and Bibliographic Services Branch

395 Wellington Street
Ottawa, Ontario
K1A 0N4

Bibliothèque nationale du Canada

Direction des acquisitions et des services bibliographiques

395, rue Wellington
Ottawa (Ontario)
K1A 0N4

Your file *Votre référence*

Our file *Notre référence*

The author has granted an irrevocable non-exclusive licence allowing the National Library of Canada to reproduce, loan, distribute or sell copies of his/her thesis by any means and in any form or format, making this thesis available to interested persons.

L'auteur a accordé une licence irrévocable et non exclusive permettant à la Bibliothèque nationale du Canada de reproduire, prêter, distribuer ou vendre des copies de sa thèse de quelque manière et sous quelque forme que ce soit pour mettre des exemplaires de cette thèse à la disposition des personnes intéressées.

The author retains ownership of the copyright in his/her thesis. Neither the thesis nor substantial extracts from it may be printed or otherwise reproduced without his/her permission.

L'auteur conserve la propriété du droit d'auteur qui protège sa thèse. Ni la thèse ni des extraits substantiels de celle-ci ne doivent être imprimés ou autrement reproduits sans son autorisation.

ISBN 0-612-13203-X

Canada

Name _____

Dissertation Abstracts International is arranged by broad, general subject categories. Please select the one subject which most nearly describes the content of your dissertation. Enter the corresponding four-digit code in the spaces provided.

Electronics and Electrical
SUBJECT TERM

0544
SUBJECT CODE

U·M·I

Subject Categories

THE HUMANITIES AND SOCIAL SCIENCES

COMMUNICATIONS AND THE ARTS
Architecture 0729
Art History 0377
Cinema 0900
Dance 0378
Fine Arts 0357
Information Science 0723
Journalism 0391
Library Science 0399
Mass Communications 0708
Music 0413
Speech Communication 0459
Theater 0465

EDUCATION
General 0515
Administration 0514
Adult and Continuing 0516
Agricultural 0517
Art 0273
Bilingual and Multicultural 0282
Business 0688
Community College 0275
Curriculum and Instruction 0727
Early Childhood 0518
Elementary 0524
Finance 0277
Guidance and Counseling 0519
Health 0680
Higher 0745
History of 0520
Home Economics 0278
Industrial 0521
Language and Literature 0279
Mathematics 0280
Music 0522
Philosophy of 0998
Physical 0523
Psychology 0525
Reading 0535
Religious 0527
Sciences 0714
Secondary 0533
Social Sciences 0534
Sociology of 0340
Special 0529
Teacher Training 0530
Technology 0710
Tests and Measurements 0288
Vocational 0747

LANGUAGE, LITERATURE AND LINGUISTICS
Language
- General 0679
- Ancient 0289
- Linguistics 0290
- Modern 0291

Literature
- General 0401
- Classical 0294
- Comparative 0295
- Medieval 0297
- Modern 0298
- African 0316
- American 0591
- Asian 0305
- Canadian (English) 0352
- Canadian (French) 0355
- English 0593
- Germanic 0311
- Latin American 0312
- Middle Eastern 0315
- Romance 0313
- Slavic and East European 0314

PHILOSOPHY, RELIGION AND THEOLOGY
Philosophy 0422
Religion
- General 0318
- Biblical Studies 0321
- Clergy 0319
- History of 0320
- Philosophy of 0322

Theology 0469

SOCIAL SCIENCES
American Studies 0323
Anthropology
- Archaeology 0324
- Cultural 0326
- Physical 0327

Business Administration
- General 0310
- Accounting 0272
- Banking 0770
- Management 0454
- Marketing 0338

Canadian Studies 0385
Economics
- General 0501
- Agricultural 0503
- Commerce-Business 0505
- Finance 0508
- History 0509
- Labor 0510
- Theory 0511

Folklore 0358
Geography 0366
Gerontology 0351
History
- General 0578
- Ancient 0579
- Medieval 0581
- Modern 0582
- Black 0328
- African 0331
- Asia, Australia and Oceania 0332
- Canadian 0334
- European 0335
- Latin American 0336
- Middle Eastern 0333
- United States 0337

History of Science 0585
Law 0398
Political Science
- General 0615
- International Law and Relations 0616
- Public Administration 0617

Recreation 0814
Social Work 0452
Sociology
- General 0626
- Criminology and Penology 0627
- Demography 0938
- Ethnic and Racial Studies 0631
- Individual and Family Studies 0628
- Industrial and Labor Relations 0629
- Public and Social Welfare 0630
- Social Structure and Development 0700
- Theory and Methods 0344

Transportation 0709
Urban and Regional Planning 0999
Women's Studies 0453

THE SCIENCES AND ENGINEERING

BIOLOGICAL SCIENCES
Agriculture
- General 0473
- Agronomy 0285
- Animal Culture and Nutrition 0475
- Animal Pathology 0476
- Food Science and Technology 0359
- Forestry and Wildlife 0478
- Plant Culture 0479
- Plant Pathology 0480
- Plant Physiology 0817
- Range Management 0777
- Wood Technology 0746

Biology
- General 0306
- Anatomy 0287
- Biostatistics 0308
- Botany 0309
- Cell 0379
- Ecology 0329
- Entomology 0353
- Genetics 0369
- Limnology 0793
- Microbiology 0410
- Molecular 0307
- Neuroscience 0317
- Oceanography 0416
- Physiology 0433
- Radiation 0821
- Veterinary Science 0778
- Zoology 0472

Biophysics
- General 0786
- Medical 0760

EARTH SCIENCES
Biogeochemistry 0425
Geochemistry 0996
Geodesy 0370
Geology 0372
Geophysics 0373
Hydrology 0388
Mineralogy 0411
Paleobotany 0345
Paleoecology 0426
Paleontology 0418
Paleozoology 0985
Palynology 0427
Physical Geography 0368
Physical Oceanography 0415

HEALTH AND ENVIRONMENTAL SCIENCES
Environmental Sciences 0768
Health Sciences
- General 0566
- Audiology 0300
- Chemotherapy 0992
- Dentistry 0567
- Education 0350
- Hospital Management 0769
- Human Development 0758
- Immunology 0982
- Medicine and Surgery 0564
- Mental Health 0347
- Nursing 0569
- Nutrition 0570
- Obstetrics and Gynecology 0380
- Occupational Health and Therapy 0354
- Ophthalmology 0381
- Pathology 0571
- Pharmacology 0419
- Pharmacy 0572
- Physical Therapy 0382
- Public Health 0573
- Radiology 0574
- Recreation 0575
- Speech Pathology 0460
- Toxicology 0383

Home Economics 0386

PHYSICAL SCIENCES
Pure Sciences
Chemistry
- General 0485
- Agricultural 0749
- Analytical 0486
- Biochemistry 0487
- Inorganic 0488
- Nuclear 0738
- Organic 0490
- Pharmaceutical 0491
- Physical 0494
- Polymer 0495
- Radiation 0754

Mathematics 0405
Physics
- General 0605
- Acoustics 0986
- Astronomy and Astrophysics 0606
- Atmospheric Science 0608
- Atomic 0748
- Electronics and Electricity 0607
- Elementary Particles and High Energy 0798
- Fluid and Plasma 0759
- Molecular 0609
- Nuclear 0610
- Optics 0752
- Radiation 0756
- Solid State 0611

Statistics 0463

Applied Sciences
Applied Mechanics 0346
Computer Science 0984
Engineering
- General 0537
- Aerospace 0538
- Agricultural 0539
- Automotive 0540
- Biomedical 0541
- Chemical 0542
- Civil 0543
- Electronics and Electrical 0544
- Heat and Thermodynamics 0348
- Hydraulic 0545
- Industrial 0546
- Marine 0547
- Materials Science 0794
- Mechanical 0548
- Metallurgy 0743
- Mining 0551
- Nuclear 0552
- Packaging 0549
- Petroleum 0765
- Sanitary and Municipal 0554
- System Science 0790

Geotechnology 0428
Operations Research 0796
Plastics Technology 0795
Textile Technology 0994

PSYCHOLOGY
General 0621
Behavioral 0384
Clinical 0622
Developmental 0620
Experimental 0623
Industrial 0624
Personality 0625
Physiological 0989
Psychobiology 0349
Psychometrics 0632
Social 0451

TIME-DOMAIN BASED FINITE DIFFERENCE TECHNIQUE AND ITS APPLICATIONS TO ELECTROMAGNETIC PROBLEMS

BY

MOUSA ISSA M. HUSSEIN

A Thesis submitted to the Faculty of Graduate Studies of the University of Manitoba in partial fulfillment of the requirements of the degree of

DOCTOR OF PHILOSOPHY

© 1995

Permission has been granted to the LIBRARY OF THE UNIVERSITY OF MANITOBA to lend or sell copies of this thesis, to the NATIONAL LIBRARY OF CANADA to microfilm this thesis and to lend or sell copies of the film, and LIBRARY MICROFILMS to publish an abstract of this thesis.

The author reserves other publication rights, and neither the thesis nor extensive extracts from it may be printed or other-wise reproduced without the author's written permission.

I hereby declare that I am the sole author of this thesis.

I authorize the University of Manitoba to lend this thesis to other institutions or individuals for the purpose of scholarly research.

I further authorize the University of Manitoba to reproduce this thesis by photocopying or by other means, in total or in part, at the request of other institutions or individuals for the purpose of scholarly research.

The University of Manitoba requires the signatures of all persons using or photocopying this thesis. Please sign below, and give address and date.

Abstract

A general literature review was conducted to obtain a suitable, accurate, efficient and inexpensive tool to model some engineering applications of electromagnetic waves. The finite-difference method solution of the time-dependent Maxwell's equations is selected for this task. The finite-difference time-domain (FDTD) technique is applicable to a wide range of problems. It offers many advantages as an electromagnetic modeling, simulation, and analysis tool.

A general FDTD computer code is developed based on the time-dependent Maxwell's equations to model and solve three-dimensional electromagnetic problems. In order to facilitate the use of the FDTD code and improve its capabilities, the contour integral method is employed to obtain a general set of difference equations. The code developed is used to study the specification of the space cell size and time stepping increment. A numerical experiment is conducted to give insight and understanding to the space increment selection. A natural requirement of the FDTD technique is the use of outer radiation boundary conditions which simulate an infinite space for the open boundary problems. A detailed study on the most commonly used radiation boundary conditions is presented.

The FDTD special capability of modeling thin wires is investigated. The implementation and application of lumped circuit elements are investigated by deriving general 3-D modeling equations for passive and active lumped circuit elements. In order for the 3-D code to be complete and general, a near-field to far-field transformation is presented. This part of the code is used to transform the near-field data, which is a natural product of the FDTD simulations, to the far-field to obtain antenna radiation patterns or the radar cross-section of 3-D structures.

The FDTD code is used to obtain the radar cross section for two scattering

geometries, a conducting cube and a dielectric sphere. The developed code is also applied successfully to model three antenna configurations. These are a monopole mounted on a conducting box, a bent-slot antenna flush mounted on a rectangular conducting box and a quarter-wavelength monopole antenna mounted on an automobile's roof. Scattering and radiation results obtained using the developed code agree very well with published and available data.

The implementation of the code for planar microstrip circuits is considered via its application to several microstrip lines, a line-fed microstrip patch antenna and an aperture-coupled microstrip patch antenna. Microstrip parameters such as the effective dielectric constant, characteristic impedance, scattering parameters and input impedance are obtained.

In the area of electromagnetic interference and compatibility (EMI/EMC), the code is used to study electromagnetic coupling to wires inside shielded enclosures. The shielding effect of metal cabinets and enclosures is also demonstrated. The EMC test environment is studied for an open-sight, a screened room, and a screened room lined with absorbing materials.

Acknowledgements

I wish to express my sincere gratitude and thanks to Allah the creator and the sustainer and to Dr. A. Sebak for his advice, continuous encouragement helpful discussion and assistance throughout the course of this research.

Special thanks to the external examiner Dr. A. Z. Elsherbeni and my advisory committee Profs. E. Bridges, I. Ciric and J. Cahon for their helpful discussion and valuable assistance.

Thanks to my wife, daughters Huda and Iman, my family across the Atlantic and my colleagues for their patience, continuous encouragement and support.

The author wishes to acknowledge the financial assistance of the Natural Science and Engineering Research Council of Canada, the Department of Electrical and computer Engineering and the Faculty of Graduate studies of the University of Manitoba, which make this research possible.

Finally I dedicate this work to Allah, my father, my mother and those researchers who choose to continue on this area of research.

TABLE OF CONTENTS

Abstract iv

Acknowledgements vi

CHAPTER **PAGE**

List of Figures x

1. Introduction **1**

1.1 Literature Review 1

1.1.1 Integral Equation Model 3

1.1.2 Differential Equation Model 4

1.2 FDTD Review 6

2. Theory of FDTD **11**

2.1 Fundamental Concepts 11

2.1.1 Maxwell's Curl Equations 11

2.1.2 Yee Cell Formulation 13

2.1.3 Contour Integral Formulation 16

2.2 Computational Aspects of FDTD Technique 19

2.2.1 Cell Size and Numerical Stability 20

2.2.2 Grid Zoning and Plane Wave Source Condition 27

2.2.3 Incident Field 28

2.2.4 Radiation Boundary Condition 30

3. Radiation Boundary Condition **32**

CHAPTER PAGE

3.1 Introduction 32
3.2 Mur Radiation Boundary Condition 33
3.3 Generalized and Higher Order RBC 37
3.4 Super-absorbing Boundary Condition 39
3.5 Comparison and Numerical Tests 44

4. FDTD Special Capabilities 57
4.1 Introduction 57
4.2 Thin Wire Modeling 58
4.3 Lumped Elements Modeling 60
4.4 Numerical Application 65

5. Application to 3-D Scattering and Radiation 83
5.1 Introduction 83
5.2 Near Field to Far Field Transformation 84
5.3 Application to Scattering Problems 88
5.4 Application to Antenna Radiation 92
5.4.1 Monopole Mounted on a Box 93
5.4.2 Bent-Slot Dipole 99
5.4.3 Monopole Mounted on a Car 104
5.5 Antenna Radiated Power and Efficiency 108

6. Application to Planar Microstrip Circuits 113
6.1 Introduction 113
6.2 Source Consideration and the Radiation Conditions 114
6.3 Microstrip Lines 118
6.4 Microstrip Line-Fed Patch Antenna 122

CHAPTER PAGE

6.5 Aperture-Coupled Microstrip Antenna 124

7. Application to EM Interference and Compatibility 136

7.1 Introduction 136

7.2 Field to Wire Coupling 139

7.3 EMC Test Environment 148

7.3.1 Effect of Testing Equipment on EMC Environment 148

7.3.2 Screened and Anechoic Rooms 154

8. Conclusions and Recommendations 158

8.1 Conclusions 158

8.2 Recommendations 160

APPENDICES 170

A. Realtion of Electric and Magnetic Fields for RBC Application 171

B. Discrete Fourier Transformation 173

LIST OF FIGURES

FIGURE		PAGE
2.1	Yee cell geometry.	14
2.2	(a) Faraday's contour integral. (b) Ampere's contour integral.	18
2.3	Geometry of the square cylinder.	21
2.4	Magnitude and phase comparison of FDTD and MoM results for the cylinder surface current distribution, for $\Delta = \lambda/6\pi$.	23
2.5	Magnitude and phase comparison of FDTD and MoM results for the cylinder surface current distribution, for $\Delta = \lambda/13\pi$.	24
2.6	Magnitude and phase comparison of FDTD and MoM results for the cylinder surface current distribution, for $\Delta = \lambda/20\pi$.	25
2.7	Magnitude and phase comparison of FDTD and MoM results for the cylinder surface current distribution, for $\Delta = \lambda/32\pi$.	26
2.8	Grid zoning.	27
2.9	Plane wave source.	28
2.10	Corrected fortran code flow chart after [64].	31
3.1	2-D computational domain for RBC application.	35
3.2	Two-dimensional finite-difference grid.	41
3.3	2-D computational domain for numerical experimentation.	45
3.4	Compact pulse wave source.	47
3.5	Gaussian pulse wave source.	48
3.6	E_z field at points (i,1) and $t = 80\Delta t$ computed in the larger and smaller domain. The smaller domain is truncated with $E = 0$ RBC.	49
3.7	E_z field at points (i,1) and $t = 80\Delta t$ computed in the larger and smaller domain. The smaller domain is truncated with Mur first order RBC.	49
3.8	E_z field at points (i,1) and $t = 80\Delta t$ computed in the larger and smaller domain. The smaller domain is truncated with Mur second order RBC.	50
3.9	E_z field at points $(i, 1)$ and $t = 80\Delta t$ computed in the larger and smaller domain. The smaller domain is truncated with third order RBC, $p_0 = 1.0, p_2 = -0.75$ and $q_2 = -0.25$	50

FIGURE **PAGE**

3.10 E_z field at points (i,1) and $t = 80\Delta t$ computed in the larger and smaller domain. The smaller domain is truncated with $E = 0$ and super-absorption RBC. 51

3.11 E_z field at points (i,1) and $t = 80\Delta t$ computed in the larger and smaller domain. The smaller domain is truncated with Mur first order and super-absorption RBC. 51

3.12 Comparison of the reflection error of $E_z(i, 1)$ at $t = 80\Delta t$, computed using Mur first, second and third order RBC. 52

3.13 Comparison of the reflection error of $E_z(i, 1)$ at $t = 80\Delta t$, computed using $E = 0$ and super-absorption, Mur first and super-absorption, Mur second and third order RBC. 52

3.14 Comparison of the time response of $E_z(25, 1)$, computed using the larger domain and the smaller domain truncated using Mur first RBC. 53

3.15 Comparison of the time response of $E_z(25, 1)$, computed using the larger domain and the smaller domain truncated using Mur second RBC. 53

3.16 Comparison of the time response of $E_z(25, 1)$, computed using the larger domain and the smaller domain truncated using third order RBC. 54

3.17 Comparison of the time response of $E_z(25, 1)$, computed using the larger domain and the smaller domain truncated using $E = 0$ and super-absorption RBC. 54

3.18 Comparison of the time response of $E_z(25, 1)$, computed using the larger domain and the smaller domain truncated using Mur first and super-absorption RBC. 55

3.19 Comparison of the reflection error of $E_z(i, 1, 25)$ at $t = 80\Delta t$, computed using $E = 0$, Mur first and second RBC. 56

3.20 Comparison of the reflection error of $E_z(i, 1, 25)$ at $t = 80\Delta t$, computed using $E = 0$ and super-absorption, Mur first and super-absorption and Mur second RBC. 56

4.1 Field locations and geometry for thin wire. 58

4.2 Input current for the wire dipole with one cell approximation radius. 70

4.3 Input current for the wire dipole with contour integral approximation. 70

FIGURE **PAGE**

4.4 Magnitude and phase of the input current for the wire dipole with one cell approximation. 71
4.5 Magnitude and phase of the input current for the wire dipole with contour integral approximation. 72
4.6 Magnitude of the input impedance for the wire dipole with one cell approximation. 73
4.7 Magnitude of the input impedance for the wire dipole with contour integral approximation. 73
4.8 Current response at location (0,0,15), 15 cells form the lower end of the wire dipole with one cell approximation radius. 74
4.9 Current response at location (0,0,15), 15 cells form the lower end of the wire dipole with contour integral. 74
4.10 Magnitude and phase of the current at cell 15 of the wire dipole with one cell approximation. 75
4.11 Magnitude and phase of the current at cell 15 of the wire dipole with contour integral approximation. 76
4.12 Transient current through the 50Ω resistance at cell location $(i, j, 15)$. 77
4.13 Transient voltage across the 50Ω resistance at cell location $(i, j, 15)$. . 77
4.14 Comparison of the lumped resistance value calculated using FDTD, CFDTD and the ideal value $R = 50\Omega$. 78
4.15 Transient current through the capacitor at cell location $(i, j, 15)$. . . . 78
4.16 Transient voltage across the capacitor at cell location $(i, j, 15)$. 79
4.17 Comparison of the lumped capacitive reactance value calculated using FDTD, CFDTD and circuit theory. 79
4.18 Transient current through the parallel RLC circuit at location $(i, j, 15)$. 80
4.19 Transient voltage across the parallel RLC circuit at location $(i, j, 15)$. 80
4.20 Comparison of the real and imaginary lumped impedance calculated using CFDTD and circuit theory. 81
4.21 Comparison of the lumped impedance $|Z_{LRC}|$ calculated using CFDTD and circuit theory. 81
4.22 Phase variation of R, C, and parallel RLC with frequency. 82
5.1 Near field to far field transformation surface. 84
5.2 Normalized radar cross-section of the conducting cube with $k_o a = 1$ and $\phi = 0^o$. 90

FIGURE **PAGE**

5.3 Comparison of the radar cross-section of the lossless and lossy sphere, $k_o a = \pi$, $\varepsilon_r = 3.0$, $\sigma = 0.04$ and at $\phi = 0^o$. 90
5.4 Back scattering behavior of a conducting sphere, at $\phi = 0^o$, $\theta = 90^o$ and $a = 0.437\lambda$. 91
5.5 Monopole antenna on a rectangular box. 95
5.6 Radiation pattern of monopole antenna on a box, x-z plane, $\phi = 0^o$ and $L_z = 130mm$. 96
5.7 Radiation pattern of monopole antenna on a box, y-z plane, $\phi = 90^o$ and $L_z = 130mm$. 96
5.8 Radiation pattern of monopole antenna on a box, $\theta = 90^o$ and $L_z = 130mm$. 97
5.9 Radiation pattern of monopole antenna on a box, x-z plane, $\phi = 0^o$ and $L_z = 200mm$. 97
5.10 Radiation pattern of monopole antenna on a box, $\phi = 90^o$ and $L_z = 200mm$. 98
5.11 Radiation pattern of monopole antenna on a box, x-y plane, $\theta = 90^o$ and $L_z = 200mm$. 98
5.12 Bent-slot antenna on a rectangular box. (a) Type I. (b) Type II. . . . 101
5.13 Radiation pattern due to bent-slot antenna, x-y plane, $\theta = 90^o$. Type I. 102
5.14 Radiation pattern due to bent-slot antenna, x-z plane, $\phi = 0^o$. Type I. 102
5.15 Radiation pattern due to bent-slot antenna, x-y plane, $\theta = 90^o$. Type II. 103
5.16 Radiation pattern due to bent-slot antenna, x-z plane, $\phi = 0^o$. Type II. 103
5.17 Mobile monopole antenna and Automobile model. 106
5.18 Radiation pattern E_θ from the automobile antenna, in the x-z plane 107
5.19 Radiation pattern E_θ from the automobile antenna, in the y-z plane 107
5.20 Input power for the dipole antenna. 111
5.21 Power Dissipated in the 50 Ω resistance. 111
5.22 Dipole radiated power. 112
5.23 Antenna efficiency. 112
6.1 Microstrip geometry and computation domain. 115
6.2 Microstrip line geometry. 118
6.3 Geometry of, (a) open end microstrip line, (b) matched open-end microstrip line. 121

FIGURE **PAGE**

6.4 Line-fed rectangular microstrip antenna. 122
6.5 3-D geometry of aperture-coupled microstrip patch antenna. 125
6.6 Geometry of aperture-coupled microstrip patch antenna, x-y plane. . 125
6.7 Electric field, E_z, distribution just underneath the strip line at different positions a long the y-axis. 127
6.8 Effective dielectric constant of the strip line as a function of frequency, FDTD (solid) and microstrip theory (dashed). 127
6.9 Characteristic impedance of the strip line as a function of frequency. . 128
6.10 Transient electric field, E_z, distribution just beneath the open end strip line at a distance $L = 3.81mm$. 128
6.11 Magnitude and phase of the frequency dependent S_{11} parameter of the open end strip line. 129
6.12 Transient electric field, E_z, distribution just beneath the open end 50Ω match terminated strip line at a distance $L = 3.81mm$. 130
6.13 Distribution of $E_z(x, y, t)$ just underneath the dielectric interface of the line-fed microstrip patch antenna at $200, 300, 400$ and 600 time steps. 131
6.14 Transient electric field, E_z, distribution just beneath the strip line of the microstrip patch at a distance $L = 40\Delta y$ from the patch edge. . . 132
6.15 Return loss S_{11} of the microstrip patch antenna. 132
6.16 Input impedance of the microstrip patch antenna near the operating resonance at $7.475GHz$. 133
6.17 Distribution of $E_z(x, y, t)$ just underneath the dielectric interface of the microstrip patch of the aperture-coupled microstrip antenna at $200, 300, 400$ and 600 time steps. 134
6.18 Transient electric field, E_z, distribution just above the strip line of the aperture-coupled microstrip antenna at a distance $L = 80\Delta y$ from the open end of the strip line. 135
6.19 Return loss S_{11} of the aperture-coupled microstrip antenna. 135
7.1 Generic EMC problem geometry. 140
7.2 Current in the 50Ω resistance due to coupling with the field due to plane wave excitation. 143
7.3 Current in the 50Ω resistance due to coupling with the dipole field, with no box. 143

FIGURE **PAGE**

7.4 Current in the 50Ω resistance due to coupling with the dipole field, with box and slot. 144
7.5 Current in the 50Ω resistance due to coupling with the dipole field, with box and slot covered with absorbing material. 144
7.6 Time-domain E_z response near the center of the box position, with no box present. 145
7.7 Time-domain E_z response near the center inside the box. 145
7.8 Frequency response of the field near the center of the box position, with no box present 146
7.9 Frequency response of the field near the center inside the box. 146
7.10 Shielding effect of the conducting box with a slot. 147
7.11 Resonance inside a screened empty room. 150
7.12 Resonance inside a screened room with a $15cm$ long wire. 150
7.13 Resonance inside a screened room with a $1m$ long wire. 151
7.14 E_z profile on a plane midway and parallel to the ground plane for an empty room. 152
7.15 E_z profile on a plane midway and parallel to the ground plane for room with $15cm$ dipole. 152
7.16 E_z profile on a plane midway and parallel to the ground plane for room with $1m$long dipole. 153
7.17 E_z field midway above the ground plane for screened room. 156
7.18 E_z field midway above the ground plane with Mur's absorbing boundaries. 156
7.19 E_z field midway above the ground plane for screened room lined with RAM. 157

CHAPTER 1

Introduction

The science of electromagnetics plays a major role in predicting and understanding many of nature's phenomena and it has contributed greatly to other areas of science. Over the years the science of electromagnetics has been involved in wide range of applications such as scattering, radiation, transmission-line coupling, electromagnetic interference (EMI), lightning and electromagnetic pulse (EMP), shielding and electromagnetic compatibility (EMC), filters, magnetic circuits, biomedical applications and communications.

An extensive and substantial amount of work has been reported in the literature towards predicting, verifying and trying to understand electromagnetic radiation and scattering phenomena. The purpose of this research is to obtain a suitable, accurate, efficient and inexpensive numerical mathematical model which is capable of modeling a wide range of electromagnetic problems.

1.1 Literature Review

Engineering analysis and design efforts in the area of electromagnetics can be classified into three major categories; experimental, analytical, and computational. Experimental is a limited, inflexible and expensive approach. Each specific problem requires a unique setup, also not every problem in nature can fit under this category. Similarly analytic solution is only possible for small class of problems for which the

object boundaries coincide with the complete constant-coordinate surfaces of an orthogonal coordinate system. Other cases become tractable only if approximations or idealizations can be made. Some of the available analytic techniques are, separation of variables, reciprocity theorem, and equivalence principle.

On the other hand, computational electromagnetics is one of the newest and fastest growing research area. This is due to the advances in the technology of high-speed large-central-memory computer systems. Computational electromagnetics involves the electromagnetic modeling, simulation and analysis of electromagnetic responses of complex systems to various sources. It provides an understanding of the system response that allows for the better design or modification of the system. Generally speaking, numerical techniques are only tools developed to solve a mathematical model (equations). Most of nature's phenomena can be modeled using mathematical models in integral or differential form. Based on this, most available numerical techniques are classified as integral or differential models.

It is well known that Maxwell's equations provide the basis for studying electromagnetic effects. Maxwell's equations can be given in a differential or integral form. Accordingly, numerical techniques may take two different directions depending on how the equations are manipulated to obtain the starting equations. The integral and differential equation models can be classified further into another two classes depending on the domain of computation. For the case where the time dependent is sinusoidal, the computation will be carried over the spatial domain at specific frequency, this is called frequency-domain approach. In the case where the transient response is required the time dependent factor can not be suppressed. Therefore, the computational domain is space and time dependent. This is called time-domain approach.

Over the years researchers utilized all four combinations of classes in an effort to

obtain an efficient, accurate, and time saving approach. In order to grasp a better understanding of the available numerical techniques, this review will be based mainly on the two major models of Maxwell's equations.

1.1.1 Integral Equation Model

The starting point for developing an integral equation model in electromagnetics is the selection of an appropriate Green's function for the problem of interest. The integral equation model can be formulated in either the frequency-domain, where the harmonic time variation $\exp(j\omega t)$ is assumed, or in the time-domain, where time is treated as an independent variable. Whether frequency or time dependent formulation is used, the integral equation model reduces the problem into an integral equation in terms of specialized Green's functions with the surface fields as unknown quantities. This usually result in a system with a dense matrix equation.

Method of moments (MoM) is considered the leading method in the integral equation frequency-domain approach. It is a general procedure for solving linear equations. The use of method of moments has become popular in electromagnetics after the work of Richmond [1], [2] and Harrington [3], [4].

For frequencies above the resonance region, the geometrical theory of diffraction (GTD), an asymptotic theory developed by Keller [5], can be used. This is an extension of the geometrical optics theory. A hybrid technique for combining the method of moments with the geometrical theory of diffraction is extended by Davidson and Thiele [6] to account for the natural coupling between two monopole antennas on a large circular cylinder by means of curved surface wave diffraction. Combining method of moments with GTD will result in a great saving in time and memory. This is because the computation time of GTD is independent of increasing problem size in frequency, in contrast with the MoM.

The time-domain integral equation approach is used by many authors in the literature. Gomez *et al.* [7] studied the interaction of transient electromagnetic pulse (EMP) with perfect electric conductor structures. The electric field integral equation and the magnetic field integral equation were both used in the development of their code. Another method which uses the time-domain integral equation approach is the singularity expansion method (SEM) [8]. This method employs the use of method of moments where the zeros of the determinant of the system matrix define the locations of the natural resonances of the structure in terms of exponentially damped sinusoids.

Formulating the integral equation model in the time-domain offers substantial advantage over its formulation in the frequency-domain. It provides more information and a better understanding of the system response. Also numerical techniques in general, due to the discretization process, produce unwanted information (artifacts). These unwanted artifacts are usually separated in frequency from the desired time-domain data using Fourier transformation, whereas such separation does not occur in the frequency-domain.

1.1.2 Differential Equation Model

The differential equation model can be regarded as a model which applies Maxwell's equations locally. This means that the spatial variation of the fields must be developed from sampling in as many dimensions as possessed by the problem. Due to the locality of the differential model, it is capable of treating medium inhomogeneities, nonlinearities, and time variations in a straightforward manner.

Maxwell's equations in the frequency-domain have been employed using many approaches. One approach for solving Maxwell's equations is to divide space into two parts. One is a spherical region of finite extent, enclosing the object. In this region

solutions are obtained using the finite element method. The rest is the space outside the spherical region in which the electromagnetic waves are expanded in terms of spherical harmonics. The solutions from these two regions have to be matched across the common connecting boundary. Chang and Mei [9] pioneered a solution along these lines for a two-dimensional geometry and called it the unimoment method. Later this approach was extended to 3-D problems, and it is commonly known in literature as the finite element method. Castillo *et al.* [10] used this technique to analyze general multiconductor printed-circuit transmission line systems for both lossless and lossy cases. Merewether and Fisher [11] applied the equivalence technique to the problem of predicting the fields inside aperture-driven cavities. Their approach allows the prediction of the fields penetrating large apertures into complex cavities using the finite-difference analysis procedure. Beaubien and Wexler [12] used the finite-difference method for predicting higher order waveguide modes.

The last class in this review is the use of Maxwell's equations in time-domain. One technique is the use of point-matched finite-element formulation [13]. Another approach is the transmission line matrix (TLM) method [14]. TLM method is based on the equivalence between Maxwell's equations for the electric and magnetic fields in a medium, and the equation for the voltage and currents on a network of continuous transmission lines. One other approach which has been introduced recently to the electromagnetic community by Fettweis [15] is the wave digital filter (WDF) method. This method is based on simulating the actual continuous-domain system by means of a discrete-domain system in such a way that all features of the actual system are preserved. Finally the finite-difference time-domain (FDTD) method developed by Yee [16], has been used extensively in electromagnetic applications. A general review in terms of capabilities and applications of the FDTD is given in the following section. A more detailed study will follow in later chapters.

1.2 FDTD Review

Of the many approaches in computational electromagnetics, including method of moments (MoM), finite-difference time-domain (FDTD), finite element (FE), geometrical theory of diffraction, wave digital filter (WDF), and physical optics, the finite-difference time-domain technique is applicable to the widest range of problems.

In 1966 Yee [16] applied the central finite difference to Maxwell's equations to develop a technique which is commonly known in the literature as the finite-difference time-domain (FDTD) method. It was nearly one decade before it was used to any great extent for actual applications. This is due to the lack of the necessary computer hardware capabilities.

The FDTD technique offers many advantages as an electromagnetic modeling, simulation, and analysis tool. Its capabilities include,

- Arbitrary three-dimensional (3-D) modeling.
- Simulation of electromagnetic field interaction with objects of arbitrary conductivity and frequency-dependent material.
- Predicting the response of a system such as, scattered field, radiation pattern, radar cross-section (RCS), currents, penetration and interior coupling, and scattering parameters for a given excitation.

The basis of the FDTD code is the two Maxwell's equations in time-domain. These equations are expressed in a linearized form by means of central finite differencing. Only nearest-neighbor interactions need to be considered as the fields are advanced temporally in discrete time steps over spatial cells of rectangular shape.

A decade after Yee developed the FDTD method, many authors and researchers modified, refined and used the method in different areas involving electromagnetic

wave scattering [17]-[20], aperture coupling [21]-[23], electromagnetic interaction with biological tissues [24]-[26], electromagnetic pulse coupling [27]-[31] and microwave circuit design [32] and [33]. A primary contribution to Yee's approach was the introduction of the integral equation approach (contour integral) by Taflove *et al.* [21]. This approach allows the modeling of smoothly curved conducting edges and surfaces [34].

In the area of antenna radiation, Reineix and Jecko [35] used the FDTD method to analyze microstrip patch antennas. Sheen *et al.* [36] applied the FDTD method to analyze planer microstrip circuits involving microstrip patch antennas and microstrip filters. Maloney *et al.* [37] investigated the application of FDTD method to the analysis of axially symmetric two-dimensional antennas. Recently, Kats *et al.* [38] extended the method to analyze electromagnetic radiation from a system containing horn antennas. Also Tirkas and Balanis [39] applied the FDTD to model antenna radiation by wire and aperture antennas mounted on finite size ground planes and pyramidal horns. In a recent work by Hussein and Sebak [40] they applied the FDTD to study the radiation from mobile antennas.

Research efforts in the area of the FDTD method are currently directed toward advancing its capabilities to model curved three-dimensional electromagnetic scattering or radiation problems. Holland developed a finite-difference solution of Maxwell's equations in a generalized nonorthogonal three-dimensional coordinate system using tensor notation [41]. Based on the Holland approach, Fusco has applied the curvilinear FDTD approach to model two-dimensional scattering problems [42].

Similar research efforts also continue using the computational fluid dynamics (CFD) approach and the finite-volume time-domain (FVTD) method. Shankar *et al.* used the CFD approach to obtain solutions to Maxwell's equations for two-

and three-dimensional problems involving curved surfaces [43], [44]. Using the CFD approach Maxwell's equations are first cast into conservation form and then solved using a finite-volume discretization procedure. A modified FVTD approach for solving Maxwell's equations was applied by Madsen and Ziolkowski [45], [46]. Their approach, which is based on the integral form of Maxwell's equations, allows the use of general nonorthogonal grids and is a direct generalization of the canonical staggered-grid finite-difference method. A similar approach using the FVTD method was reported by Holland *et al.* [47]. Taflove and Umashankar used the contour path integral to extend the FDTD method to model curved conducting surfaces by distorting the grid locally to the structure geometry [18]. Advances to the contour path FDTD method were reported in a recent work by Jurgens *et al.* [34] and [48].

The FDTD method is also capable of modeling hybrid electromagnetic systems that contain passive and active lumped elements. Sui *et al.* [49] extended the two-dimensional FDTD method to include lumped elements inside the grid. Discrete voltage and current sources with internal impedance are modeled by specifying the appropriate current/voltage characteristics of the source elements. They also treated both linear and nonlinear circuit elements. Chamberlin *et al.* [50] used frequency-domain and FDTD to study the behavior of a nonlinearly-terminated dipole. Recently an extension of the two dimensional work to three dimensions has been reported in [51] and [52].

The first part of Chapter 2 of this work discusses in detail the derivation and formulation of the discretized central differenced Maxwell's equations. The equations are formulated for lossy dielectrics, which in the limit of infinite conductivity become perfect conductors. The contour path integral is also discussed and its equivalence to the Yee algorithm is presented. The second part, FDTD basics, provides details and guide lines for applying the FDTD formulation. A detailed study of cell size

requirement and numerical stability is presented. Lattice zoning and incident field specification for plane wave excitation and other sources are discussed. A brief discussion on the use of outer radiation boundary conditions is presented. Finally the chapter concludes with a schematic diagram for code requirements and development.

Detailed and inclusive studies regarding the choice and applications of the radiation boundary conditions is reported in Chapter 3. Discussions on the derivation and application of Mur radiation boundary conditions, generalized and higher order radiation conditions and super-absorbing boundary conditions are presented.

Chapter 4 shades light on two of the FDTD special capabilities and their applications, namely, thin wire modeling and lumped circuit elements modeling. Derivation of proper equations and their implementation in the FDTD code of passive and active lumped element are provided.

The transformation of the near-field data, which is a natural product of the FDTD simulation, to the far-field and its application to 3-D scattering and radiation problems is discussed in Chapter 5. Scattering by a conducting cube and a dielectric sphere is presented to exploit the capabilities of the 3-D FDTD code. In the area of antenna applications, three antenna configurations are modeled, they are a monopole mounted on a conducting box, a bent-slot antenna flush mounted on a rectangular conducting box and a quarter-wavelength monopole antenna mounted on an automobile roof. The last part of Chapter 5 concludes with applications of the method to the radiation, power dissipation and efficiency computations of a dipole antenna.

Chapter 6 covers in details the use of FDTD in the application of planar microstrip circuits. Some special considerations regarding excitation modeling and radiation condition requirements are provided. Three microstrip circuits are discussed. These are a microstrip line, a microstrip line-fed patch antenna and an

aperture-coupled microstrip antenna.

The use of the FDTD in the area of electromagnetic interference and compatibility (EMI/EMC) is considered in Chapter 7. The chapter starts with a detailed introduction and definitions related to electromagnetic interference and system compatibility. The chapter then discusses the coupling of electromagnetic sources with wires in shielded enclosure and also discusses the shielding effect of a screened and shielded cabinet. Simulation of an EMC test environment is also considered. Finally Chapter 8 ends with conclusions about the presented work and offers some recommendations for potential future work.

CHAPTER 2

Theory of FDTD

2.1 Fundamental Concepts

2.1.1 Maxwell's Curl Equations

It is well known that Maxwell's curl equations provide the basis for studying electromagnetic phenomena. In general, Maxwell's equations can be given in differential or integral form, depending on how the equations are manipulated to obtain the starting equation. Solution to the time-dependent Maxwell's equations are unknown except for few special cases. This is due to the implementation of the boundary conditions.

The differential time-domain Maxwell's equations in a linear isotropic and frequency independent medium are given as:

$$\nabla \times \mathbf{E} = -\frac{\partial \mathbf{B}}{\partial \mathrm{t}} \tag{2.1}$$

$$\nabla \times \mathbf{H} = \frac{\partial \mathbf{D}}{\partial \mathrm{t}} + \mathbf{J} \tag{2.2}$$

where

$$\mathbf{B} = \mu \mathbf{H} \tag{2.3}$$

$$\mathbf{D} = \varepsilon \mathbf{E} \tag{2.4}$$

This is all the information needed to completely specify the field behavior in linear isotropic materials as long as the initial field distribution is specified and satisfies Maxwell's equations. The initial time is often taken as time zero. The field quantities and sources are set to zero at that time.

Hence, the starting point for the FDTD formulations is the curl equations (2.1)-(2.4). They can be rewritten into the form used for FDTD:

$$\frac{\partial \mathbf{H}}{\partial t} = -\frac{1}{\mu}\nabla \times \mathbf{E} \tag{2.5}$$

$$\frac{\partial \mathbf{E}}{\partial t} = \frac{1}{\varepsilon}\nabla \times \mathbf{H} - \frac{\sigma}{\varepsilon}\mathbf{E} \tag{2.6}$$

Her $\mathbf{J} = \sigma\mathbf{E}$ is used to allow for lossy dielectric material. $\mathbf{E}$ is the electric field, $\mathbf{H}$ is the magnetic field, ε is the electric permittivity, σ is the electric conductivity and μ is the magnetic permeability.

In a rectangular coordinate system, (2.5) and (2.6) are equivalent to the following system of scalar equations:

$$\frac{\partial H_x}{\partial t} = \frac{1}{\mu}\left[\frac{\partial E_y}{\partial z} - \frac{\partial E_z}{\partial y}\right] \tag{2.7}$$

$$\frac{\partial H_y}{\partial t} = \frac{1}{\mu}\left[\frac{\partial E_z}{\partial x} - \frac{\partial E_x}{\partial z}\right] \tag{2.8}$$

$$\frac{\partial H_z}{\partial t} = \frac{1}{\mu}\left[\frac{\partial E_x}{\partial y} - \frac{\partial E_y}{\partial x}\right] \tag{2.9}$$

$$\frac{\partial E_x}{\partial t} = \frac{1}{\varepsilon}\left[\frac{\partial H_z}{\partial y} - \frac{\partial H_y}{\partial z} - \sigma E_x\right] \tag{2.10}$$

$$\frac{\partial E_y}{\partial t} = \frac{1}{\varepsilon}\left[\frac{\partial H_x}{\partial z} - \frac{\partial H_z}{\partial x} - \sigma E_y\right] \tag{2.11}$$

$$\frac{\partial E_z}{\partial t} = \frac{1}{\varepsilon}\left[\frac{\partial H_y}{\partial x} - \frac{\partial H_x}{\partial y} - \sigma E_z\right] \tag{2.12}$$

2.1.2 Yee Cell Formulation

The system of six coupled partial differential equations of (2.7)-(2.12) forms the basis of the FDTD algorithm for electromagnetic radiation, interference, and interaction with three dimensional objects.

The system in (2.7)-(2.12) is differenced following Yee [16] notation. Here a space point in a rectangular grid is denoted as

$$(i, j, k) = (i\Delta x, j\Delta y, k\Delta z) \tag{2.13}$$

and any function of space and time in the rectangular grid at point (i, j, k) is given as

$$F^n(i, j, k) = F(i\Delta x, j\Delta y, k\Delta zy, n\Delta t) \tag{2.14}$$

where Δx, Δy, and Δz are, respectively, the grid space increments in the x, y, and z coordinate directions, Δt is the time increment and i, j, k, and n are integers.

The Yee FDTD algorithm is applied on a staggered grid, Fig. 2.1. The Cartesian components of the electric field are the unknowns on one grid and the Cartesian components of the magnetic field are the unknowns on the second grid offset from the first by a half-cell distance in each Cartesian direction. This is known as centered finite-difference with a second order accuracy. The space derivatives can be expressed as,

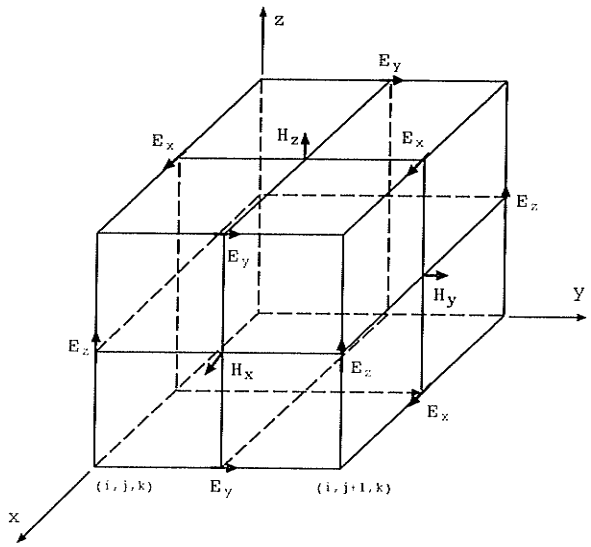

Figure 2.1: Yee cell geometry.

$$\frac{\partial F^n(i,j,k)}{\partial x} = \frac{F^n(i+1/2,j,k) - F^n(i-1/2,j,k)}{\Delta x} + \mathrm{O}(\Delta x^2) \tag{2.15}$$

Similarly the time derivative can be expressed in the same manner such as,

$$\frac{\partial F^n(i,j,k)}{\partial t} = \frac{F^{n+1/2}(i,j,k) - F^{n-1/2}(i,j,k)}{\Delta t} + \mathrm{O}(\Delta t^2) \tag{2.16}$$

To achieve the accuracy of (2.16), the electric field and the magnetic field values on the two grids are evaluated at alternate half time steps (leap-frog manner). Implementing these expressions to (2.7)-(2.12) results in a system of six difference equations, the following are the six finite-difference time-domain expression for the magnetic and electric field components, respectively.

$$H_x^{n+1/2}(i,j+1/2,k+1/2\ \ ) = H_x^{n-1/2}(i,j+1/2,k+1/2) + \frac{\Delta t}{\mu(i,j+1/2,k+1/2)} \Big\{ [E_y^n(i,j+1/2,k+1) - E_y^n(i,j+1/2,k)]/\Delta z + [E_z^n(i,j,k+1/2) - E_z^n(i,j+1,k+1/2)]/\Delta y \Big\} \quad (2.17)$$

$$H_y^{n+1/2}(i+1/2,j,k+1/2\ \ ) = H_y^{n-1/2}(i+1/2,j,k+1/2) + \frac{\Delta t}{\mu(i+1/2,j,k+1/2)} \{ [E_z^n(i+1,j,k+1/2) - E_z^n(i,j,k+1/2)]/\Delta x + [E_x^n(i+1/2,j,k) - E_x^n(i+1/2,j,k+1)]/\Delta z \} \quad (2.18)$$

$$H_z^{n+1/2}(i+1/2,j+1/2,k\ \ ) = H_z^{n-1/2}(i+1/2,j+1/2,k) + \frac{\Delta t}{\mu(i+1/2,j+1/2,k)} \{ [E_x^n(i+1/2,j+1,k) - E_x^n(i+1/2,j,k)]/\Delta y + [E_y^n(i,j+1/2,k) - E_y^n(i+1,j+1/2,k)]/\Delta x \Big\} \quad (2.19)$$

$$E_x^{n+1}(i+1/2,j,k\ \ ) = \frac{1 - \frac{\sigma(i+1/2,j,k)\Delta t}{2\varepsilon(i+1/2,j,k)}}{1 + \frac{\sigma(i+1/2,j,k)\Delta t}{2\varepsilon(i+1/2,j,k)}} E_x^n(i+1/2,j,k) + \frac{\Delta t}{\varepsilon(i+1/2,j,k)} \frac{1}{1 + \frac{\sigma(i+1/2,j,k)\Delta t}{2\varepsilon(i+1/2,j,k)}} \Big\{ [H_z^{n+1/2}(i+1/2,j+1/2,k) - H_z^{n+1/2}(i+1/2,j-1/2,k)]/\Delta y + [H_y^{n+1/2}(i+1/2,j,k-1/2) - H_y^{n+1/2}(i+1/2,j,k+1/2)]/\Delta z \Big\} \quad (2.20)$$

$$E_y^{n+1}(i,j+1/2,k\ \ ) = \frac{1-\frac{\sigma(i,j+1/2,k)\Delta t}{2\varepsilon(i,j+1/2,k)}}{1+\frac{\sigma(i,j+1/2,k)\Delta t}{2\varepsilon(i,j+1/2,k)}} E_y^n(i,j+1/2,k)$$
$$+\frac{\Delta t}{\varepsilon(i,j+1/2,k)} \frac{1}{1+\frac{\sigma(i,j+1/2,k)\Delta t}{2\varepsilon(i,j+1/2,k)}}$$
$$\Big\{[H_x^{n+1/2}(i,j+1/2,k+1/2) - H_x^{n+1/2}(i,j+1/2,k-1/2)]/\Delta z$$
$$+[H_z^{n+1/2}(i-1/2,j+1/2,k) - H_z^{n+1/2}(i+1/2,j+1/2,k)]/\Delta x\Big\} \quad (2.21)$$

$$E_z^{n+1}(i,j,k+1/2\ \ ) = \frac{1-\frac{\sigma(i,j,k+1/2)\Delta t}{2\varepsilon(i,j,k+1/2)}}{1+\frac{\sigma(i,j,k+1/2)\Delta t}{2\varepsilon(i,j,k+1/2)}} E_z^n(i,j,k+1/2)$$
$$+\frac{\Delta t}{\varepsilon(i,j,k+1/2)} \frac{1}{1+\frac{\sigma(i,j,k+1/2)\Delta t}{2\varepsilon(i,j,k+1/2)}}$$
$$\Big\{[H_y^{n+1/2}(i+1/2,j,k+1/2) - H_y^{n+1/2}(i-1/2,j,k+1/2)]/\Delta x$$
$$+[H_x^{n+1/2}(i,j-1/2,k+1/2) - H_x^{n+1/2}(i,j+1/2,k+1/2)]/\Delta y\Big\} \quad (2.22)$$

2.1.3 Contour Integral Formulation

The Yee algorithm for FDTD was originally interpreted as a direct approximation of the pointwise derivatives of Maxwell's time-dependent curl equations using numerical central differences. Although this interpretation is useful for understanding how FDTD models wave propagation away from material surfaces, however, it has a distinct drawback in modeling fine geometrical features properly, such as wires, slots and curved surfaces.

Contour integral formulation is a generalization of the traditional FDTD method, and it is capable of modeling such fine geometries. This approach involves a more macroscopic combined field description based upon Faraday's law and Ampere's law in integral forms and implemented on an array of electrically small specially orthogonal contours. The contours of Ampere's and Faraday's law

intersect each other's enclosed surfaces in the same manner as the links in a chain intersect, Fig. 2.2. For a lossless dielectric region Faraday's and Ampere's are given, respectively, by

$$\frac{\partial}{\partial t}\int_s \mathbf{B}\cdot\mathbf{ds} = -\oint_c \mathbf{E}\cdot\mathbf{dl} \tag{2.23}$$

$$\frac{\partial}{\partial t}\int_s \mathbf{D}\cdot\mathbf{ds} = \oint_c \mathbf{H}\cdot\mathbf{dl} \tag{2.24}$$

To illustrate the approach, consider the H_z component of the magnetic field and the encircling electric field components shown in Fig. 2.2 (a). The usual Yee notation is used, and the field locations are separated by $\Delta x, \Delta y$ and Δz as usual. Now applying (2.23) to the contour in Fig. 2.2 (a) , assuming that the fields are uniform along each side of the contour and $H_z(i,j,k)$ equals the average value of H_z over the surface s, the result is the usual FDTD update equation,

$$-\mu\frac{\partial H_z(i,j,k)}{\partial t} = \frac{E_x(i,j,k) - Ex(i,j+1,k)}{\Delta y} + \frac{E_y(i+1,j,k) - Ey(i,j,k)}{\Delta x} \tag{2.25}$$

Next, applying Ampere's integral equation (2.24) to the contour in Fig. 2.2 (b), results in the Yee time-stepping expression for E_z for the free-space case that was obtained directly from implementing the curl H equation with finite difference.

$$\varepsilon\frac{\partial E_z(i,j,k)}{\partial t} = \frac{H_x(i,j-1,k) - Hx(i,j,k)}{\Delta y} + \frac{H_y(i,j,k) - H_y(i-1,j,k)}{\Delta x} \tag{2.26}$$

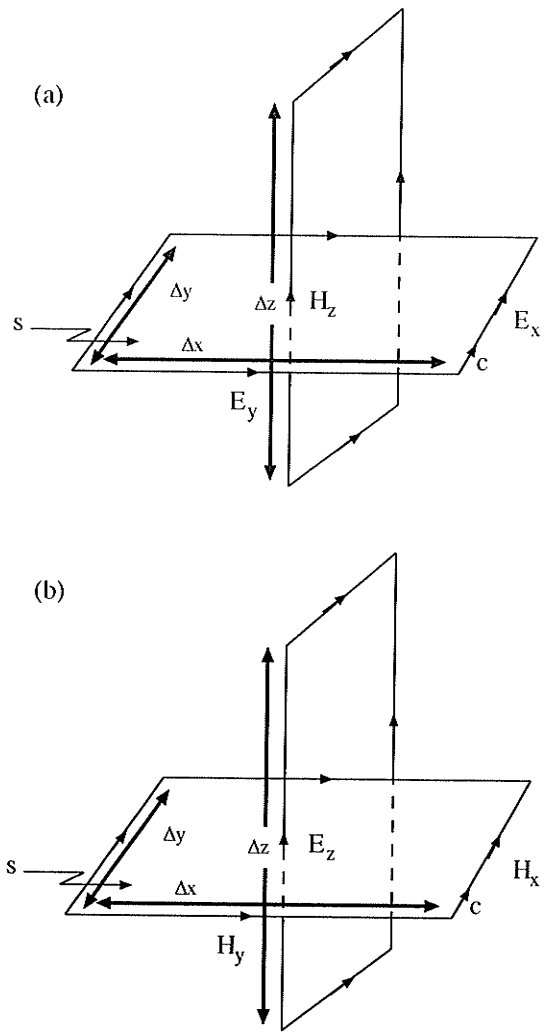

Figure 2.2: (a) Faraday's contour integral. (b) Ampere's contour integral.

2.2 Computational Aspects of FDTD Technique

The first consideration that needs to be determined before starting any numerical calculation is the cell size. For accurate results, the cell size must be small enough at the highest frequency of interest and, due to computational resources limitation, it has to be large enough to keep resources requirement manageable [53]. A cell size is directly related to the wavelength of the the problem under consideration. The wavelength depends on the material in which the wave is travelling. Thus, the greater the permittivity, the shorter the wavelength at a given frequency and the smaller the cell size required. The second important consideration is the maximum time step, it can be obtained directly using Courant condition [53].

Since the numerical algorithm for Maxwell's curl equations defined by the finite-difference system has a linear dependence upon the components of the electromagnetic field vectors, therefore, this system is valid for either the incident field vector components, the scattered field vector components or the total field vector components. Thus, the FDTD code developed is based on dividing the space into two distinct regions (total field region and scattered field region), separated by rectangular surfaces which serve to connect the fields in each region. This approach will enable the use of the incident field in analytic form at the connecting boundary. For problems which do not have an incident field as an excitation, such as for antenna radiation calculation, grid zoning is not required, instead a total field calculation will be used.

Whether total or scattered fields are computed in the outer region, Mur's [54] first or second order absorbing boundaries, a relatively reflection-free and easily implemented termination for the FDTD space, will be used.

2.2.1 Cell Size and Numerical Stability

The accuracy of the FDTD solution is highly dependent on cell size selection. The smaller the cell size the more accurate the solution. The critical question is "How much smaller?" [53]. A commonly used constraint is 10 cells/λ or less at the highest frequency of interest. In some cases, such as antenna input impedance or a very accurate near field information, $\lambda/20$ or even smaller cells may be required. However, in special cases reasonable results have been obtained with much smaller number of cells [55]. For regions of different dielectric materials, the maximum cell size is determined by the wavelength in the region of the highest permittivity.

The grid dispersion error is another key point in selecting a cell size [53]. Due to the fact that FDTD is an approximate technique, therefore, waves of different frequencies will travel at different speeds. For accurate and stable solutions, the grid dispersion error must be reduced to an acceptable level. This can be accomplished by reducing the cell size [56]

In order to understand the effect of cell size on the accuracy of the FDTD algorithm, a numerical experiment is conducted to study the effect of different cell sizes on the accuracy of the magnitude and the phase of the surface current on a conducting two-dimensional square cylinder Fig. 2.3. The cylinder electrical size is $k_o s = 2$, where s is the side of the cylinder and k_o is the wave number in free space. The excitation is assumed $z-$polarized TM_z plane wave incident on the conducting cylinder with an angle of $\phi^i = 0^o$.

Four different cell sizes are considered for this numerical experiment, they are $\Delta = \lambda/6\pi$, $\lambda/13\pi$, $\lambda/20\pi$ and $\lambda/32\pi$ and it is assumed that the cell is a square cell with $\Delta = \Delta x = \Delta y$. The magnitude and phase of the surface current distribution, extracted from the FDTD solution using the discrete Fourier transform (discussed

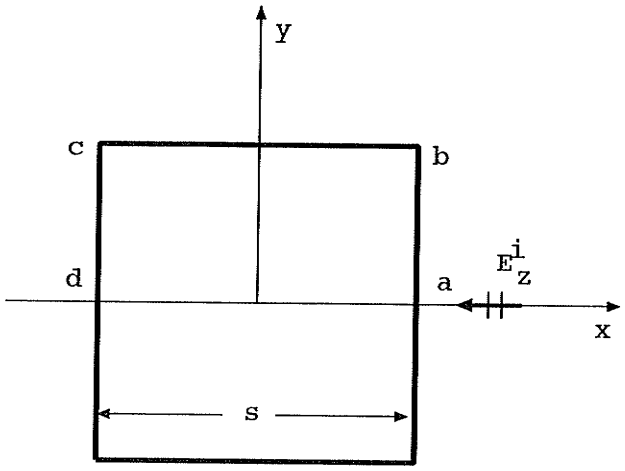

Figure 2.3: Geometry of the square cylinder.

in appendix B), is compared to that computed using the frequency-domain electric field integral equation (EFIE) method, which is solved using the method of moments (MoM).

It is observed from Fig. 2.4 that the accuracy for $\Delta = \lambda/6\pi$ is poor specially for the phase part. However, for cell size in the range of $\Delta = \lambda/13\pi$ to $\lambda/20\pi$ the accuracy has improved. From Figs. 2.5 and 2.6 it can be observed that the magnitude and phase of the FDTD computed surface current agree with the MoM solution results. Fig. 2.7 illustrates the effect of using a very small cell size. It is clear that the accuracy of the surface current has been affected, this is due to the fact that as the cell size gets smaller the absorbing boundaries get closer to the structure, this can be avoided by increasing the number of cells between the structure and the outermost boundaries, however, this increases the computational requirements.

Once the cell size is determined, the maximum size of the time step Δt follows immediately from the Courant condition [56]. To understand the basis for the Courant condition, consider a plane wave propagating through a FDTD grid. Within

one time step any point on this wave must not pass through more than one cell, because during one time step the wave can propagate only from one cell to its nearest neighbor. To insure the stability of the time-stepping algorithm, Δt is chosen to satisfy the inequality [57]

$$\Delta t \leq \frac{1}{c_{max}\left[\frac{1}{\Delta x^2}+\frac{1}{\Delta y^2}+\frac{1}{\Delta z^2}\right]^{1/2}} \tag{2.27}$$

where $c_{max} = \frac{1}{\sqrt{\mu\varepsilon}}$ is the maximum electromagnetic wave phase velocity within the media being modeled. A detailed discussion on the effect of Courant condition on the stability and the accuracy of the FDTD solution can be found in [53].

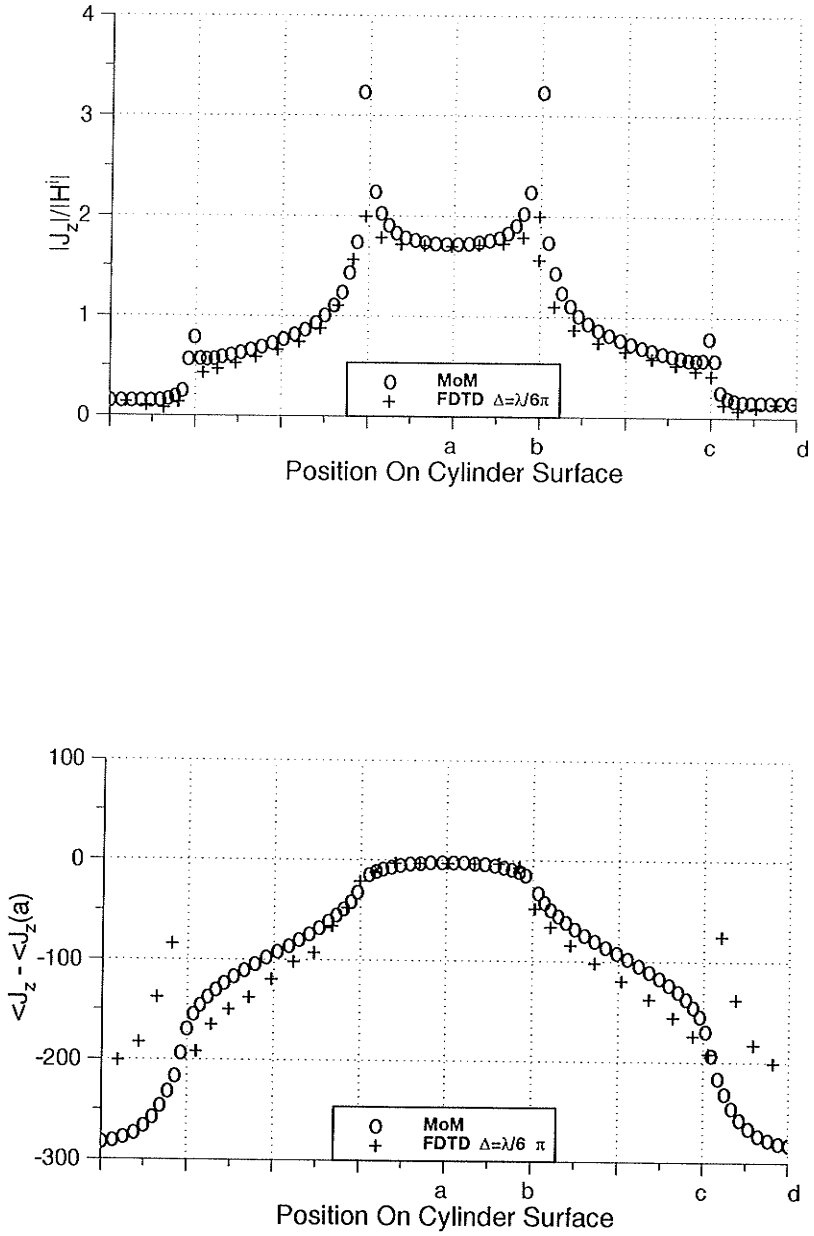

Figure 2.4: Magnitude and phase comparison of FDTD and MoM results for the cylinder surface current distribution, for $\Delta = \lambda/6\pi$.

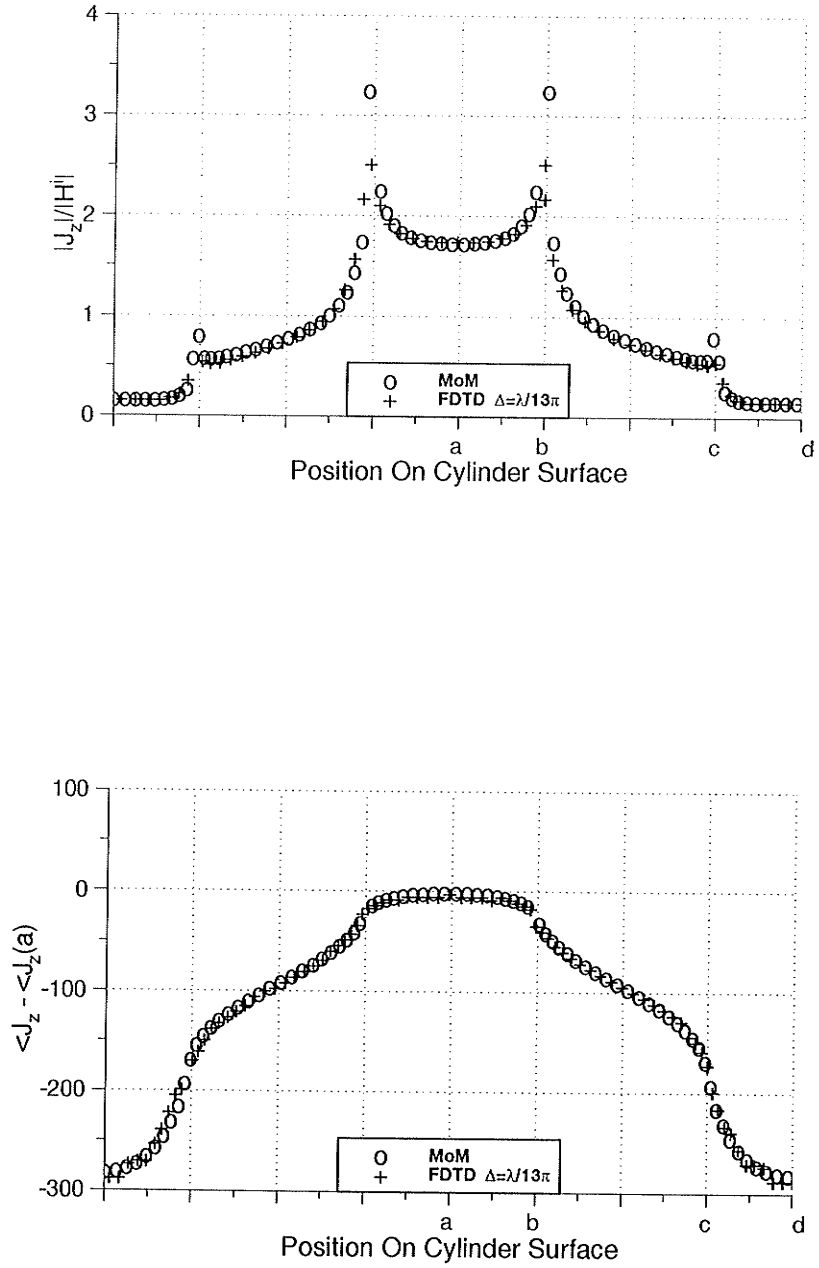

Figure 2.5: Magnitude and phase comparison of FDTD and MoM results for the cylinder surface current distribution, for $\Delta = \lambda/13\pi$.

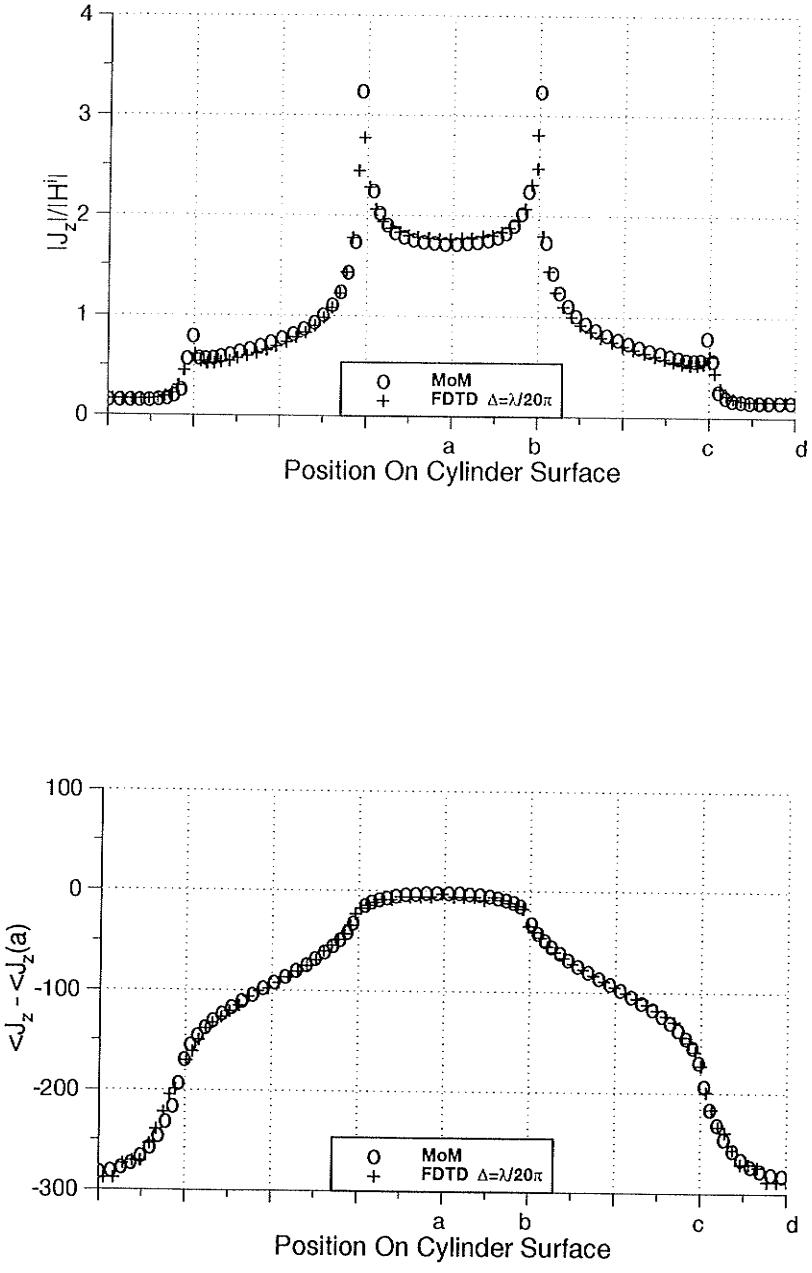

Figure 2.6: Magnitude and phase comparison of FDTD and MoM results for the cylinder surface current distribution, for $\Delta = \lambda/20\pi$.

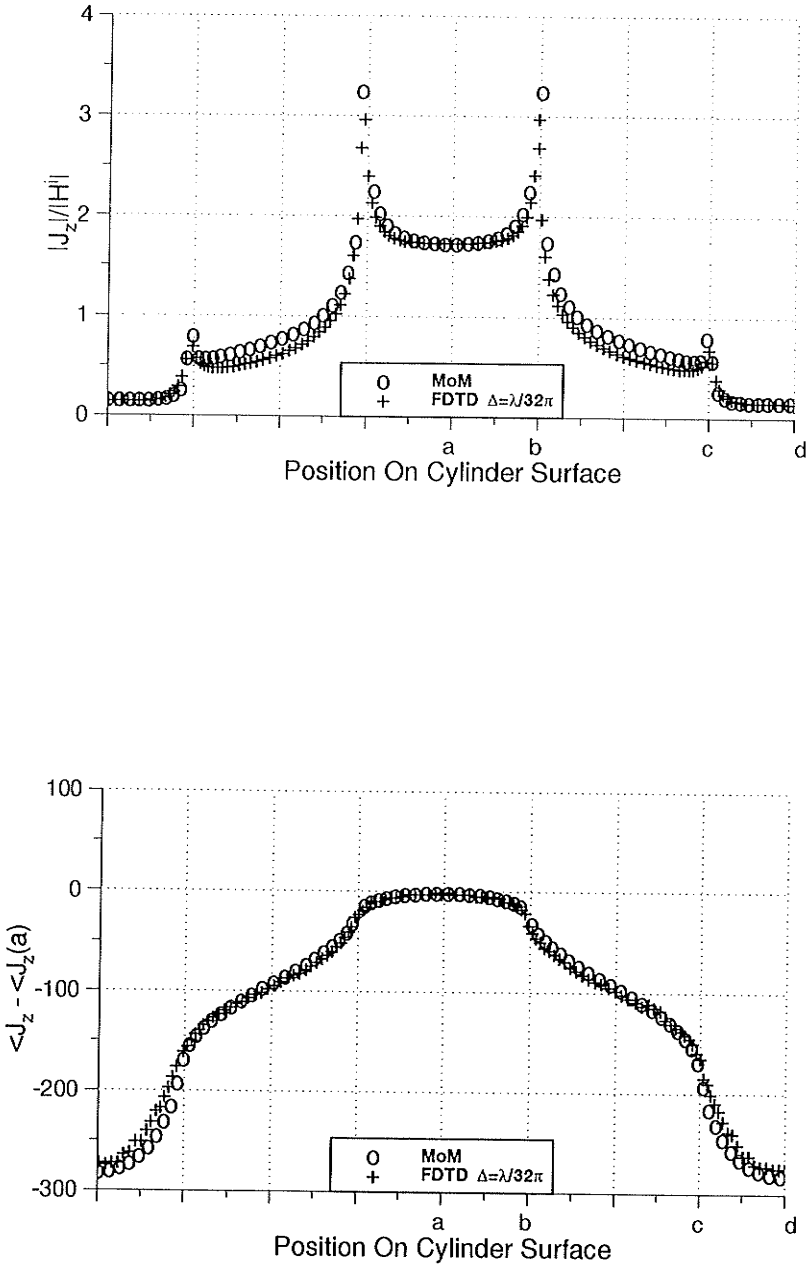

Figure 2.7: Magnitude and phase comparison of FDTD and MoM results for the cylinder surface current distribution, for $\Delta = \lambda/32\pi$.

2.2.2 Grid Zoning and Plane Wave Source Condition

Due to linear dependence of Maxwell's curl equations upon the components of the electromagnetic field vectors, the computational space of the FDTD will be divided into two distinct regions as shown in Fig. 2.8, separated by a rectangular virtual surface which serves to connect the fields in each region.

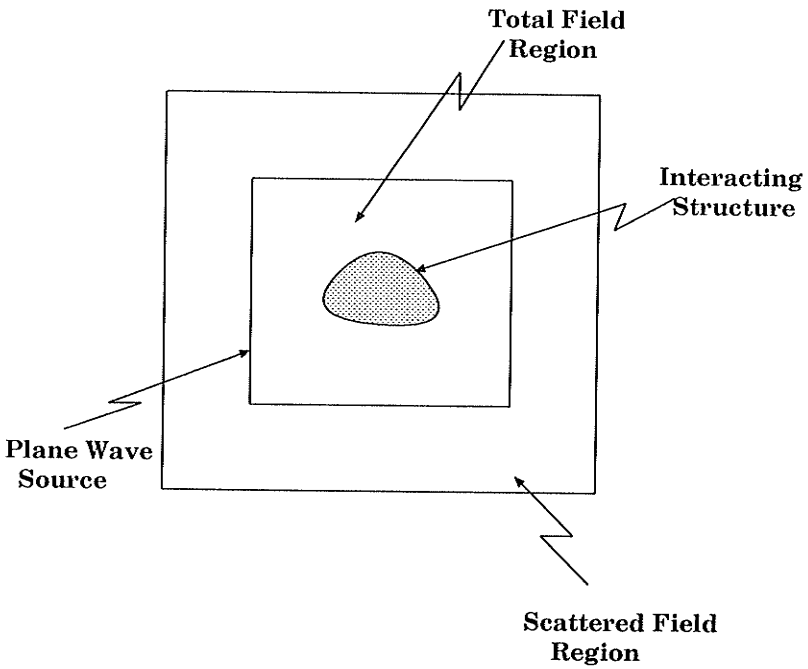

Figure 2.8: Grid zoning.

Region 1, the inner region of the FDTD space, is denoted as the total field region. This means that the finite difference system operates on total-field vector components. The interacting structure of interest is embedded within this region.

Region 2, the outer region of the FDTD space, is denoted as the scattered field region. Analogous to region 1, it is assumed that the finite difference system operates on scattered-field vector components only. The outer space planes bounding region 2 called space truncation planes or outer radiation boundary , which serves to implement the free-space radiation condition.

The incident wave, generated along one edge of the surface connecting the two regions, propagates through the total field region and is subtracted out of the other end. To demonstrate the use of this grid zoning, consider one edge of the connecting surface $j = j_o$ in a 2-D case, as shown in Fig. 2.9.

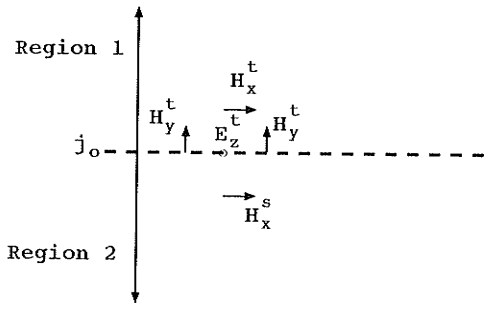

Figure 2.9: Plane wave source.

$E_z(i, j_o)$ at any time step is composed of the total electric field. It is updated using the ordinary FDTD, however, since H_x^s (in region 2) is used to update $E_z(i, j_o)$, H_x^{inc} must be added to it to account for the total field. On the other hand, updating $H_x^s(i, j_o - 1/2)$ require the subtraction of E_z^{inc} from $E_z(i, j_o)$ used to update $H_x^s(i, j_o - 1/2)$.

2.2.3 Incident Field

An important feature of using grid zoning is that the incident field can be expressed in a close simple form [53]. The incident field may be specified as a Gaussian pulse or a sinusoidal continuous plane wave (CW).

A time domain incident plane wave can be expressed in terms of its spherical coordinates components. The direction of the incident plane wave is specified using θ, measured from the z-axis, and ϕ, measured from the x-axis, with the origin at the center of the FDTD Cartesian system. Next, let a unit vector $\hat{r}$ point from the origin in the direction of θ and ϕ, an incident plane wave from this direction can be

specified as:

$$\mathbf{E} = \left[E_\theta \hat{\theta} + E_\phi \hat{\phi}\right] f(t + (\bar{r}' \cdot \hat{r})/c + R/c) \tag{2.28}$$

$$\mathbf{H} = \left[\frac{-E_\phi}{\eta}\hat{\theta} + \frac{E_\theta}{\eta}\hat{\phi}\right] f(t + (\bar{r}' \cdot \hat{r})/c + R/c) \tag{2.29}$$

here $\hat{\theta}$ and $\hat{\phi}$ are the spherical coordinate system unit vectors, η is the impedance of free space, c is the speed of light, and $\bar{r}'$ is the vector from the origin to point in the FDTD computation space at which the incident field is evaluated. $f(t)$ may be any function of time, *i.e.* sine wave or Gaussian pulse. R is an arbitrary reference distance, it is chosen so that the incident field does not appear suddenly at the scattering object, but rather propagates gradually into the FDTD space.

The amplitudes of the Cartesian components of the incident field are obtained as follow [53]:

$$\begin{aligned}
E_x &= E_\theta \cos\theta \cos\phi - E_\phi \sin\phi \\
E_y &= E_\theta \cos\theta \sin\phi + E_\phi \cos\phi \\
E_z &= -E_\theta \sin\theta \\
H_x &= \left(-E_\phi \cos\theta \cos\phi + E_\theta \sin\phi\right)/\eta \\
H_y &= \left(-E_\phi \cos\theta \sin\phi + E_\theta \cos\phi\right)/\eta \\
H_z &= \left(E_\phi \sin\theta\right)/\eta
\end{aligned}$$

In order to incorporate the relative time delay for any field component, *i.e.* E_x^n, at cell (i, j, k) and time step $n\Delta t$, $(\bar{r}' \cdot \hat{r})$ will take the following form,

$$\bar{r}' \cdot \hat{r} = ((i + 1/2)\Delta x \cos\phi \sin\theta + j\Delta y \sin\phi \sin\theta + k\Delta z \cos\theta) \tag{2.30}$$

The 1/2 cell offset in (2.30) is due to the location in the (i, j, k) Yee cell of the E_x component. Similar offset must be included for each field component.

2.2.4 Radiation Boundary Condition

In many scattering and radiation applications, the structure of interest is situated in an open space. In such cases the radiation condition at infinity should be satisfied, *i.e.*, the scattered or radiated field should propagate into boundless space. However, the FDTD computational space is bounded by necessity. Therefore, scattered or radiated fields arriving at the outermost boundary will be reflected back and will contaminate the interior field quantities. One approach to reduce or eliminate the reflected wave is the application of radiation boundary condition (RBC) at the outermost boundary. This boundary condition acts as an absorber which absorbs arriving waves and simulates an infinite space. Implementing such a boundary condition will reduce the number of cells needed to model the free space surrounding the scatterer or antenna. This will result in a corresponding saving in computer time and resources.

Based on the above different considerations, a computer code is developed. A simplified flow chart of the code appears in Fig. 2.10

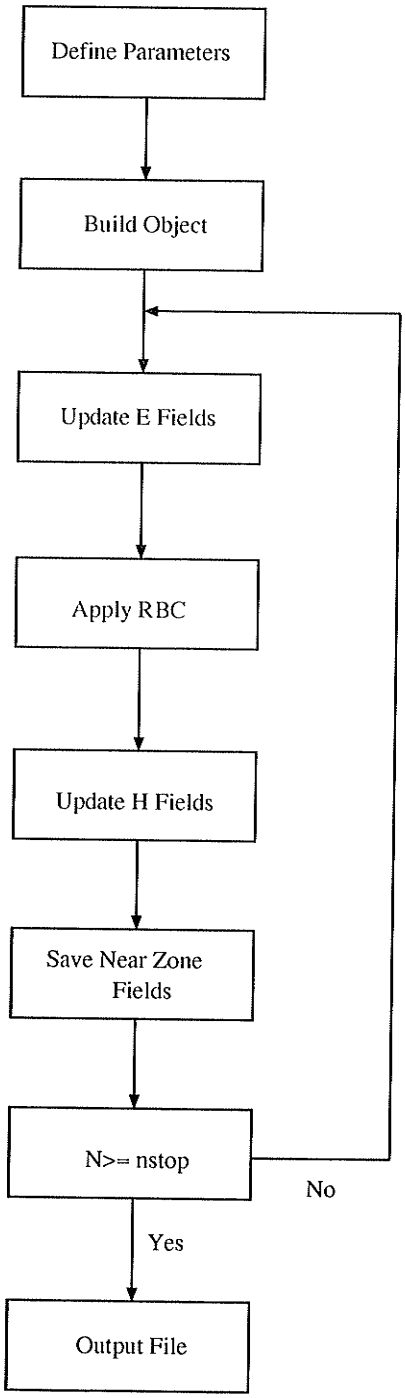

Figure 2.10: Corrected fortran code flow chart after [64].

CHAPTER 3

Radiation Boundary Condition

3.1 Introduction

In many scattering and radiation applications, the structure of interest is situated in an open space. In such cases the radiation condition at infinity should be satisfied, *i.e.*, the scattered or radiated field should propagate into boundless space. However, the FDTD computational space is bounded by necessity. Therefore, scattered or radiated fields arriving at the outermost boundary will be reflected back and will contaminate the interior field quantities. One approach to reduce or eliminate the reflected wave is the application of radiation boundary condition (RBC) at the outermost boundary. This boundary condition acts as an absorber which absorbs arriving waves and simulates an infinite space. Implementing such a boundary condition will reduce the number of cells needed to model the free space surrounding the scatterer or antenna. This will result in a corresponding saving in computer time and resources. Recent research work on RBC focus on the development of techniques that reduce the reflection coefficient at the outer boundary surface. A newly developed absorbing boundary condition, called perfectly matched layer (PML), has been developed by Berenger [58] and extended to 3-D geometries by Katz *et. al*, [59].

The need for an RBC in open space problem can be illustrated by considering field components at the outermost boundary of the computational space. Such field components can not be updated using the regular FDTD equations discussed in

Sec. 2.1.2 because they require knowledge of some field components out side the computational space.

A partial differential equation which permits wave propagation only in a certain direction is called a "one-way wave equation". Absorbing boundary conditions are, therefore, obtained by starting from the wave equation and deriving a one-way wave equation from it that allows propagation in the outward direction only. This chapter will develop the theory and numerical implementation of three useful radiation conditions. These are the Mur radiation boundary condition, the higher order radiation boundary condition, and the modified or super-absorption boundary condition. Numerical experiments will be conducted to show the validity and to compare the accuracy of the three schemes.

3.2 Mur Radiation Boundary Condition

The derivation of Mur radiation boundary condition, can be explained in terms of a differential operator factoring [18]. Consider the two-dimensional wave equation in Cartesian coordinates,

$$U_{xx} + U_{yy} - c^{-2}U_{tt} = 0 \tag{3.1}$$

where U is any scalar field component, the subscripts xx, yy, and tt denote second partial derivatives with respect to x, y, and t, respectively; and c is the wave phase velocity. Applying the partial differential operator to the two-dimensional wave equation one obtains,

$$L = D_x^2 + D_y^2 - c^{-2}D_t^2 = 0 \tag{3.2}$$

which can be given in a simpler form as,

$$LU = 0 \tag{3.3}$$

The operator L can be factored into two operators representing (+) traveling and (−) traveling waves as follow,

$$LU = L^{+}L^{-}U = 0 \tag{3.4}$$

where

$$L^{-} = D_x - \frac{D_t}{c}\sqrt{1 - s^2} \tag{3.5}$$

with

$$s = \frac{D_y}{(D_t/c)} \tag{3.6}$$

The operator, L^{+}, is defined similarly except for a " + " sign before the radical.

It has been shown by [60] that at a grid boundary, $x = 0$, the application of L^{-} to the wave function, U, will exactly absorb a plane wave propagating toward the boundary at an arbitrary angle θ, Fig. 3.1.

Therefore, L^{-}, applied at $x = 0$ functions, simulates an exact analytical radiation boundary condition which absorbs waves propagating toward the boundary $x = 0$ from the interior of the computational domain. The operator L^{+}, is performing the same function for a wave propagating at an arbitrary angle toward the other x boundary at $x = h$, Fig. 3.1.

The operators derived here are non-local in both space and time, this is due to the presence of the radical in (3.5). This would prohibit the direct numerical implementation of $L^{-}U = 0$ as an RBC. This difficulty can be overcome by approximating the radical by a Taylor series expansion. A two-term expansion would take

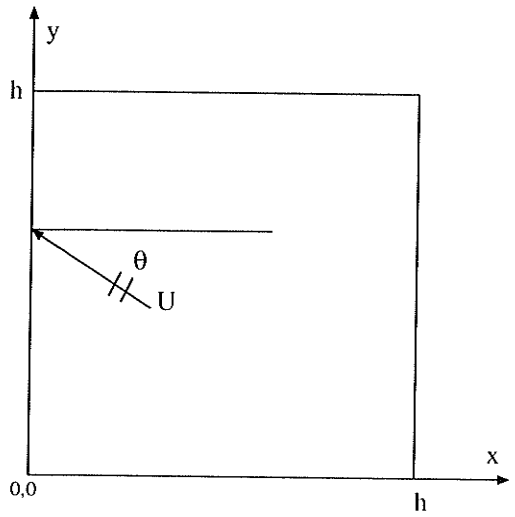

Figure 3.1: 2-D computational domain for RBC application.

the following form,

$$\sqrt{1-s^2} \simeq 1 - \frac{1}{2}s^2 \tag{3.7}$$

Substituting (3.7) into (3.5) for the negative operator, and multiplying the resulting equation by D_t, one obtains the following approximate analytical RBC, which can be numerically implemented at $x = 0$. Such an approximation is called Mur's second absorbing boundary condition.

$$U_{xt} - \frac{1}{c}U_{tt} + \frac{c}{2}U_{yy} = 0 \tag{3.8}$$

However, if the radical is to be approximated by a single-term Taylor series, this will result in Mur's first order boundary condition which takes the following form,

$$U_x - \frac{1}{c}U_t = 0 \tag{3.9}$$

Analogous approximation to other grid boundaries can be derived; *i.e.* $x = h, y = 0$, and $y = h$.

Extension of the above derivation into three-dimension is a simple task and it follows the above development closely. Thus, the approximate analytical RBC,

which can be numerically implemented at boundary surfaces in the three dimension grid are,

$$U_{xt} - \frac{1}{c}U_{tt} + \frac{c}{2}U_{yy} + \frac{c}{2}U_{zz} = 0 \qquad x = 0 \tag{3.10}$$

and

$$U_{xt} + \frac{1}{c}U_{tt} - \frac{c}{2}U_{yy} - \frac{c}{2}U_{zz} = 0 \qquad x = h \tag{3.11}$$

similar equations for y and z boundary surfaces can be obtained.

These approximate representations of an RBC have been found to be very effective when implemented using the differencing scheme proposed by Mur [54]. A detailed discussion on the implementation of the approximate RBC equations is discussed in [54] and [61]. As an application of such approximations to electromagnetic problems, (3.9) and (3.10) will be discretized for E_z, at $x = 0$, in the following manner for a three-dimensional grid:

First order Mur absorbing boundary condition,

$$\begin{aligned} E_z^{n+1}(0, j, k+1/2\ \ ) &= E_z^n(1, j, k+1/2) \\ &+ \frac{c_o\Delta t - \Delta x}{c_o\Delta t + \Delta x}(E_z^{n+1}(1, j, k+1/2) - E_z^n(0, j, k+1/2)) \end{aligned} \tag{3.12}$$

Second order Mur absorbing boundary condition,

$$\begin{aligned} E_z^{n+1}(0, j, k+1/2\ \ ) &= -E_z^{n-1}(1, j, k+1/2) \\ &+ \frac{c_o\Delta t - \Delta x}{c_o\Delta t + \Delta x}(E_z^{n+1}(1, j, k+1/2) - E_z^{n-1}(0, j, k+1/2)) \\ &+ \frac{2\Delta x}{c_o\Delta t + \Delta x}(E_z^n(0, j, k+1/2) - E_z^n(1, j, k+1/2)) \\ &+ \frac{\Delta x(c_o\Delta t)^2}{2(\Delta y)^2(c_o\Delta t + \Delta x)}(E_z^n(0, j+1, k+1/2) - 2E_z^n(0, j, k+1/2) \\ &+ (E_z^n(0, j-1, k+1/2) + E_z^n(1, j+1, k+1/2) \\ &- 2E_z^n(1, j, k+1/2) + E_z^n(1, j-1, k+1/2)) \end{aligned}$$

$$+\frac{\Delta x(c_o\Delta t)^2}{2(\Delta z)^2(c_o\Delta t+\Delta x)}\,(E_z^n(0,j,k+3/2)-2E_z^n(0,j,k+1/2)$$
$$+(E_z^n(0,j,k-1/2)+E_z^n(1,j,k+3/2)$$
$$-2E_z^n(1,j,k+1/2)+E_z^n(1,j,k-1/2)) \tag{3.13}$$

3.3 Generalized and Higher Order RBC

It is evident from the previous section that the approximation of the one-way wave equation is dependent on the order of approximating the radical $\sqrt{1-s^2}$. However, the order of approximation affects the accuracy of the numerical solution. Therefore, a higher-order approximation to the radical will result in a better accuracy of the numerical solution [62].

Trefethen and Halpern [63] proposed a generalization of the two-term Taylor series approximation to the radical, using the rational function approximation

$$\sqrt{1-s^2}\simeq\frac{p_m(s)}{q_n(s)}=\frac{p_0+p_2s^2+\cdot}{1+q_2s^2+\cdot} \tag{3.14}$$

where p_m and q_n are polynomials in s of degree m and n, respectively. It is clear that (3.14) reduces to Mur's first order approximation of the radical by selecting $m=1,n=0$ and $p_0=1$, called type (1,0) and reduces to Mur's second order approximation by choosing $m=2,n=0$, $p_0=1$ and $p_2=-1/2$ called type (2,0). The use of the general type $(2,2)$ rational function

$$\sqrt{1-s^2}\simeq\frac{p_0+p_2s^2}{1+q_2s^2} \tag{3.15}$$

gives the general third-order, approximate, analytical RBC in two-dimensions

$$U_{xtt}+q_2c^2U_{xyy}-\frac{p_0}{c}U_{ttt}-p_2cU_{tyy}=0 \tag{3.16}$$

which takes the discretized form for use in finite-differencing for any field components U at $x=0$ as follows:

$$
\begin{aligned}
U^{n+1}(0,j) &= U^{n-2}(1,j) + c_1(U^{n+1}(1,j) - U^{n-2}(0,j)) \\
&+c_2(U^n(0,j) + U^{n-1}(0,j) - U^n(1,j) - U^{n-1}(1,j)) \\
&+c_3(U^n(0,j) + U^n(1,j) - U^{n-1}(1,j) - U^{n-1}(0,j)) \\
&+c_4\,(U^n(1,j+1) - 2U^n(1,j) + U^n(1,j-1) \\
&-U^n(0,j+1) + 2U^n(0,j) - U^n(0,j-1) \\
&+U^{n-1}(1,j+1) - 2U^{n-1}(1,j) + U^{n-1}(1,j-1) \\
&-U^{n-1}(0,j+1) + 2U^{n-1}(0,j) - U^{n-1}(0,j-1)\Big) \\
&-c_5\,(U^n(1,j+1) - 2U^n(1,j) + U^n(1,j-1) \\
&+U^n(0,j+1) - 2U^n(0,j) + U^n(0,j-1) \\
&-U^{n-1}(1,j+1) + 2U^{n-1}(1,j) - U^{n-1}(1,j-1) \\
&-U^{n-1}(0,j+1) + 2U^{n-1}(0,j) - U^{n-1}(0,j-1)\Big)
\end{aligned}
\tag{3.17}
$$

where

$$
\begin{aligned}
c_1 &= \frac{c\Delta t/\Delta - p_0}{c\Delta t/\Delta + p_0} \\
c_2 &= \frac{c\Delta t/\Delta}{c\Delta t/\Delta + p_0} \\
c_3 &= \frac{3p_0}{c\Delta t/\Delta + p_0} \\
c_4 &= \frac{q_2(c\Delta t/\Delta)^3}{c\Delta t/\Delta + p_0} \\
c_5 &= \frac{p_2(c\Delta t/\Delta)^2}{c\Delta t/\Delta + p_0}
\end{aligned}
\tag{3.18}
$$

Where Δ is the space increment. Appropriate selection of p and q coefficients produces various families of RBC's [62]. For example, taking $p_0 = 1, p_2 = -3/4$ and $q_2 = -1/4$ gives the Pade $(2,2)$ approximation. Absorbing boundary conditions

with higher degrees of interpolation, *i.e.* four and five, can be obtained by replacing the radical, respectively, by

$$\sqrt{1-s^2} \simeq \frac{p_0 + p_2 s^2 + p_4 s^4}{1 + q_2 s^2} \tag{3.19}$$

$$\sqrt{1-s^2} \simeq \frac{p_0 + p_2 s^2 + p_4 s^4}{1 + q_2 s^2 + q_4 s^4} \tag{3.20}$$

The derivation of such approximation and their implementation will not be pursued here due to their complicated form.

3.4 Super-absorbing Boundary Condition

Generally speaking, most practical absorbing boundary conditions usually cannot absorb outgoing waves completely. In return a reflection error will propagate back into the computational domain, which will result in some error. This is due to the approximate representation of the one-way wave equation. Although most schemes proved to be good absorbers and obtained an accurate solution, however, in some cases such as, printed circuit, and microstrip structures, they fail to provide very good accuracy. This is because such structures adopt a high resonant behavior, also waves arrive at the outermost boundary at different velocities. Thus, better absorbing boundary conditions, not only will result in a more accurate numerical solution, but outer boundaries can be brought closer to the modeled structures, resulting in considerable savings on computer memory space and computation time.

The super-absorbing boundary condition is a scheme which works on reducing the error resulting from the imperfect boundary conditions, and to minimize wave

propagation back into the computational domain [64]. To understand how the super-absorption technique works, consider the transverse magnetic (TM) wave in two-dimensions space. In this case only three field components will be present namely, E_z, H_x and H_y. These field components can be updated using the usual FDTD technique,

$$E_z^n(i,j) = E_z^{n-1}(i,j) + \quad c_1 \left[H_y^{n-1/2}(i+1/2,j) - H_y^{n-1/2}(i-1/2,j) \right.$$
$$\left. - H_x^{n-1/2}(i,j+1/2) + H_x^{n-1/2}(i,j-1/2) \right] \quad (3.21)$$

$$H_x^{n+1/2}(i,j+1/2) = H_x^{n-1/2}(i,j+1/2) + c_2 \left[E_z^{n-1}(i,j) - E_z^{n-1}(i,j+1) \right] \quad (3.22)$$

$$H_y^{n+1/2}(i+1/2,j) = H_y^{n-1/2}(i+1/2,j) + c_2 \left[E_z^{n-1}(i+1,j) - E_z^{n-1}(i,j) \right] \quad (3.23)$$

where

$$c_1 = \Delta t/\varepsilon\Delta$$
$$c_2 = \Delta t/\mu\Delta$$

The location of these field components is illustrated in Fig 3.2, in the following formulation the term 1/2 will be dropped out from the H-field components for simplicity. Assuming the line at which $i = M$ is the outer boundary, and from (3.21)–(3.23) it is clear that only E_z components need to be computed, while the H_x components on the same boundary do not affect the computation of internal variables. The discussion will be limited to this boundary only since other boundaries can be treated in the same way.

Usually E_z at this boundary is updated using a radiation boundary treatment, as discussed in the previous two sections. However, due to the imperfection of

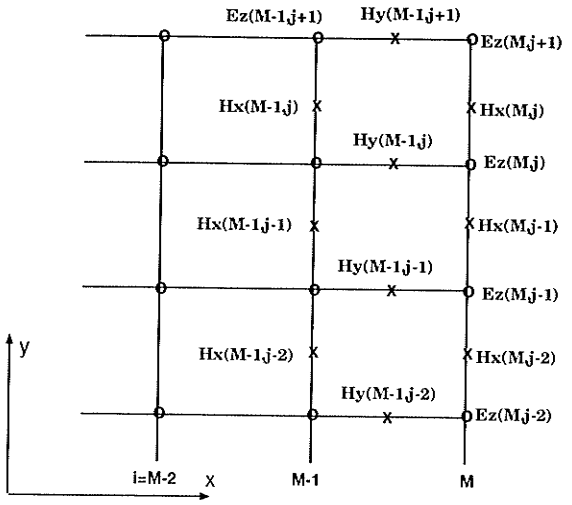

Figure 3.2: Two-dimensional finite-difference grid.

available absorbing boundary schemes, a reflected error will propagate back into the computational domain, which will result in a less accurate solution of the internal points. This propagation is due to the update of the H_y field components just inside this boundary. Assume $E_z^{n(b)}$ is updated by an absorbing boundary condition, and $E_z^{n(e)}$ is the solution as if an infinite space is present, *i.e.*, no boundary limitation, at $i = M$. The error produced by the presence of an absorbing boundary condition can be denoted as

$$err1 = E_z^{n(b)}(M, i) - E_z^{n(e)}(M, i) \tag{3.24}$$

As usual the computed $E_z^{n(b)}$ is used to update $H_y^{n+1/2}$ using the difference equation (3.23), and it would take the following form

$$H_y^{n+1/2}(M-1, j) = H_y^{n-1/2} + c_2 \left[E_z^{n(b)}(M, j) - E_z^n(M-1, j) \right] \tag{3.25}$$

where $H_y^{n+1/2}$ contains the error passed on by $E_z^{n(b)}$. Upon substituting (3.24) into (3.25) the updating equation for $H_y^{n+1/2}$ will take the form,

$$H_y^{n+1/2(1)}(M-1, j) = H_y^{n+1/2(e)}(M-1, j) + c_2 err1 \tag{3.26}$$

where $H_y^{n+1/2(e)}$ is the solution with no boundary condition.

Let the boundary condition applied to $E_z^{n(b)}$ be applied to $H_y^{n+1/2}$, and denote the value computed by the boundary condition as $H_y^{n+1/2(2)}$. The error for $H_y^{n+1/2}$ can be given as,

$$err2 = H_y^{n+1/2(2)}(M-1,i) - H_y^{n+1/2(e)}(M-1,i) \tag{3.27}$$

The two errors, err1 and err2, are not independent, they are related by the same relation that relates E_z^n and $H_y^{n+1/2}$, since the same absorbing boundary is applied to both quantities [61]. The relation between E_z and H_y, derived in Appendix A, is

$$H_y = -c_{TM} E_z \tag{3.28}$$

where

$$c_{TM} = \frac{c_2 \sin \frac{k_x \Delta}{2}}{\sin \frac{\omega \Delta t}{2}} \tag{3.29}$$

Thus, using (3.26),(3.27) and (3.28), and by eliminating the errors, one gets

$$H_y^{n+1/2(e)}(M-1,j) = \frac{c_{TM} H_y^{n+1/2(1)}(M-1,j) + c_2 H_y^{n+1/2(2)}(M-1,j)}{c_{TM} + c_2} \tag{3.30}$$

The solution of H_y obtained from (3.30) contains no reflection error. However, this solution can not be implemented numerically due to the presence of c_{TM}. Therefor, some approximations have to be done. In order to ensure the accuracy of the solutions, the grid size Δ is chosen to be small enough so that

$$\Delta \leq \lambda/10 \tag{3.31}$$

which makes

$$k_x \Delta \ll 1$$

$$\omega \Delta t \ll 1$$

Therefore

$$c_{TM} = \frac{c_2 \sin\frac{k_x\Delta}{2}}{\sin\frac{\omega\Delta t}{2}} \approx c_2\frac{k_x\Delta}{\omega\Delta t} = c_2\left(\frac{\Delta}{c\Delta t}\right)\frac{k_x}{k} = c_2\left(\frac{\Delta}{c\Delta t}\right)\cos\theta \quad (3.32)$$

where c is the speed of light in the medium. With these approximations (3.30) can be rewritten as

$$H_y^{n+1/2(e)}(M-1,j) = \frac{\cos\theta H_y^{n+1/2(1)}(M-1,j) + \rho H_y^{n+1/2(2)}(M-1,j)}{\cos\theta + \rho} \quad (3.33)$$

where

$$\rho = \frac{c\Delta t}{\Delta}$$

In many applications, the incident angle θ of the out going wave is unknown. Equation (3.33) can be simplified further by assuming the wave is normally incident on the boundary,

$$H_y^{n+1/2(e)}(M-1,j) = \frac{H_y^{n+1/2(1)}(M-1,j) + \rho H_y^{n+1/2(2)}(M-1,j)}{1+\rho} \quad (3.34)$$

Using (3.34) will produce less reflection error in H_y, however, E_z is still less accurate and contains the original error resulted from the absorbing boundary. A more accurate E_z can be obtained by recalculating its more accurate value using (3.21), which contains the more accurate value of H_y obtained from (3.34).

$$E_z^n(M,j) = E_z^{n-1}(M-1,j) + \frac{1}{c_2}\left[H_y^{n-1/2}(M-1,j) - H_y^{n-1/2}(M-1,j)\right] \quad (3.35)$$

This step is necessary for some absorbing boundary conditions in which $E_z^n(M,j)$ is used as a previous value to update and compute $E_z^{n+1}(M,j)$. In summary, the procedure of the super-absorption technique for the outer boundary at $i = M$ for a TM wave as given in [61] is as follows:

- Choose an absorbing boundary condition on boundary nodes $E_z^n(M, j)$.
- Compute $H_y^{n+1/2}(M-1, j)$ using the regular finite-difference scheme to obtain $H_y^{n+1/2(1)}(M-1, j)$.
- Apply the same absorbing boundary condition, used with E_z, on H_y to obtain $H_y^{n+1/2(2)}(M-1, j)$.
- Recalculate H_y using (3.34).
- Recalculate E_z using (3.35).

For the two-dimensional TE case the super-absorption technique is applied in the same procedure as for the TM case, with the exception that the operations will be applied on H_z, E_x and E_y instead of E_z, H_x and H_y. Similarly in three-dimensions space, the procedure will follow exactly the two-dimensional case, except that the super-absorption operations are applied on two pairs of nodes, *i.e.*, for the surface $i = M$, one pair is found by the $E_z(M, j, k)$ and $H_y(M-1, j, k)$ nodes, the second pair is found by the $E_y(M, j, k)$ and $H_z(M-1, j, k)$ nodes.

3.5 Comparison and Numerical Tests

In this section numerical simulations are performed to test and compare the accuracy of the RBC's considered in the previous sections. The analysis for two-dimensional problems is similar to the one applied by Moor *et al.* [61] and [62]. Fig. 3.3 shows two domains on which the two-dimensional FDTD algorithm is computed for the transverse magnetic TM_z case. Ω_l is the larger domain whereas Ω_s is the smaller one. Ω_l is used to simulate an infinite space, this can be accomplished by choosing an observation time domain shorter than the time needed for the wave

to reach the outer boundary, this way there will be no reflection error propagating back into the computational domain. On the boundaries of the domain Ω_s, RBC's considered in the previous section are applied.

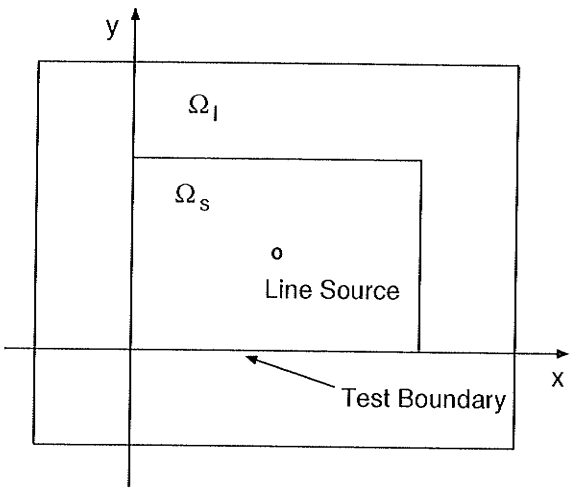

Figure 3.3: 2-D computational domain for numerical experimentation.

A line source is located in the center in both domains; grid position $(25, 25)$ in the smaller domain. The computational space for the smaller domain is taken to be 50×50, while the larger domain has a computational space of 400×400. By calculating the difference between the solutions in the two domains a measure of the reflection caused by the boundary of Ω_l is obtained. At each time step the difference is defined to be.

$$err(i,j) = E_z^s(i,j) - E_z^l(i,j) \tag{3.36}$$

The pulse used in this analysis is the same as the one used by [61], and it is defined as;

$$E_z^n(25,25) = \begin{cases} \alpha(10 - 15\cos\omega_1\xi + 6\cos\omega_2\xi - \cos\omega_1\xi) & \xi \leq \tau \\ 0 & \xi > \tau \end{cases} \tag{3.37}$$

where

$$\alpha = \frac{1}{320} \qquad \tau = 10^{-9}, \xi = n\Delta t$$
$$\omega_m = \frac{2\pi m}{\tau} \qquad m = 1, 2, 3$$

and $\Delta t = \Delta/2c = 25.0ps$ is the time step used. Such selection of the time step restricts the wave to travel one space cell in two time steps. The source point in Fig. 3.3 is 25 cells away from the lower boundary of Ω_s at $y = 0$. Therefore, it takes the wave 50 time steps to arrive at the outer boundary of Ω_s at $y = 0$. An observation point along the x-axis, one cell above the lower boundary of Ω_s at $y = \Delta$ and at $t = 80\Delta t$, is chosen to study the local error defined by (3.36). The time profile of the compact pulse is shown in Fig. 3.4.

The experiment is carried out for five types of RBCs, these are: a hard boundary condition, where the outer boundary tangential electric field components are set to zero, $E_z = 0$; a first order Mur type; a second order Mur type, a third order RBC with $p_0 = 1, p_2 = -3/4$ and $q_2 = -1/4$, which is called Pade's $(2,2)$ approximation; and lastly, the super-absorption technique is applied along with the hard boundary and Mur's first order type.

Three sets of results have been obtained. Figs. 3.6– 3.11, compare the behavior of the wave along the x-axis at the lower boundary of the y–axis, $y = \Delta$, at $t = 80\Delta t$. It is clear from Fig. 3.6 that a great amount of reflection is propagating back into the grid. However, a significant reduction in this reflection error is observed in Fig. 3.7, which corresponds to the use of Mur's first RBC. Moreover, the behavior

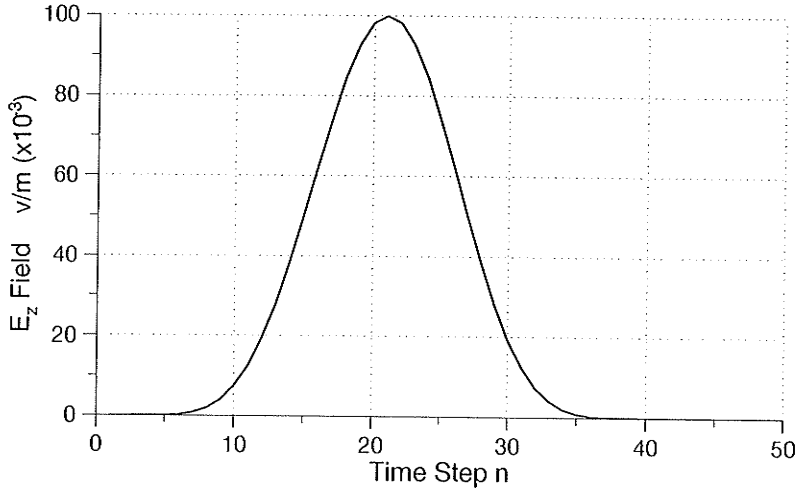

Figure 3.4: Compact pulse wave source.

has improved further as the order of approximation increases, as shown in Figs. 3.8– 3.9. It should be mentioned here that, such improvement will add to the cost of the code in terms of space memory and computation time, also one should be careful in using the higher order approximation. The reason for this will be discussed later in this section.

The application of the super-absorption technique is illustrated in Figs. 3.10– 3.11. One can easily observe the improvement in the performance of the hard and Mur's first RBC's after the introduction of the super-absorption technique.

The second test is done through the use of Eq.(3.36). Results are shown in Figs. 3.12– 3.13, and illustrate the local error produced using RBC's under study. The test, again, is performed along the x-axis at the lower boundary of the y–axis, $y = \Delta$ and $t = 80\Delta t$.

The last test is performed at node $(25, 1)$ for 260 time steps, the purpose of

this test is to examine the performance of the RBC's under discussion over a period of time. Figs. 3.14– 3.18 illustrate the effect of using a higher order RBC's. It is clear that as time progresses, the reflected error increases with the higher order approximation RBC's. This is due to the imperfection of the RBC's, which will result in some reflection, error, back into the domain. This error, in some cases, accumulates and adds up as time progresses.

The same tests have been conducted for the three-dimensions case, however, only the results which reflect the amount of error will be shown. The domain space is taken to be $50 \times 50 \times 50$ cells. A Gaussian point source located in the center of the domain is used to excite the grid. Results in Figs. 3.19– 3.20 are observed along the line $y = \Delta, z = 25$ and $x = i$, *i.e.*, at $(i, \Delta, 25)$, where $\Delta = 5\ mm$ is used along with the Courant condition $\Delta t = \Delta/2c$ with c the speed of light in free space. The Gaussian pulse used for this experiment is shown in Fig. 3.5.

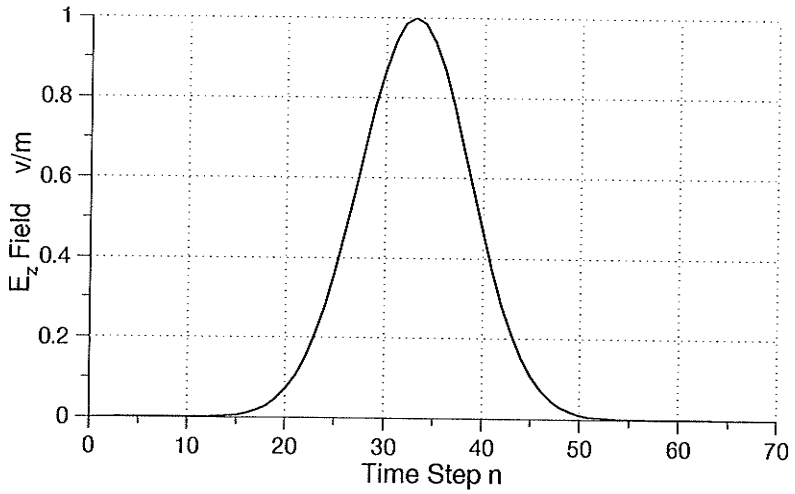

Figure 3.5: Gaussian pulse wave source.

2-D Results

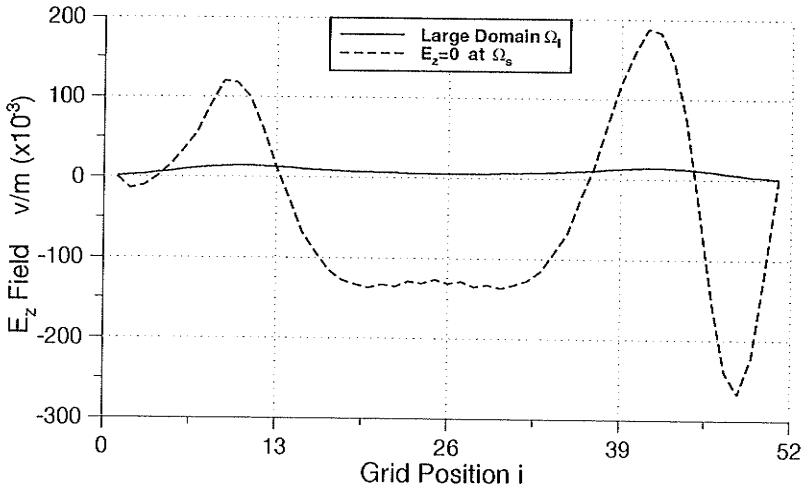

Figure 3.6: E_z field at points (i,1) and $t = 80\Delta t$ computed in the larger and smaller domain. The smaller domain is truncated with $E = 0$ RBC.

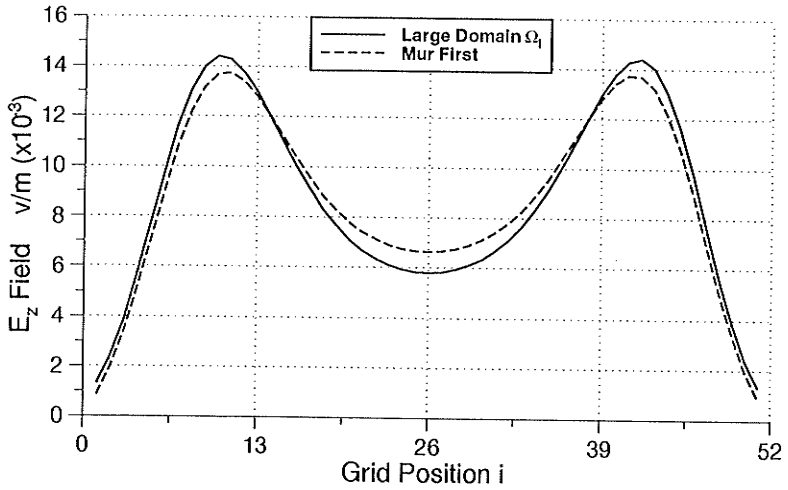

Figure 3.7: E_z field at points (i,1) and $t = 80\Delta t$ computed in the larger and smaller domain. The smaller domain is truncated with Mur first order RBC.

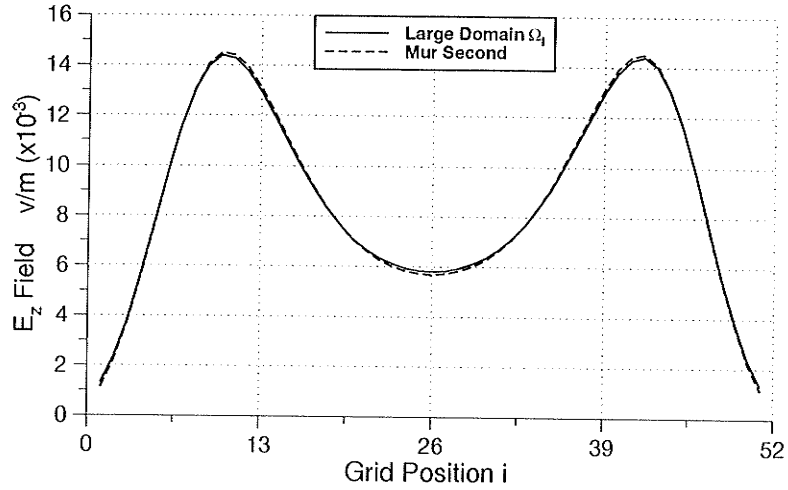

Figure 3.8: E_z field at points (i,1) and $t = 80\Delta t$ computed in the larger and smaller domain. The smaller domain is truncated with Mur second order RBC.

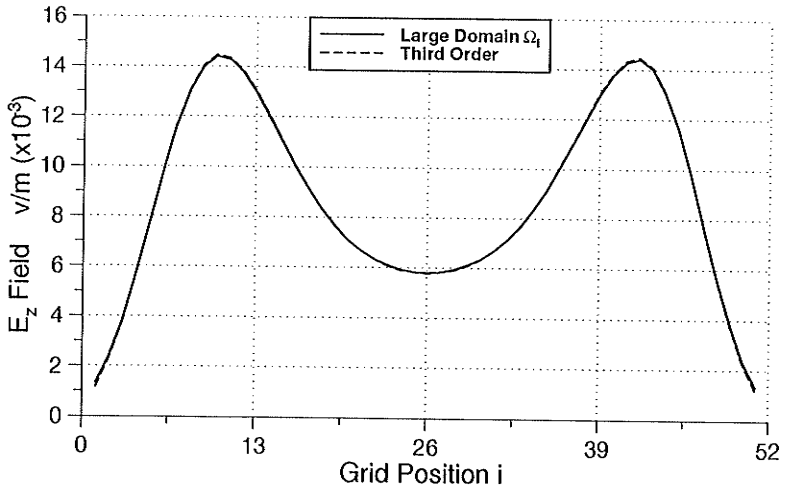

Figure 3.9: E_z field at points $(i, 1)$ and $t = 80\Delta t$ computed in the larger and smaller domain. The smaller domain is truncated with third order RBC, $p_0 = 1.0, p_2 = -0.75$ and $q_2 = -0.25$

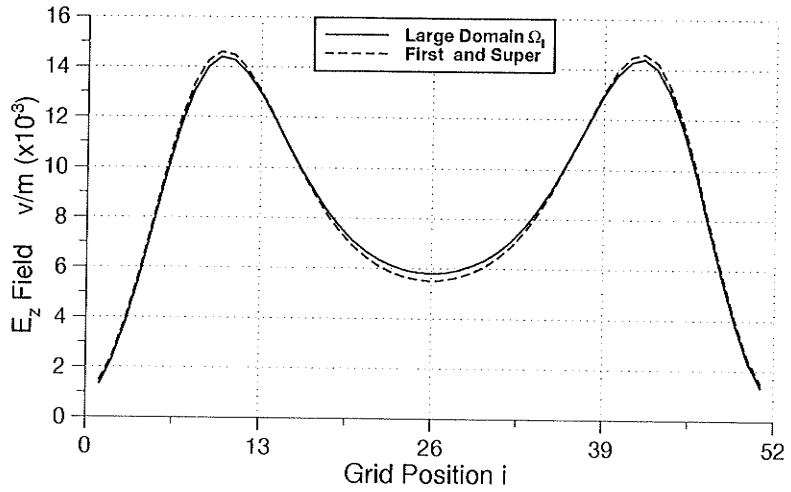

Figure 3.10: E_z field at points (i,1) and $t = 80\Delta t$ computed in the larger and smaller domain. The smaller domain is truncated with $E = 0$ and super-absorption RBC.

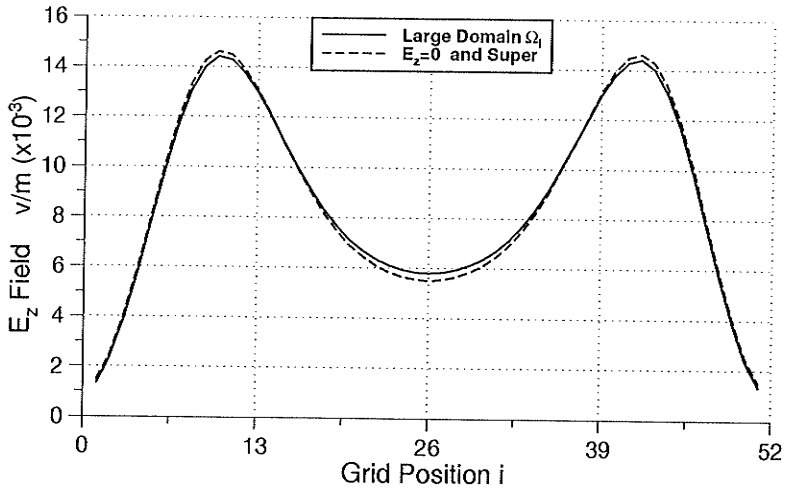

Figure 3.11: E_z field at points (i,1) and $t = 80\Delta t$ computed in the larger and smaller domain. The smaller domain is truncated with Mur first order and super-absorption RBC.

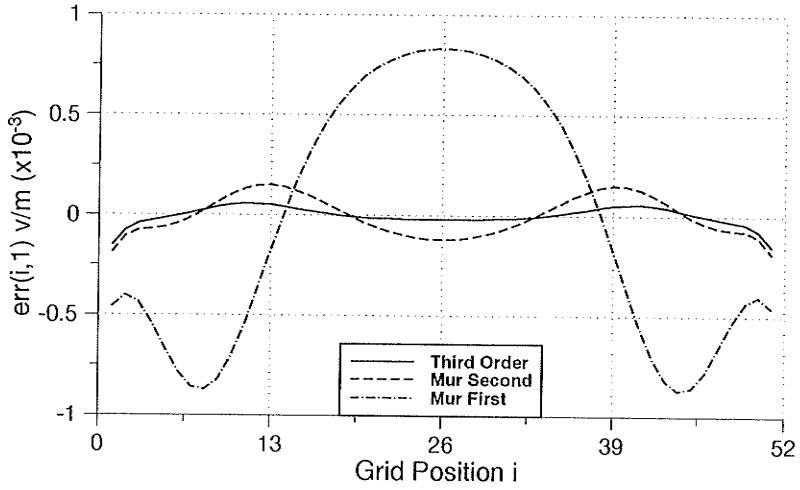

Figure 3.12: Comparison of the reflection error of $E_z(i,1)$ at $t = 80\Delta t$, computed using Mur first, second and third order RBC.

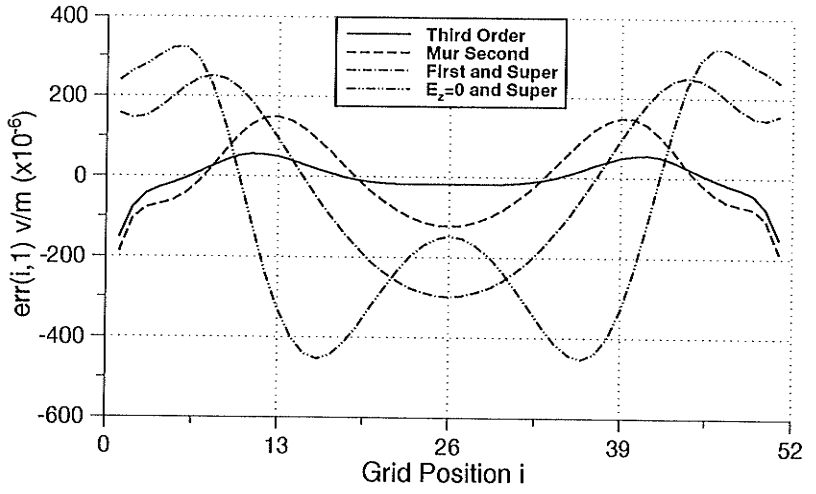

Figure 3.13: Comparison of the reflection error of $E_z(i,1)$ at $t = 80\Delta t$, computed using $E = 0$ and super-absorption, Mur first and super-absorption, Mur second and third order RBC.

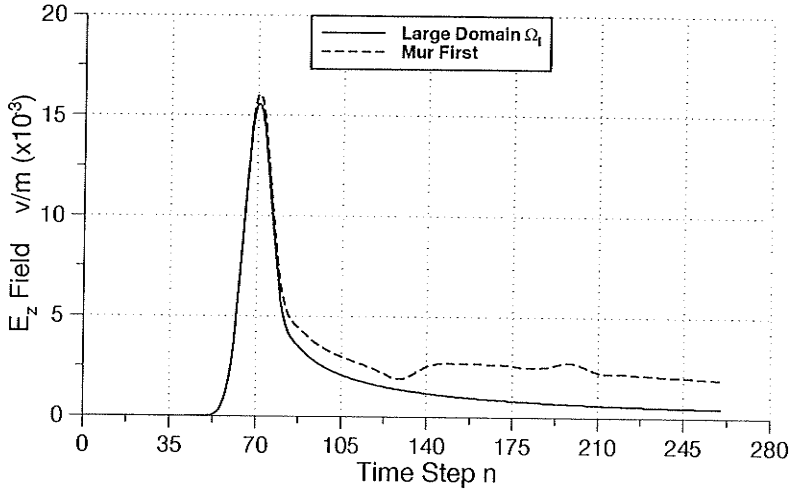

Figure 3.14: Comparison of the time response of $E_z(25, 1)$, computed using the larger domain and the smaller domain truncated using Mur first RBC.

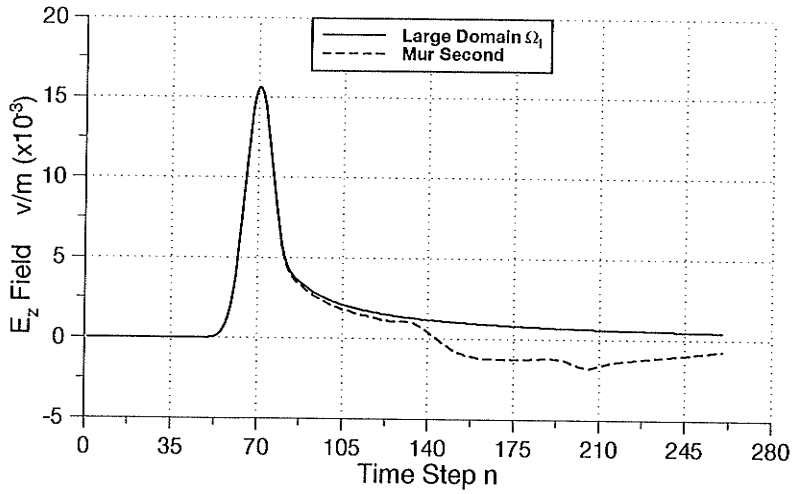

Figure 3.15: Comparison of the time response of $E_z(25, 1)$, computed using the larger domain and the smaller domain truncated using Mur second RBC.

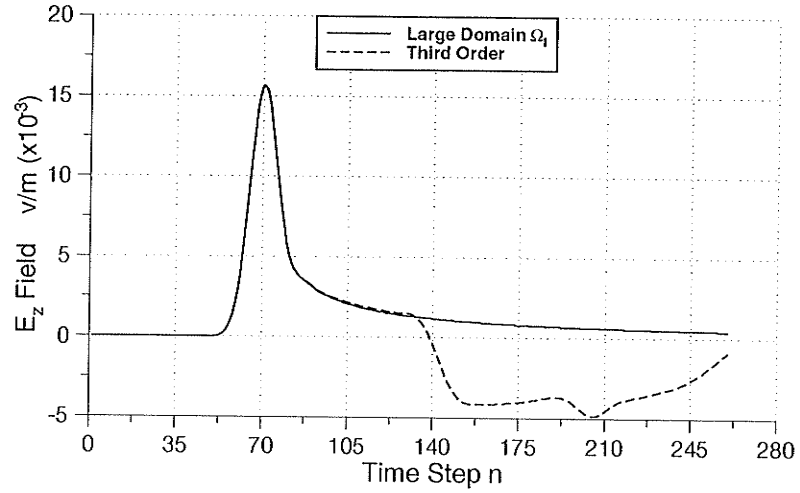

Figure 3.16: Comparison of the time response of $E_z(25, 1)$, computed using the larger domain and the smaller domain truncated using third order RBC.

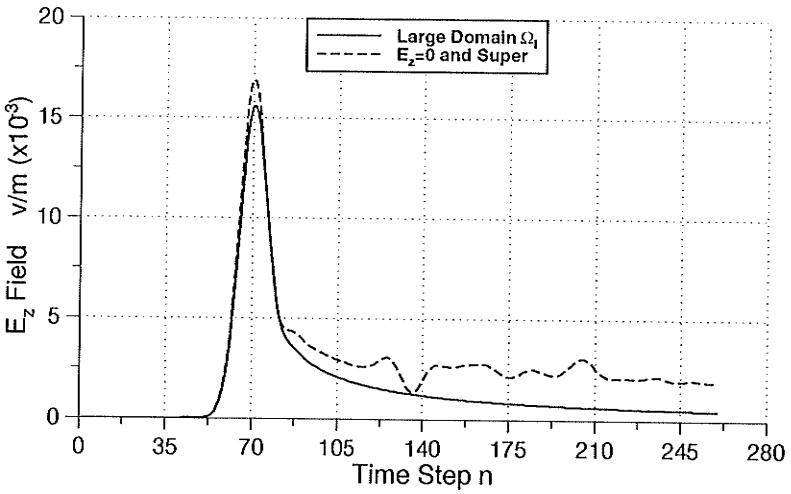

Figure 3.17: Comparison of the time response of $E_z(25, 1)$, computed using the larger domain and the smaller domain truncated using $E = 0$ and super-absorption RBC.

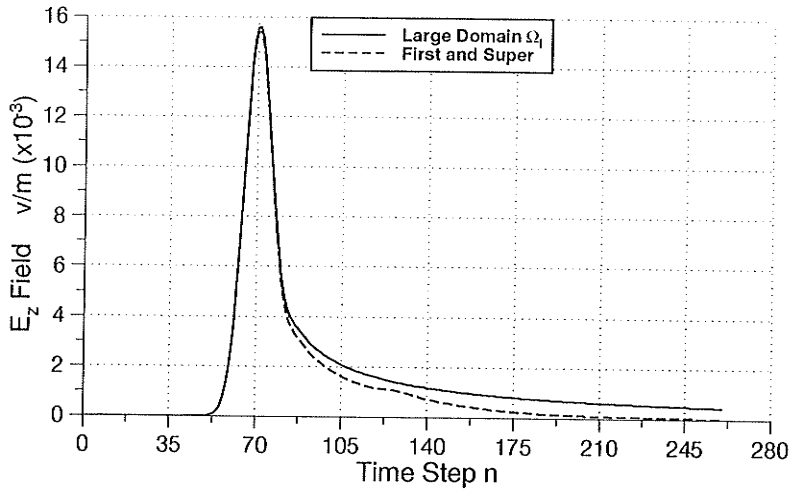

Figure 3.18: Comparison of the time response of $E_z(25, 1)$, computed using the larger domain and the smaller domain truncated using Mur first and super-absorption RBC.

3-D Results

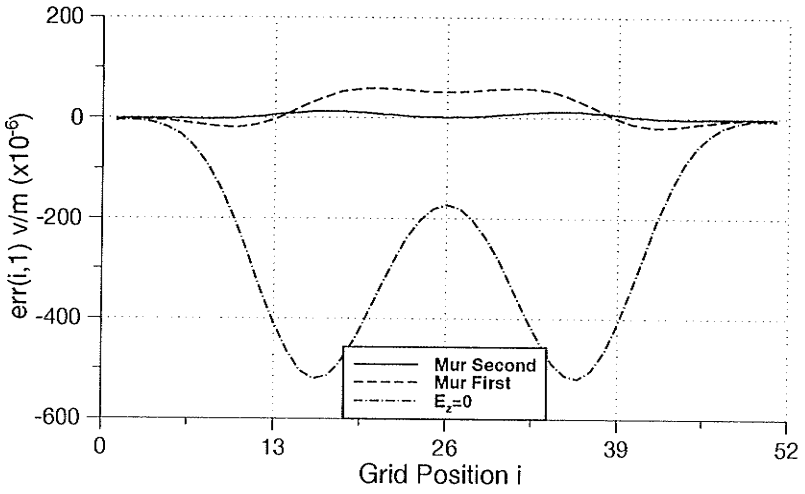

Figure 3.19: Comparison of the reflection error of $E_z(i, 1, 25)$ at $t = 80\Delta t$, computed using $E = 0$, Mur first and second RBC.

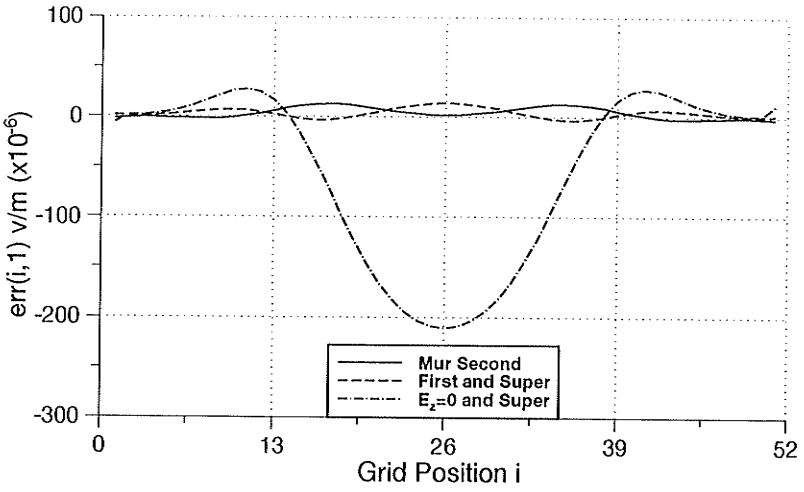

Figure 3.20: Comparison of the reflection error of $E_z(i, 1, 25)$ at $t = 80\Delta t$, computed using $E = 0$ and super-absorption, Mur first and super-absorption and Mur second RBC.

CHAPTER 4

FDTD Special Capabilities

4.1 Introduction

The FDTD method has become increasingly popular in the area of computational electromagnetics, this is due to its computational efficiency, accuracy, direct physical interpretation, and diversity. The last two features are the main scope of this chapter. The Yee algorithm for FDTD was originally interpreted as a direct approximation of the point-wise derivatives of Maxwell's time-dependent curl equations using numerical central differences. However, such development has distinct drawback in modeling fine geometrical structures such as wires, slots, curved surfaces and lumped circuit elements.

Usually these structures are very small in at least one dimension as compared to the main body of the object being modeled. One way to overcome this problem is to reducing the cell size throughout the computational space, however, it is computationally expensive, and impractical if computer resources are inadequate. A more practical way to deal with this situation is to use large FDTD cells throughout the computational space, and approximate the small geometry elements by modifying the large cell field equations. Development of this approach requires the use of Maxwell's equations in integral form. It was shown in Sec. 2.1.3 that the difference

equations could be obtained from the integral form of Maxwell's equations.

In this chapter the contour integral formulation, Sec. 2.1.3, will be extended to model thin wire structure and lumped circuit elements in electromagnetic systems.

4.2 Thin Wire Modeling

Thin wire structures are commonly used in antenna and coupling applications. Usually these wires are much smaller in radius than other structures of the modeled object. Approximating the wire as being the same size as the object modeling cell, may yield poor results, as both antenna impedance and coupling are sensitive to wire radius [53].

In this section the contour integral method [21] is used to approximate the effect of a wire with radius smaller than the FDTD cell on the FDTD updating equations.

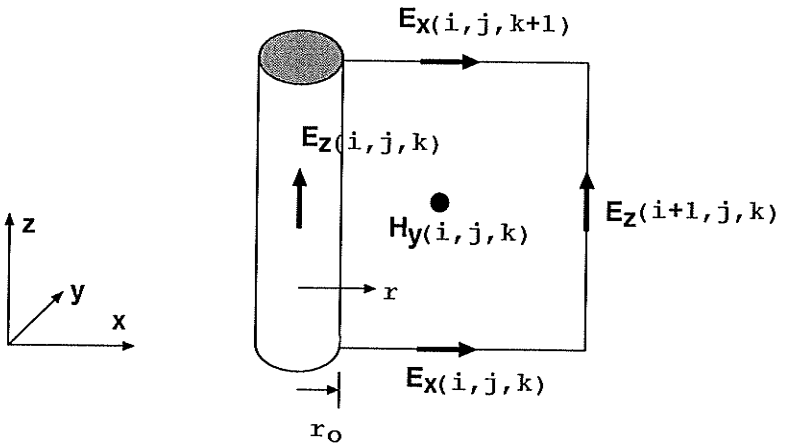

Figure 4.1: Field locations and geometry for thin wire.

Consider the geometry shown in Fig. 4.1, a conducting circular wire of radius r_o

is positioned and centered on the $E_z(i,j,k)$ field component. The wire radius, r_o, is assumed less than $\Delta x/2$, which from the definition of the cell size, $\Delta x \leq \lambda/10$, implies that $r_o \ll \lambda$. Therefore, it can be assumed that the normal electric and circumferential magnetic fields in the vicinity of the wire have $1/r$ dependence, where r is the radial distance from the center of the wire. Thus, the spatial dependence of $H_y(i,j,k)$ within the contour can be approximated as,

$$H_y(r,j,k) \approx \frac{\Delta x}{2r} H_y(i,j,k) \tag{4.1}$$

the electric field $E_x(r,j,k)$ along the upper and lower contours as,

$$E_x(r,j,k) \approx \frac{\Delta x}{2r} E_x(i,j,k) \tag{4.2}$$

with $E_z(i,j,k)$ along the axis of the conducting wire set to $E_z(i,j,k) = 0$, and $E_z(i,j,k)$ is assumed uniform along the right contour.

Application of Faraday's law, Eq. (2.23), to the contour passing through the four electric field locations results in,

$$\begin{aligned} -\mu\Delta z \frac{\partial}{\partial t} \int_{r_o}^{\Delta x} H_y(i,j,k) \frac{\Delta x}{2} \frac{dr}{r} &= 0 - E_z(i+1,j,k)\Delta z \\ + \int_{r_o}^{\Delta x} E_x(i,j,k+1) \frac{\Delta x}{2} \frac{dr}{r} &- \int_{r_o}^{\Delta x} E_x(i,j,k) \frac{\Delta x}{2} \frac{dr}{r} \end{aligned} \tag{4.3}$$

which after evaluating the integrals and approximating the time derivatives as finite differences reduces to

$$\begin{aligned} H_y^{n+1/2}(i,j,k) = H_y^{n-1/2}(i,j,k) &+ \frac{2\Delta t}{\mu\Delta x \ln(\Delta x/r_o)} E_z^n(i+1,j,k) \\ &+ \frac{\Delta t}{\mu\Delta z} \left[E_x^n(i,j,k) - E_x^n(i,j,k+1)\right] \end{aligned} \tag{4.4}$$

Equation (4.4) is the new updating equation of the magnetic field, H_y at (i,j,k) in the vicinity of the wire. However, for each $E_z(i,j,k)$ along the thin wire, there are

four H field components associated with it. This requires the derivation of another three equations for updating the remaining magnetic field components and are given by,

$$H_y^{n+1/2}(i-1,j,k) = H_y^{n-1/2}(i-1,j,k) - \frac{2\Delta t}{\mu\Delta x \ln(\Delta x/r_o)} E_z^n(i,j,k) + \frac{\Delta t}{\mu\Delta z}\left[E_x^n(i,j,k) - E_x^n(i,j,k+1)\right] \tag{4.5}$$

$$H_x^{n+1/2}(i,j,k) = H_x^{n-1/2}(i,j,k) - \frac{2\Delta t}{\mu\Delta y \ln(\Delta y/r_o)} E_z^n(i,j+1,k) + \frac{\Delta t}{\mu\Delta z}\left[E_y^n(i,j,k) - E_y^n(i,j,k+1)\right] \tag{4.6}$$

$$H_x^{n+1/2}(i,j-1,k) = H_x^{n-1/2}(i,j-1,k) + \frac{2\Delta t}{\mu\Delta y \ln(\Delta y/r_o)} E_z^n(i,j,k) + \frac{\Delta t}{\mu\Delta z}\left[E_y^n(i,j,k) - E_y^n(i,j,k+1)\right] \tag{4.7}$$

and the electric field components are updated using the usual FDTD equations.

4.3 Lumped Elements Modeling

The modeling of lumped circuit elements in the FDTD algorithm can be accomplished in two ways. One way is to use the integral form of Maxwell's equations, this approach is useful in modeling elements which occupy less than one space cell in the FDTD grid. The second approach is to use the traditional Maxwell's curl equations, this approach is applicable to elements that occupy a single FDTD space cell. Both approaches depend on the physical understanding of the Maxwell equation representation.

Both R, L and C lumped elements and discrete voltage and current sources with internal impedance are modeled. By specifying the appropriate $I-V$ characteristics of the sources and the elements, both passive and active, linear and nonlinear circuit elements can be treated. Start with Maxwell's equation in the time domain for curl H, *i.e.*,

$$\nabla \times \mathbf{H} = \sigma \mathbf{E} + \varepsilon \frac{\partial \mathbf{E}}{\partial \mathbf{t}} \tag{4.8}$$

To understand the physical meaning of (4.8) consider the E_z component of the electric field surrounded by H_x and H_y magnetic field components.

$$(\nabla \times H)_z = \sigma E_z + \varepsilon \frac{\partial E_z}{\partial t} \tag{4.9}$$

The curl H term in (4.9) represents the total current density flowing in the cell surrounding the electric field component E_z. The σE_z term in the right hand side of (4.9) is the conduction current density flowing through the cell in the z direction. The next term involving ε and the time derivative of E_z is the displacement current density flowing through the cell in the z direction.

Using the cell notation Δx, Δy and Δz and assuming fields are constant across the cell. Multiplying (4.9) by $\Delta x \Delta y$ and inserting appropriate Δz factors, yield

$$\begin{aligned} \Delta x \Delta y (\nabla \times H^{n+1/2})_z = \sigma \frac{\Delta x \Delta y}{\Delta z} \Delta z \frac{E_z^{n+1} + E_z^n}{2} + \\ \varepsilon \frac{\Delta x \Delta y}{\Delta z} \Delta z \frac{E_z^{n+1} - E_z^n}{\Delta t} \end{aligned} \tag{4.10}$$

The first term is the total current flowing in the $\Delta x \Delta y$ area surrounding the E_z field component. The term $\sigma \frac{\Delta x \Delta y}{\Delta z}$ can be identified as the conductance of an FDTD cell for a z component of electric field, and $\varepsilon \frac{\Delta x \Delta y}{\Delta z}$ is the capacitance. The term σE_z in

Eq. (4.9) is obtained from the conduction current J_c and evaluated at $n+1/2$ time step. Therefore, $(E_z^{n+1}+E_z^n)/2$ is used to approximate the term σE_z. If a lumped inductor is to be added in parallel with the capacitor and resistor, Eq. (4.10) will take the following form,

$$\Delta x\Delta y(\nabla\times H^{n+1/2})_z = G\Delta z\frac{E_z^{n+1}+E_z^n}{2} + C\Delta z\frac{E_z^{n+1}-E_z^n}{\Delta t} + \frac{\Delta z}{L}\int_0^{(n+1)\Delta t} E_z dt \qquad (4.11)$$

where L is the lumped inductance in Henries. Assuming E_z constant over a time interval Δt, then the integration can be approximated as a summation, hence the updating equation for E_z will be,

$$E_z^{n+1} = \frac{1-\frac{G\Delta t}{2C}}{1+\frac{G\Delta t}{2C}}E_z^n + \frac{\Delta x\Delta y}{\Delta z(1+\frac{G\Delta t}{2C})}(\nabla\times H^{n+1/2})_z - \frac{\Delta t}{L(1+\frac{G\Delta t}{2C})}\sum_{m=1}^{n} E_z^m \qquad (4.12)$$

Equation (4.10) provides a simple tool for modeling lumped elements, *i.e.* R, and C. No modification of the FDTD equations is required, since the modeling of such passive elements can be accomplished by adjusting the material properties of the cell in which the lumped element is located.

Equation (4.11) can be obtained using an alternative approach by considering the curl H Maxwell's equation in the following form,

$$\nabla\times\mathbf{H} = \mathbf{J_c} + \frac{\partial\mathbf{D}}{\partial\mathbf{t}} + \mathbf{J_l} \qquad (4.13)$$

where $\mathbf{D}=\varepsilon\mathbf{E}$, $\mathbf{J_c}$ is the conduction current density, and $\mathbf{J_l}$ is the lumped element current density. Assuming the lumped element is located in free space at $E_z(i,j,k)$ field point. Keeping in mind the following relations,

$$V = \int_{c_E} E \times dl$$
$$I = \int_{c_H} H \times dl \tag{4.14}$$

equation (4.13) can be given in terms of the total current flowing through the cell as,

$$I = I_l + I_c + I_d \tag{4.15}$$

where I is the total current flowing through the cell in a given direction, $I_l = J_l \Delta x \Delta y$ is the current through the lumped element to be modeled, I_c is the conduction current and I_d is the displacement current. Solving (4.13) for E_z^{n+1} one gets,

$$E_z^{n+1} = E_z^n + \frac{\Delta t}{\varepsilon}(\nabla \times H^{n+1/2})_z - \frac{\Delta t}{\varepsilon \Delta x \Delta y} I_l^{n+1/2} \tag{4.16}$$

I_l, as mentioned earlier, is the lumped element current which can be obtained from the $I - V$ relation. Equation (4.16) is capable of modeling any lumped element, passive, active, linear or nonlinear, as long as the current/voltage relation is known.

The lumped resistor, inductor or capacitor can be modeled easily by substituting into (4.16) the appropriate $I - V$ relations for each component. In finite difference terms these relations take the following forms for a z-directed current for the resistor, inductor, and capacitor, respectively:

$$I_z^{n+1/2}(i,j,k) = \frac{\Delta z}{2R}\left[E_z^{n+1}(i,j,k) + E_z^n(i,j,k)\right] \tag{4.17}$$
$$I_z^{n+1/2}(i,j,k) = \frac{\Delta z \Delta t}{L} \sum_{m=1}^{n} E_z^m(i,j,k) \tag{4.18}$$
$$I_z^{n+1/2}(i,j,k) = \frac{C \Delta z}{\Delta t}\left[E_z^{n+1}(i,j,k) - E_z^n(i,j,k)\right] \tag{4.19}$$

The corresponding updating equations for $E_z(i,j,k)$ are

$$E_z^{n+1}(i,j,k) = \left[\frac{1-\frac{\Delta t\Delta z}{2R\varepsilon_o\Delta x\Delta y}}{1+\frac{\Delta t\Delta z}{2R\varepsilon_o\Delta x\Delta y}}\right] E_z^n(i,j,k) + \left[\frac{\frac{\Delta t}{\varepsilon_o}}{1+\frac{\Delta t\Delta z}{2R\varepsilon_o\Delta x\Delta y}}\right] (\nabla\times H^{n+1/2})_z \tag{4.20}$$

for the resistive lumped element,

$$E_z^{n+1}(i,j,k) = E_z^n(i,j,k) + \left[\frac{\frac{\Delta t}{\varepsilon_o}}{1+\frac{C\Delta z}{\varepsilon_o\Delta x\Delta y}}\right] (\nabla\times H^{n+1/2})_z \tag{4.21}$$

for the capacitive lumped element, and

$$E_z^{n+1}(i,j,k) = E_z^n(i,j,k) + \frac{\Delta t}{\varepsilon_o}(\nabla\times H^{n+1/2})_z - \frac{\Delta z(\Delta t)^2}{\varepsilon_o L\Delta x\Delta y}\sum_{m=1}^{n} E_z^m(i,j,k) \tag{4.22}$$

for the inductive lumped element.

Substituting (4.17)–(4.19) into (4.16) results in an updating equation to model a parallel RLC circuit. Other circuit elements such as a resistive voltage source can be modeled in a similar way. Again assume a z-directed lumped element located in free space at $E_z(i,j,k)$, the $I-V$ relation that describes the behavior of a resistive voltage source can be expressed in the following form,

$$I_z^{n+1/2}(i,j,k) = \frac{\Delta z}{2R_s}\left[E_z^{n+1}(i,j,k) + E_z^n(i,j,k)\right] + \frac{V_s^n}{R_s} \tag{4.23}$$

where V_s^n is the source voltage and R_s is the internal source resistance.

For a nonlinear circuit element, such as diode, the current flowing through the diode is expressed by,

$$I_d = I_0\left[\exp\left(qV_d/kT\right) - 1\right] \tag{4.24}$$

where q is the charge of an electron, V_d is the voltage across the diode, k is Boltzman's constant, and T is the temperature in degrees Kelvin. Expressing the diode voltage using field representation as,

$$V_d = \frac{\Delta z}{2}\left[E_z^{n+1}(i,j,k) + E_z^n(i,j,k)\right] \tag{4.25}$$

hence, the updating field equation for a diode lumped element will be the following transcendental equation:

$$E_z^{n+1}(i,j,k) = E_z^n(i,j,k) + \frac{\Delta t}{\varepsilon_o}(\nabla \times H^{n+1/2})_z - \frac{\Delta t}{\varepsilon_o \Delta x \Delta y} \cdot I_0\left\{\exp\left[-q\left(E_z^{n+1}(i,j,k) + E_z^n(i,j,k)\right)\Delta z/2kT\right] - 1\right\} \tag{4.26}$$

4.4 Numerical Application

In this section application of the theory presented in the previous two sections will be demonstrated. The first application to be considered is the effect of the wire approximation on the accuracy of the input current and impedance of a wire dipole antenna. Comparison with the method of moments (MoM) is also demonstrated.

The wire is of 57 cm length and 0.281 cm radius. The problem space for the one cell approximation is $51 \times 51 \times 81$ cells, with the cell dimensions $\Delta x = \Delta y = 0.5cm$ and $\Delta z = 1.0cm$. The two transverse dimensions are selected $0.5cm$ to provide the same cross-sectional area as does the wire radius for the MoM and the one cell FDTD method. On the other hand, the problem space for the small radius approximation (contour integral method) is $31 \times 31 \times 81$ cells, with the cell dimensions $\Delta x = \Delta y = \Delta z = 1.0cm$, and a wire radius of $0.281cm$. In both cases the wire is positioned at the center of the computational space.

For the FDTD calculation the dipole is center fed with a Gaussian pulse of $1.0V$ amplitude, so that the electric field in the gap of the antenna is specified as

$$E_z^n(i,j,k) = -V(n\Delta t)/\Delta z \tag{4.27}$$

where $V(t)$ is a Gaussian voltage source of the form

$$V(t) = \exp -(t - t_o)^2/\tau^2 \tag{4.28}$$

with $t_o = 32\Delta t$ and $\tau = t_o/4$, and the pulse truncated for $t < 0$ and $t > 2t_o$. The time step was set to the Courant limit of $11.11ps$ for the one cell approximation and $11.93ps$ for the contour integral case.

The current flowing through the center of the dipole can be sampled by taking the discrete approximation of the line integral of the H_x and H_y components encircling the electric field, so that I_{in} is obtained from

$$\begin{aligned} I_{in}(n\Delta t) = &\left[H_x^{n+1/2}(i,j-1,k) - H_x^{n+1/2}(i,j,k)\right]\Delta x \\ &+ \left[H_y^{n+1/2}(i,j,k) - H_y^{n+1/2}(i-1,j,k)\right]\Delta y \end{aligned} \tag{4.29}$$

with the spatial indices (i,j,k) correspond to the location of the $E_z(i,j,k)$ electric field in the feed gap. During the progress of the FDTD calculations this current is saved for each time step. The FDTD calculations are continued until all transients are dissipated, in this case 8000 time step, so that the Fourier transform yields the steady-state frequency domain response of the antenna. At the termination of the FDTD computations the input current and voltage are Fourier transformed into frequency domain using the discrete Fourier transform, and the input impedance calculated as,

$$V(w) = Z(w)I(w) \tag{4.30}$$

For comparison, MoM results were obtained using the Numerical Electromagnetic Code (NEC). The wire length was divided into 57 segments, which corresponds to a segment length of $1.0cm$, this is the same as Δz in the FDTD calculation.

The time domain input current of the dipole, obtained using the one cell and contour integral approximations for the FDTD calculation are shown in Fig. 4.2 and Fig. 4.3, respectively. Fig. 4.4 and Fig. 4.5 show the corresponding Fourier transforms of the two currents, in magnitude and phase, compared to the results obtained using the MoM. One can easily observe the effect of the wire approximation in the FDTD calculations on the accuracy of the input current. Similar observation can be obtained by examining the input impedance shown in Fig. 4.6 and Fig. 4.7, for the one cell and contour integral approximations, respectively.

The current behavior is also observed at a position of 15 cell from the lower end of the dipole antenna. The time domain response along with the corresponding Fourier transformed responses for the one cell and the contour integral approximation are recorded in Fig. 4.8-Fig. 4.11.

The next numerical experiment involves loading cell number 15 from the lower end of the dipole with three lumped circuit elements. The voltage response across the lumped element can be obtained through relation (4.14), such as

$$V_z(n\Delta t) = E_z^n(i,j,k) \cdot \Delta z \tag{4.31}$$

where E_z is the z-directed electric field at the load position. The current flowing through the specified load cell can be obtained using Eq. (4.29). Fourier transforming the two quantities into frequency domain and using Eq. (4.30), the lumped impedance in frequency domain will be obtained.

The first loading element considered is a 50Ω resistor. The implementation of this load into the FDTD equations can be accomplished using either the physical resistor method Eq. (4.10) with specified conductivity of $\sigma = 2S/m$, or using the numerical resistor method Eq. (4.20). The time domain current and voltage response are shown in Fig. 4.12–Fig. 4.13 respectively. The calculated load impedance is compared in Fig. 4.14 using (4.10), (4.20) and the ideal value of the resistor. It is observed that over the span of DC to $3GHz$, the maximum deviation is 0.65Ω for the two methods, respectively, from the ideal value.

The second numerical experiment involves loading the same cell of the dipole by a capacitor of $C = 6pF$. Again this is done using physical and numerical implementation, Eq. (4.10) and Eq. (4.21), respectively. The current and voltage responses across the capacitor are shown in Fig. 4.15 and Fig. 4.16, respectively. The load impedance obtained using the two methods is compared against the ideal capacitive reactance obtained using circuit theory. From circuit theory the capacitive reactance in the frequency domain can be obtained simply from

$$Z_c(\omega) = \frac{-j}{\omega C} \tag{4.32}$$

where ω is the radian frequency, $\omega = 2\pi f$, C is the capacitance in Farad, and $j = \sqrt{-1}$. The comparison is given in Fig. 4.17 where excellent agreement is observed.

Finally an RLC parallel circuit is implemented using FDTD. The inductor value is chosen as $L = 4.2nH$ with R and C having the same values as used in the previous simulations, this is to provide a resonant circuit at $1GHz$. The FDTD implementation is done through the use of the numerical implementation, with the

E_z updating equation for the RLC parallel circuit being,

$$\begin{aligned} E_z^{n+1}(i,j,k) &= \frac{1-\frac{\Delta t\Delta z}{2R\varepsilon_o\Delta x\Delta y}+\frac{C\Delta z}{\varepsilon_o\Delta x\Delta y}}{1+\frac{\Delta t\Delta z}{2R\varepsilon_o\Delta x\Delta y}+\frac{C\Delta z}{\varepsilon_o\Delta x\Delta y}}E_z^n(i,j,k) \\ &+\frac{\Delta t/\varepsilon_o}{1+\frac{\Delta t\Delta z}{2R\varepsilon_o\Delta x\Delta y}+\frac{C\Delta z}{\varepsilon_o\Delta x\Delta y}}\left(\nabla\times H^{n+1/2}\right)_z \\ &-\frac{\Delta z(\Delta t)^2}{1+\frac{\Delta t\Delta z}{2R\varepsilon_o\Delta x\Delta y}+\frac{C\Delta z}{\varepsilon_o\Delta x\Delta y}}\sum_{m=1}^{n}E_z^m \end{aligned} \tag{4.33}$$

The transient current and voltage across the lumped circuit are provided in Fig. 4.18 and Fig. 4.19, respectively. The real and imaginary values of the lumped impedance Z_{RLC} obtained using FDTD is compared to the circuit theory value in Fig. 4.20. The agreement is very good and the circuit behaved as expected at resonance. Fig. 4.21 shows a comparison of the absolute value of the lumped circuit impedance $|Z_{RLC}|$ calculated using FDTD and circuit theory. The variation of phase with frequency of the three modeled cases, R, C and parallel RLC, are reported in Fig. 4.22.

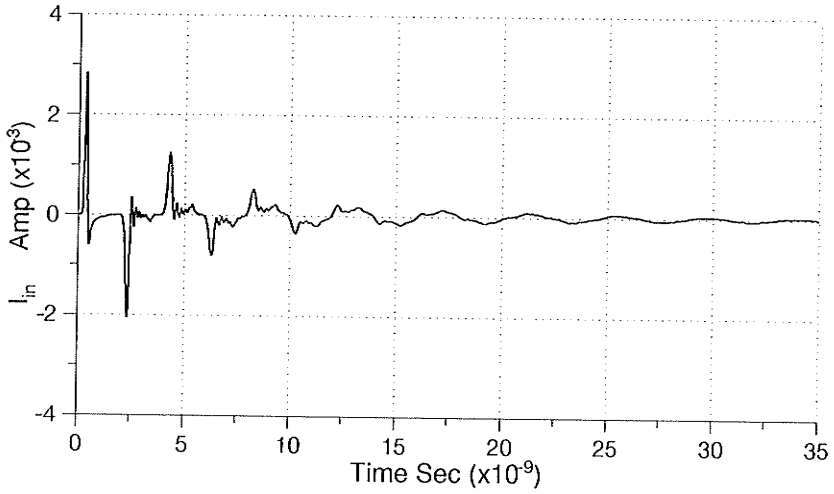

Figure 4.2: Input current for the wire dipole with one cell approximation radius.

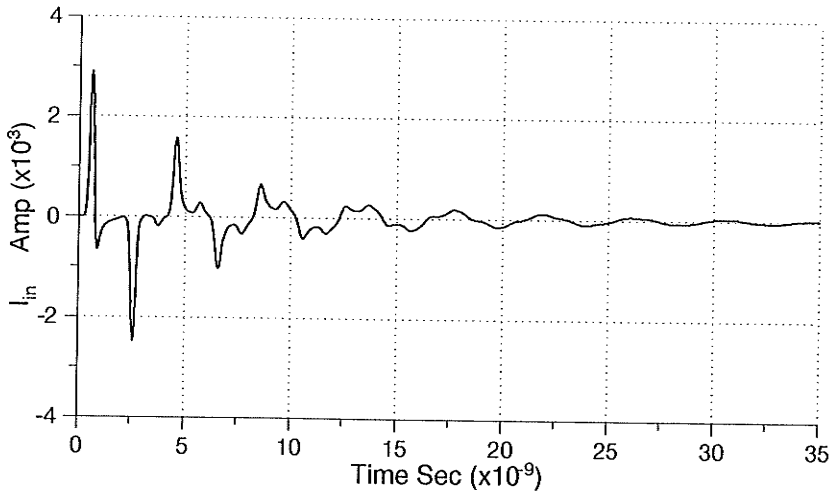

Figure 4.3: Input current for the wire dipole with contour integral approximation.

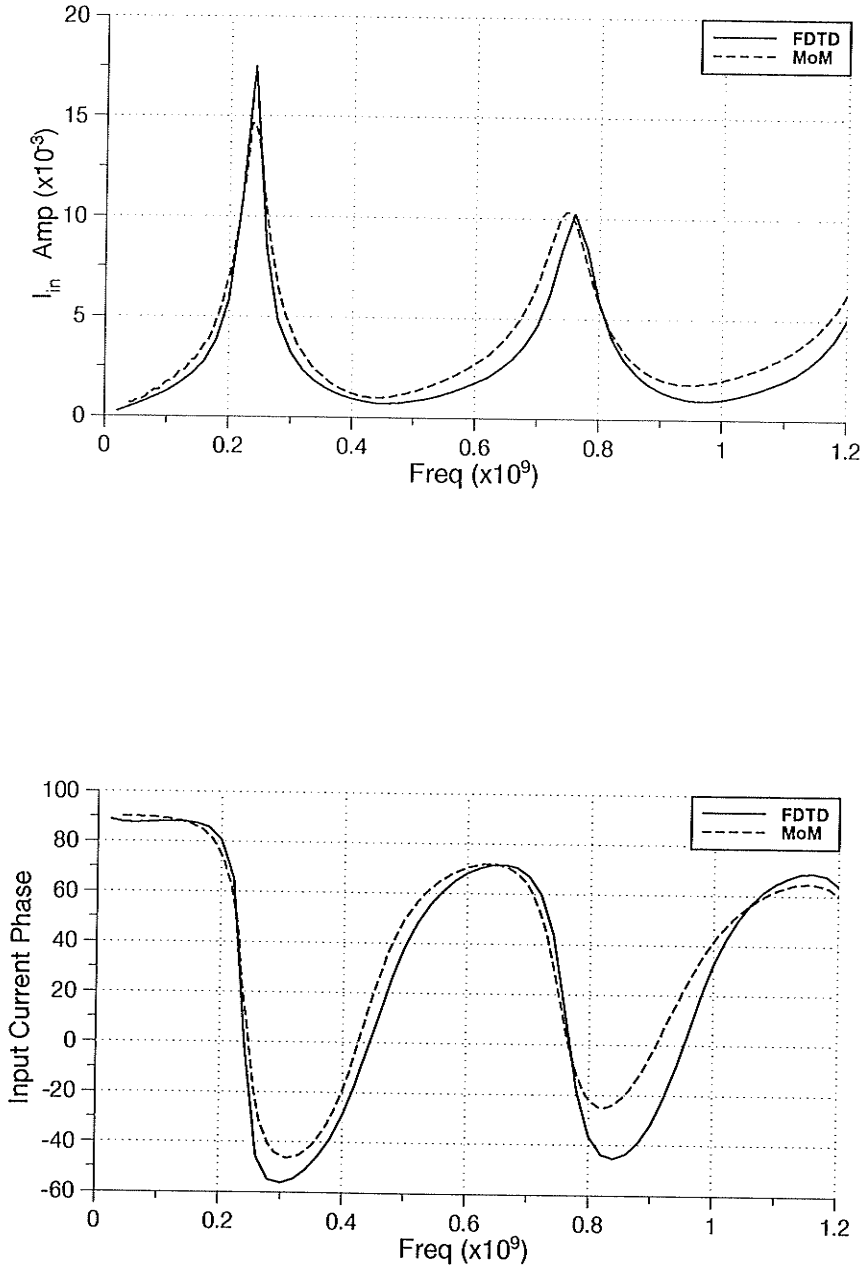

Figure 4.4: Magnitude and phase of the input current for the wire dipole with one cell approximation.

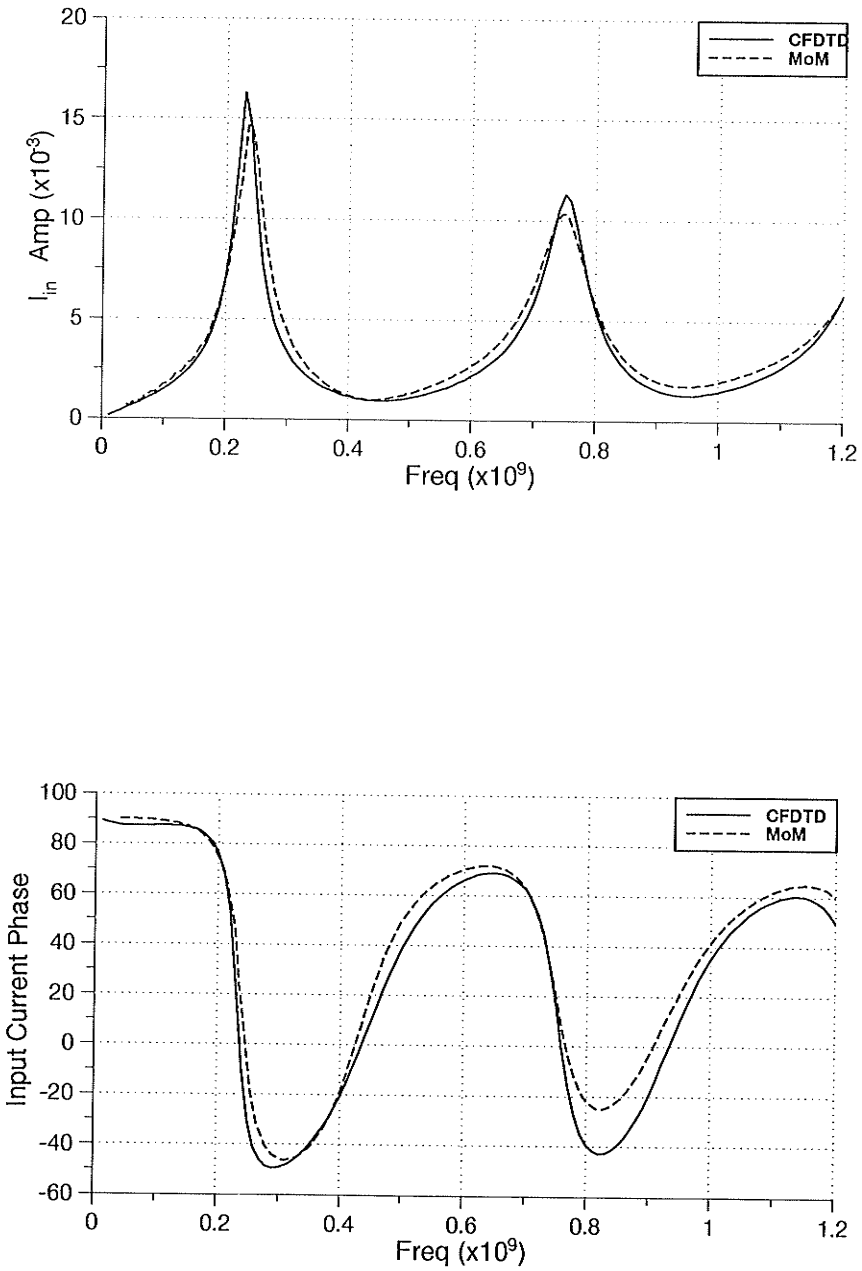

Figure 4.5: Magnitude and phase of the input current for the wire dipole with contour integral approximation.

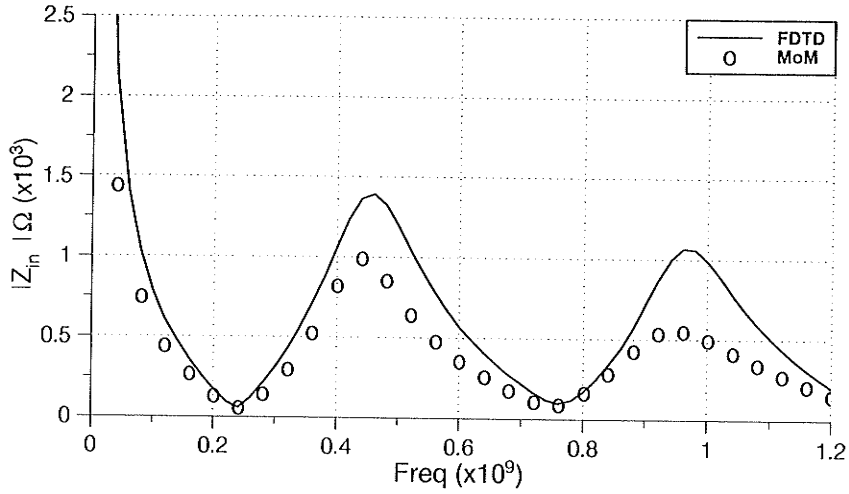

Figure 4.6: Magnitude of the input impedance for the wire dipole with one cell approximation.

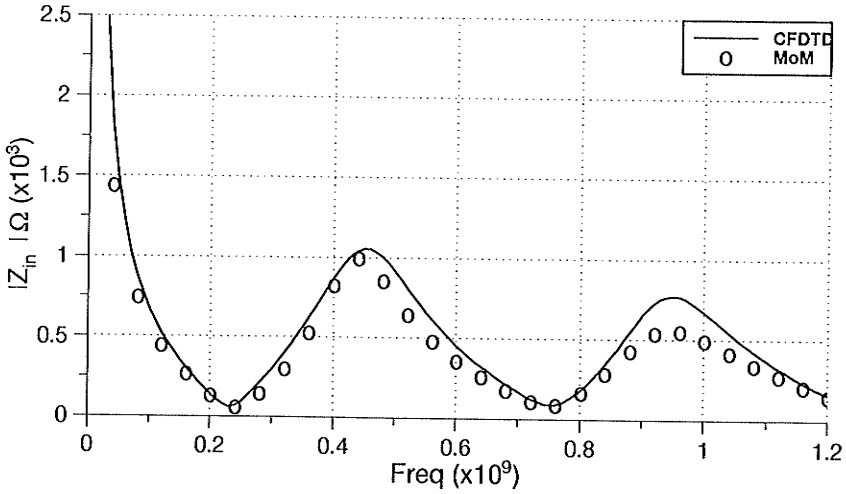

Figure 4.7: Magnitude of the input impedance for the wire dipole with contour integral approximation.

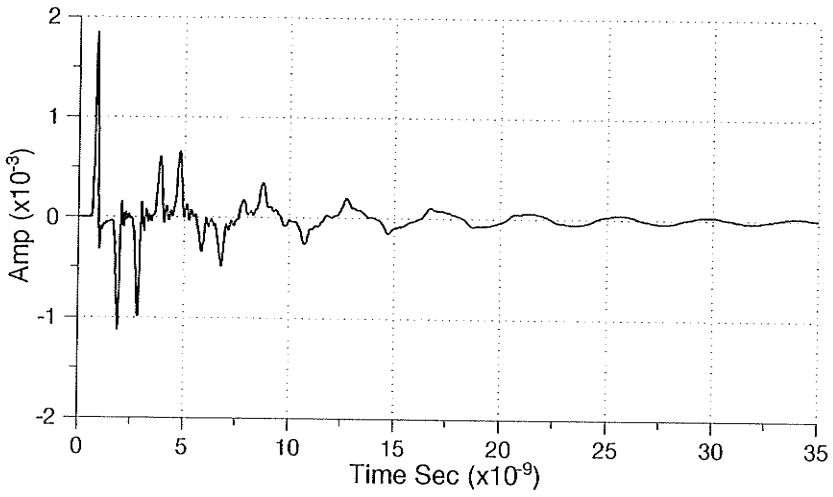

Figure 4.8: Current response at location (0,0,15), 15 cells form the lower end of the wire dipole with one cell approximation radius.

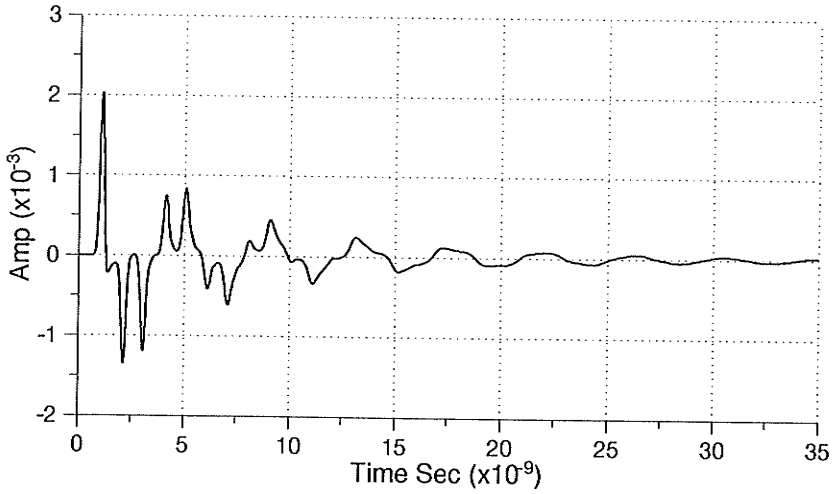

Figure 4.9: Current response at location (0,0,15), 15 cells form the lower end of the wire dipole with contour integral.

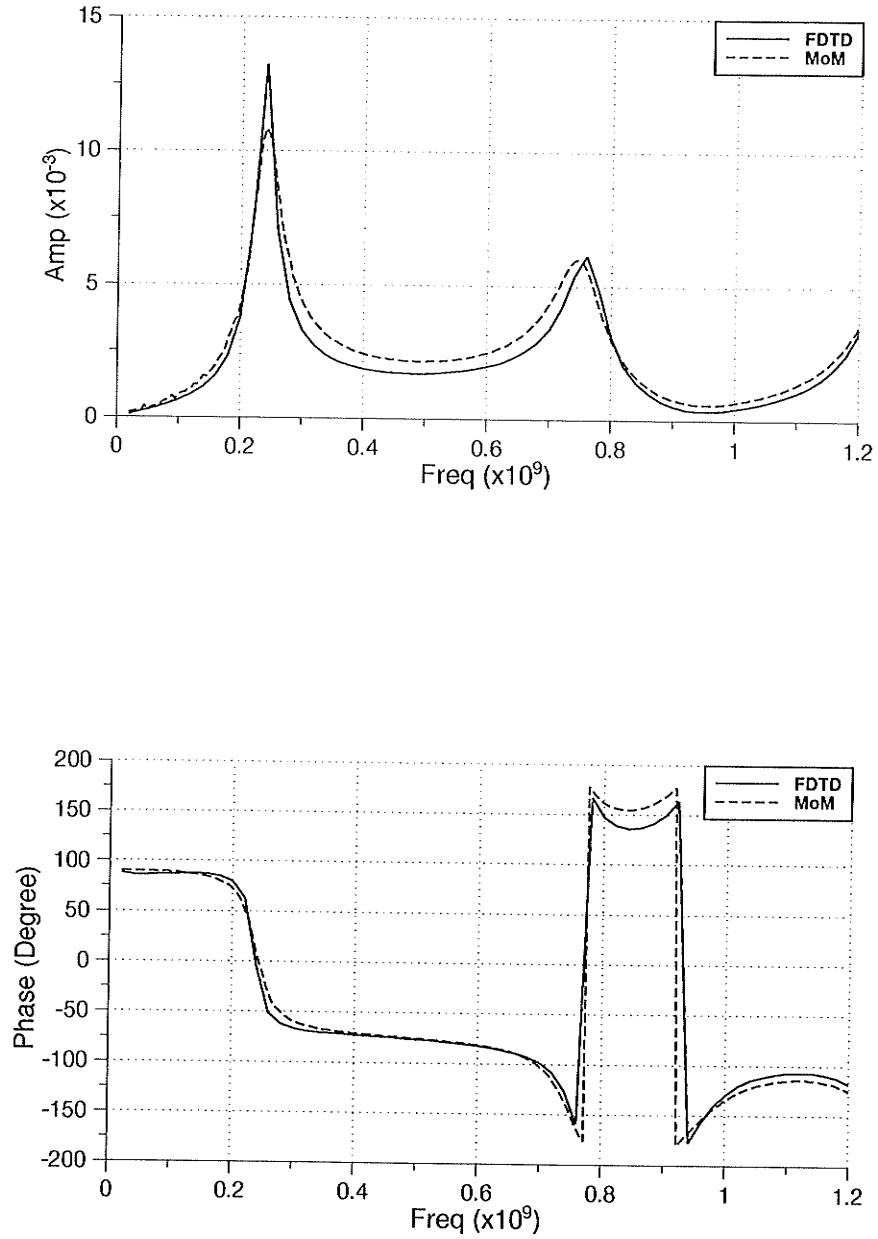

Figure 4.10: Magnitude and phase of the current at cell 15 of the wire dipole with one cell approximation.

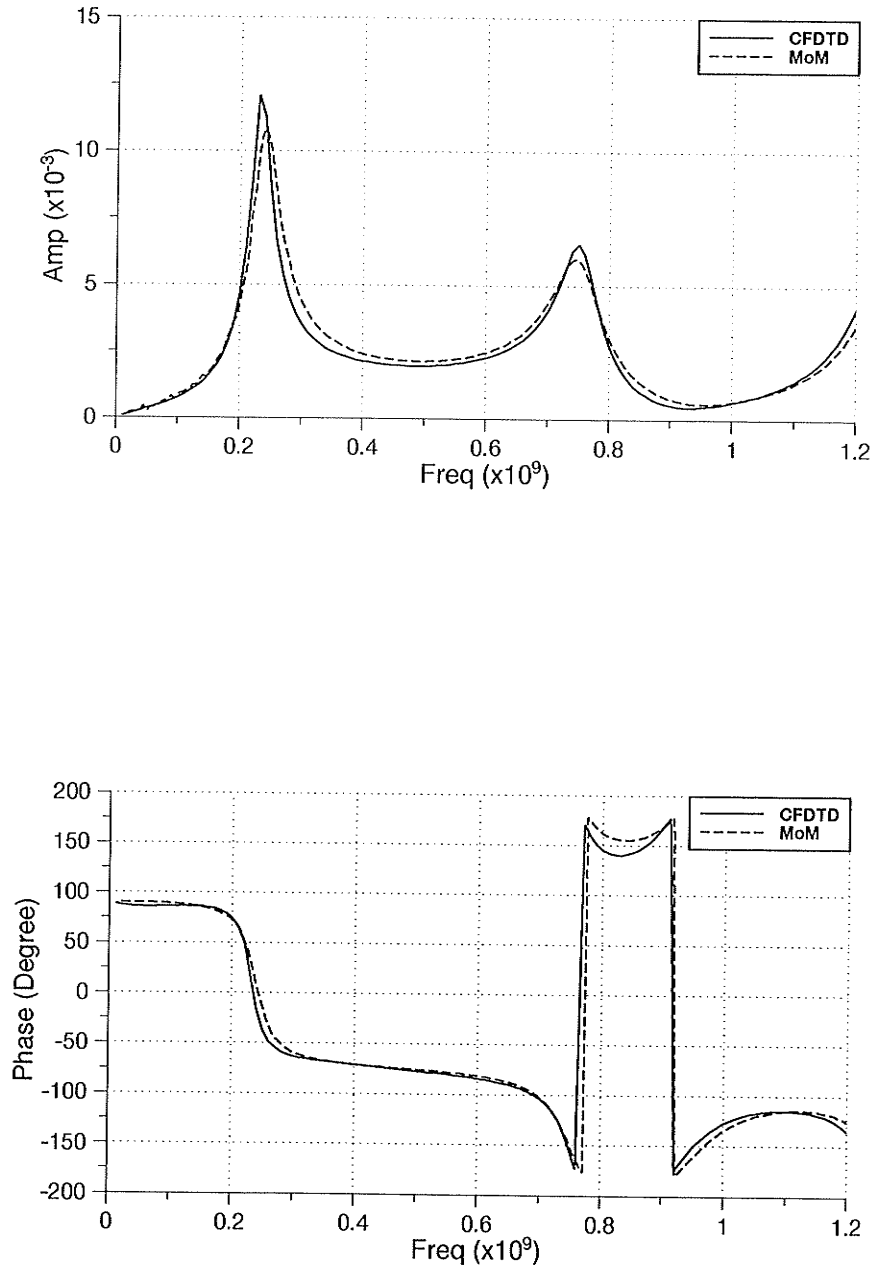

Figure 4.11: Magnitude and phase of the current at cell 15 of the wire dipole with contour integral approximation.

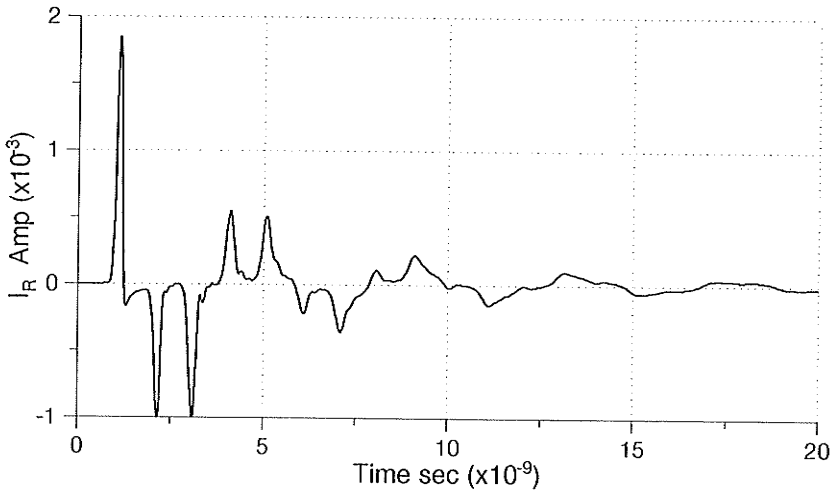

Figure 4.12: Transient current through the 50Ω resistance at cell location $(i, j, 15)$.

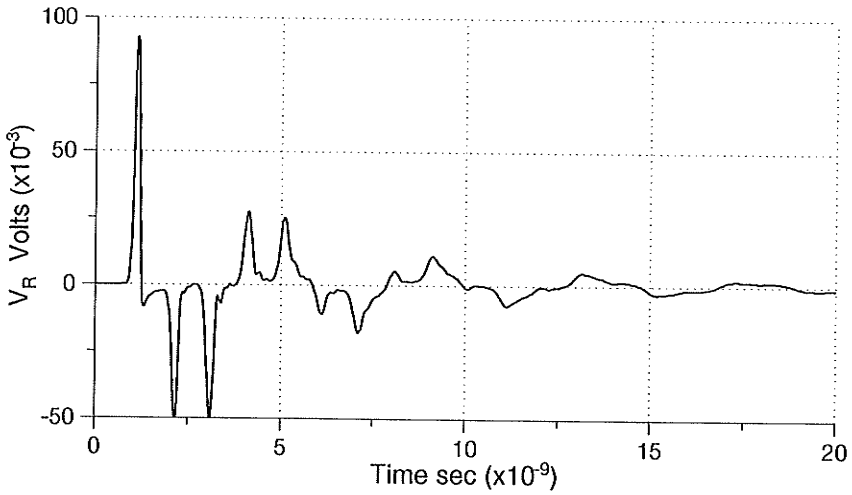

Figure 4.13: Transient voltage across the 50Ω resistance at cell location $(i, j, 15)$.

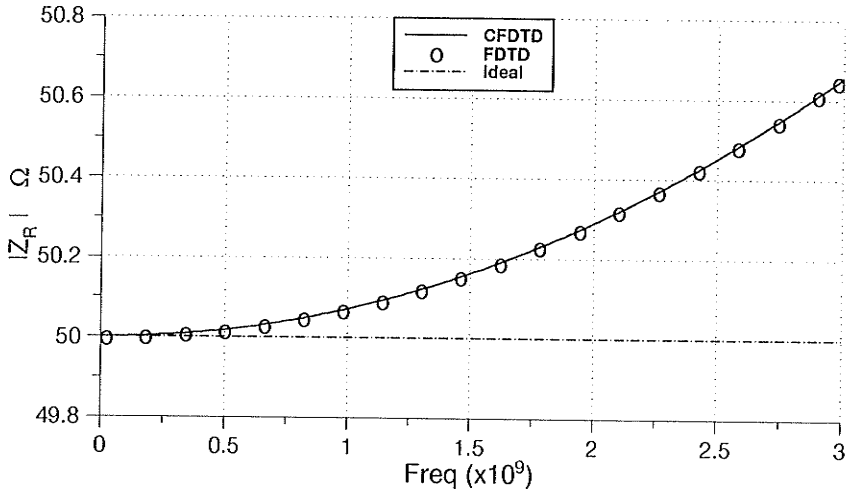

Figure 4.14: Comparison of the lumped resistance value calculated using FDTD, CFDTD and the ideal value $R = 50\Omega$.

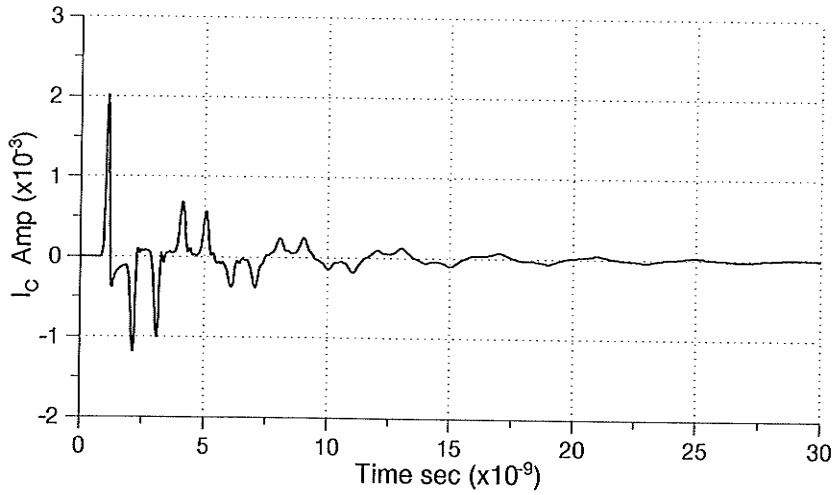

Figure 4.15: Transient current through the capacitor at cell location $(i, j, 15)$.

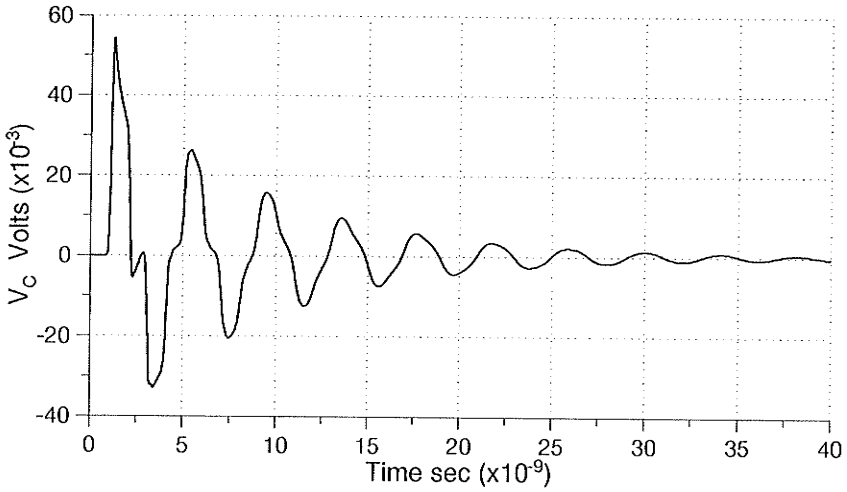

Figure 4.16: Transient voltage across the capacitor at cell location $(i, j, 15)$.

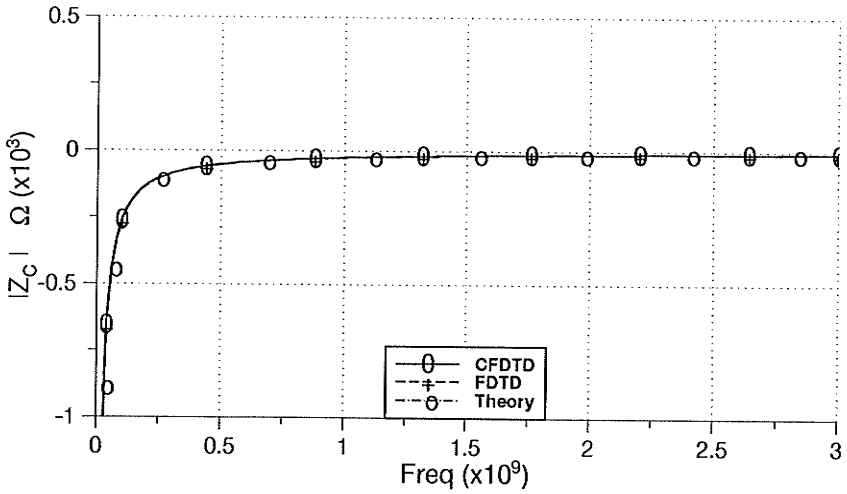

Figure 4.17: Comparison of the lumped capacitive reactance value calculated using FDTD, CFDTD and circuit theory.

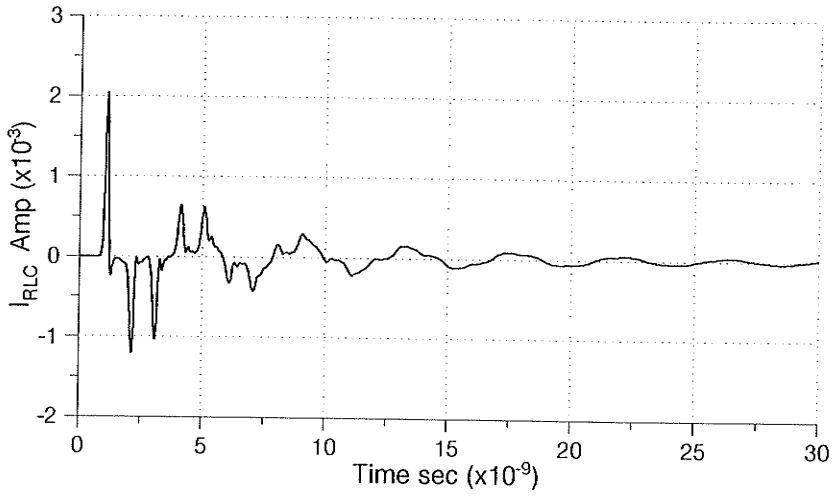

Figure 4.18: Transient current through the parallel RLC circuit at location $(i, j, 15)$.

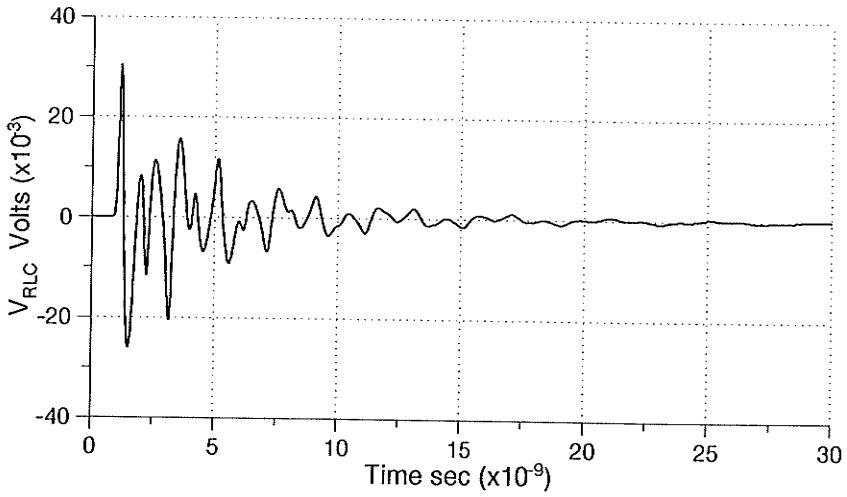

Figure 4.19: Transient voltage across the parallel RLC circuit at location $(i, j, 15)$.

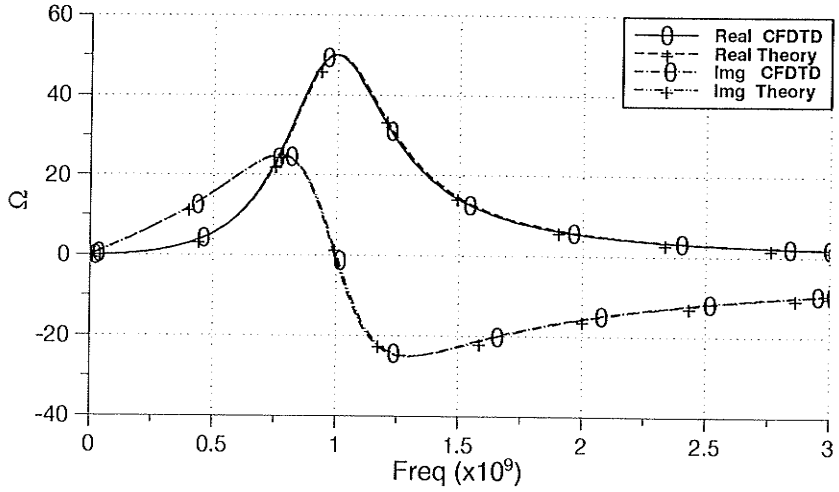

Figure 4.20: Comparison of the real and imaginary lumped impedance calculated using CFDTD and circuit theory.

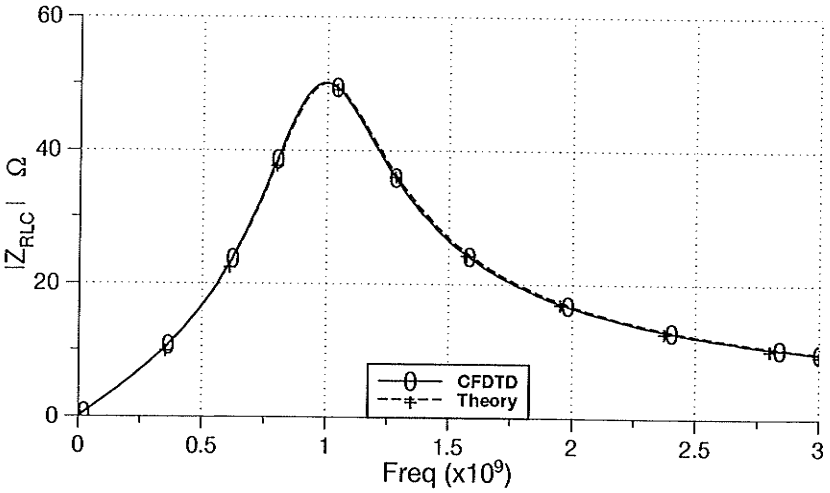

Figure 4.21: Comparison of the lumped impedance $|Z_{LRC}|$ calculated using CFDTD and circuit theory.

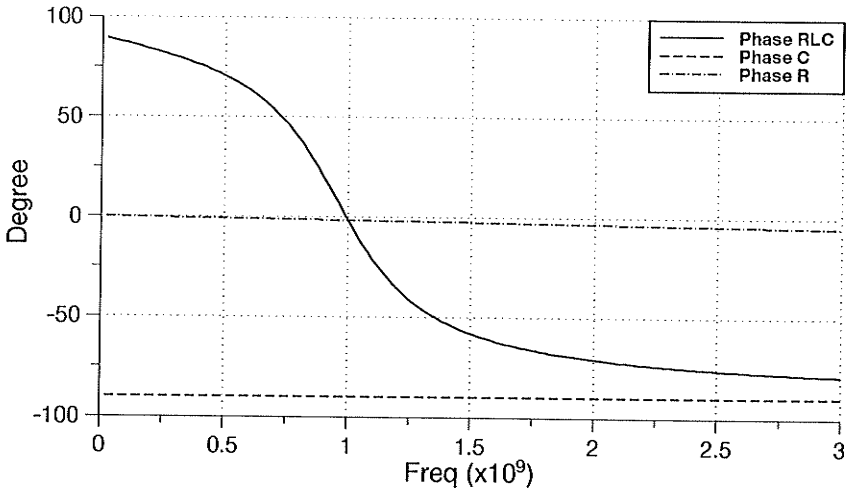

Figure 4.22: Phase variation of R, C, and parallel RLC with frequency.

CHAPTER 5

Application to 3-D Scattering and Radiation

5.1 Introduction

The FDTD calculations only produce information of the electromagnetic fields within or adjacent to the scattering or radiating object, such that the fields are contained within the FDTD computation space. However, FDTD can also be applied to analyze scattering from radar targets or radiation from antennas, with the desired results being the far zone scattered or radiated fields that lie outside the FDTD space. This can be accomplished through use of the equivalence principle, where the near field information is used to obtain the equivalent tangential electric and magnetic currents. These currents are then transformed into the far field region to obtain the scattered or the radiated fields. The application of this technique in the FDTD algorithm is discussed in detail in the following section. Later in this chapter the far field data are obtained for some applications involving three dimensional scattering and antenna radiation.

5.2 Near Field to Far Field Transformation

Usually the solution to electromagnetic scattering/radiation by arbitrary conducting bodies involves to the determination of the induced surface electric-current distribution on the body. Then, these currents are used to calculate near or far field data. Such a procedure is applicable when the structure involved is simple and has a smooth surface. However, when the surface becomes complex in shape or loaded with dielectric materials, this requires a unique formulation for each object. A useful alternative would be to obtain the scattered/radiated field information from off-surface near-field data, rather than the surface current data [65]. The near-field

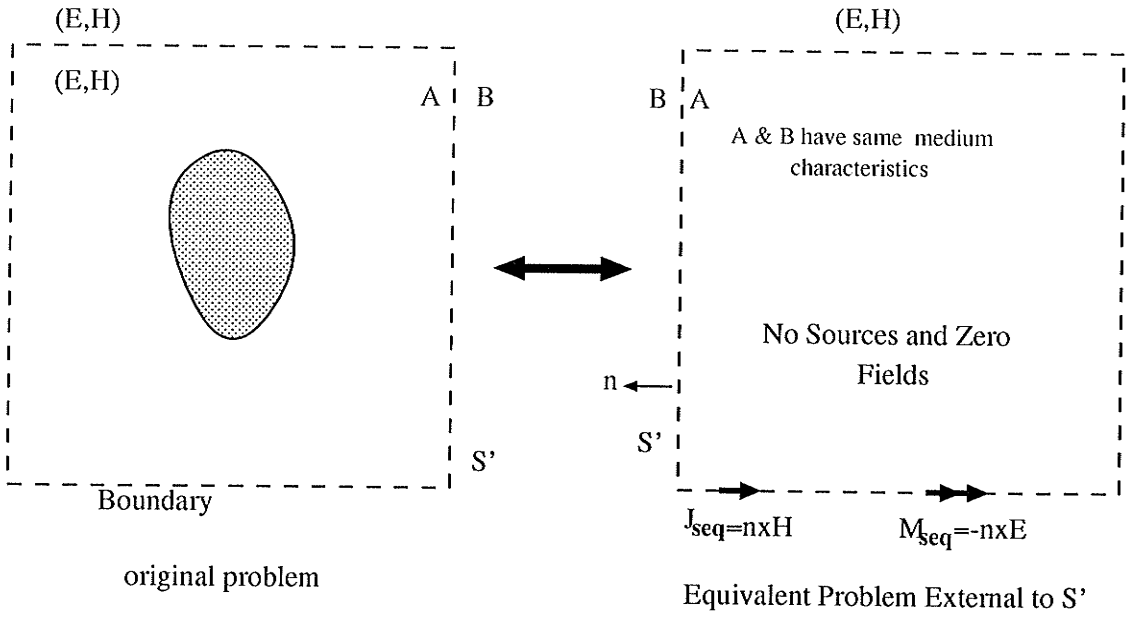

Figure 5.1: Near field to far field transformation surface.

information required for such transformation is a natural product of FDTD computations. Assume an arbitrary closed virtual boundary surface S', which separates the exterior infinite region B and the interior region A containing the object. The

closed surface S' is chosen rectangular in shape to conform with the distinct planes of the FDTD lattice Fig. 5.1. If $\hat{n}$ is the outward unit normal vector at the surface S', then according to [65] an equivalent problem external to S' is set up by defining the equivalent tangential electric currents $\mathbf{J_{seq}}$ and equivalent tangential magnetic currents $\mathbf{M_{seq}}$ on S' such that,

$$\mathbf{J_{seq}} = \hat{\mathbf{n}} \times \mathbf{H}(\mathbf{r}) \tag{5.1}$$

$$\mathbf{M_{seq}} = -\hat{\mathbf{n}} \times \mathbf{E}(\mathbf{r}) \tag{5.2}$$

Transforming the equivalent sources of (5.1) and (5.2) over the free space Green's function as discussed in [66] yields the far-field. With $(\varepsilon_o, \mu_o, \sigma_o)$ being region B medium characteristics, the far-field expressions for θ and ϕ polarization will take the form,

$$E_\theta = (-jk_o\eta_o)[A_\theta + F_\phi/\eta_o] \tag{5.3}$$

$$E_\phi = (-jk_o\eta_o)[A_\phi - F_\theta/\eta_o] \tag{5.4}$$

where

$$\begin{aligned} A_\theta &= A_x\cos\theta\cos\phi + A_y\cos\theta\sin\phi - A_z\sin\theta \\ F_\theta &= F_x\cos\theta\cos\phi + F_y\cos\theta\sin\phi - F_z\sin\theta \\ A_\phi &= -A_x\sin\phi + A_y\cos\phi \\ F_\phi &= -F_x\sin\phi + F_y\cos\phi \end{aligned} \tag{5.5}$$

where $\mathbf{A}$ and $\mathbf{F}$ are the magnetic and electric vector potential in the far field region, respectively, and they are given by [66],

$$\begin{bmatrix} \mathbf{A} \\ \mathbf{F} \end{bmatrix} = \left(\frac{e^{(-jk_o r)}}{4\pi r}\right) \int\int_{s'} \begin{bmatrix} \mathbf{J}_{s_{eq}} \\ \mathbf{M}_{s_{eq}} \end{bmatrix} e^{(jk_o r' \cos\xi)} ds' \tag{5.6}$$

$$r' \cos\xi = (x' \cos\phi + y' \sin\phi) \sin\theta + z' \cos\theta \tag{5.7}$$

here, (x', y', z') is the location of the equivalent source in Cartesian coordinates.

The procedure discussed above is frequently called the frequency domain far zone transformation, this is because the data used in this transformation is frequency domain data. Frequency domain data can be obtained from time domain data in one of two ways. The first way requires the FDTD space to be illuminated by a continuous sinusoidal wave (CW). This method requires an individual FDTD run for every frequency of interest. Frequency domain data can be obtained when the wave form reaches a steady-state. This can be done by observing the peak positive- and negative-going values of fields over a complete cycle of the wave form. A second approach is to use FDTD with a time-limited pulsed excitation (pulsed FDTD). This procedure is used to obtain far field results at multiple frequencies. For each frequency of interest the discrete Fourier transform (DFT) of the time domain tangential fields (surface currents) on the closed surface surrounding the FDTD geometry is updated at each time step. This provides the complex frequency domain currents for any number of frequencies.

Determining the tangential fields and surface currents can be illustrated by considering the contribution from a single FDTD cell. This cell lies on the surface of S'. The complete structure far field data can be obtained by summing similar contributions from all cells on the surface. Due to the nature of the Yee cell, the

field quantities are not specified at any particular surface of the cell [53]. Therefore, nearby cells are used to determine the tangential field values at the center of the cell faces. As an example consider the electric field component E_x^n tangential to the transformation surface S' and at the center of a particular (i, j, k) Yee cell face. E_x^n must be found by appropriate spatial averaging of E_x^n value from cell (i, j, k) and from adjacent cells. Assume that part of the integration surface under consideration has an outward unit normal vector $\hat{n} = \hat{y}$. Then at the center of the cell face, $E_x^n = (E_x^n(i, j+1, k) + E_x^n(i, j+1, k+1))/2$ (the magnetic field components at this point will require averaging four terms)[53]. Using Eq. (5.2) this electric field component will produce the magnetic surface current,

$$M_s = -\hat{y} \times E_x^n \hat{z} \tag{5.8}$$

therefore, E_x^n on this surface contributes only to F_z, the surface area of integration is $\Delta x \cdot \Delta z$ and the value of E_x^n is assumed constant over this surface. In order to keep track of the relative time delay for each cell face in the integration surface, a spatial reference at the center of cell (i_c, j_c, k_c) will be located, ex., the center cell of the Cartesian computation space would be an appropriate reference point. The vector from the reference cell to the center of the Yee cell face in the integration surface is

$$\overline{r}' = (i - i_c)\Delta x\hat{x} + (j + 1/2 - j_c)\Delta y\hat{y} + (k - k_c)\Delta k\hat{k} \tag{5.9}$$

The value of $1/2$ is added because the integration surface of the i, j, k cell face under consideration is offset by $1/2$ cell in the y direction away from the cell center. Similarly a $\pm 1/2$ cell contribution must be considered for all the cell faces on the S' integration surface.

5.3 Application to Scattering Problems

Of the many applications of FDTD in computational electromagnetics, the first FDTD successful application reported in the literature was the problem of scattering and interaction with two-dimensional (2-D) objects [57]. The algorithm was then extended and modified to include three-dimensional (3-D) objects.

As stated in chapter 2, FDTD is a direct solution of Maxwell's time dependent curl equations. By time stepping, and repeatedly implementing the finite difference algorithm of the curl equations at each cell of the corresponding space grid, the incident wave is tracked as it first propagates to the structure and then interacts with it via surface current excitation, diffusion, penetration, and diffraction. For scattering applications, the computational space is divided into a total field region, the region containing and surrounding the object, and scattered field region, the region outside the total field region and truncated by the outer radiation boundaries.

In this section two types of 3-D objects will be studied. First scattering by a conducting cube is considered. The cube is embedded in a 3-D free space grid and excited by a sinusoidal z-polarized plane wave with $\theta^i = 90^o$ and $\phi^i = 0^o$, accordingly the plane wave will have the field components E_z^i and H_y^i and propagates in the $-x$ direction. The cube is assumed to have an electrical size $k_o a = 1$, where a is the half-width of the face of the cube. The computational space is taken as $50 \times 50 \times 50$ cells and each face of the cube spans 20×20 cells. The modeling of the conducting cube is done by forcing the tangential components of the electric field on the surface of the cube to zero. A near-field to far-field transformation is carried out in a procedure following the discussion in Sec. 5.2. Figure 5.2 shows a comparative

normalized radar cross-section obtained by FDTD and method of moments based on the Numerical Electromagnetic Code (NEC).

The second type considered is the scattering by both a lossless and lossy dielectric sphere. The modeling of the sphere is done by approximating the sphere by a stepped surface. The sphere is situated in free space and excited by an x-polarized plane wave with $\theta^i = 180^o$ and $\phi^i = 0^o$. Hence, the plane wave will have the field components E_x^i and H_y^i and propagates in the z direction. The sphere is assumed to have $\varepsilon_r = 3.0$ for the lossless case and $\varepsilon_r = 3.0$ and $\sigma = 0.04$ for the lossy one. An electrical size $k_o a = \pi$ is assumed, where a is the radius of the sphere. Fig. 5.3 shows a comparison of the radar cross-section of the two case with the lossless case exact solution. Fig. 5.4 shows the back scattering cross-section of a conducting sphere with respect to ka in the vicinity of a spherical cavity resonance. The sphere is excited by a plane wave with $\theta^i = 90^o$ and $\phi^i = 0^o$ and $a = 0.437\lambda$. It can be observed that the results are smooth and did not encounter any singular behavior at the resonance frequency of the conducting sphere, to the contrast of an integral equation solution.

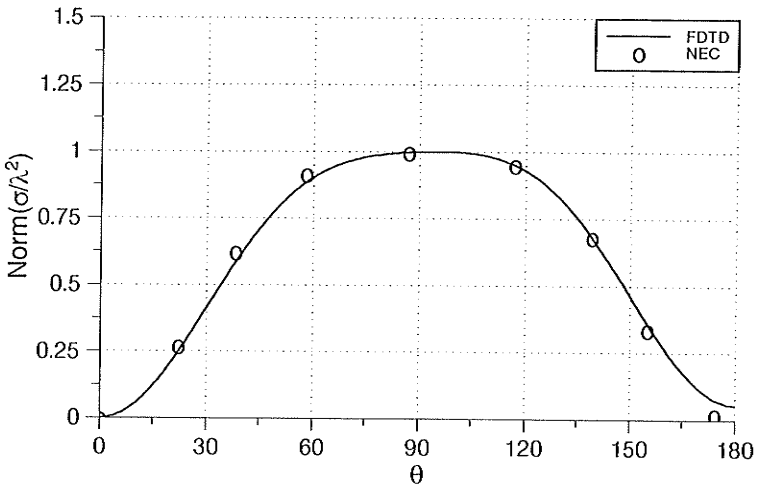

Figure 5.2: Normalized radar cross-section of the conducting cube with $k_o a = 1$ and $\phi = 0^o$.

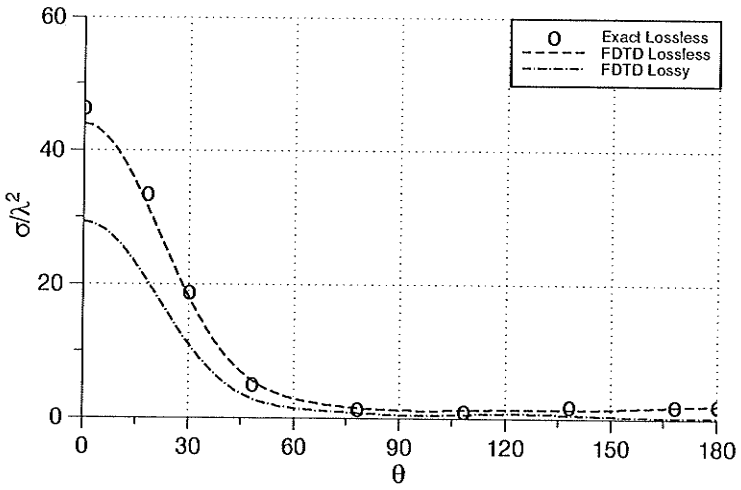

Figure 5.3: Comparison of the radar cross-section of the lossless and lossy sphere, $k_o a = \pi$, $\varepsilon_r = 3.0$, $\sigma = 0.04$ and at $\phi = 0^o$.

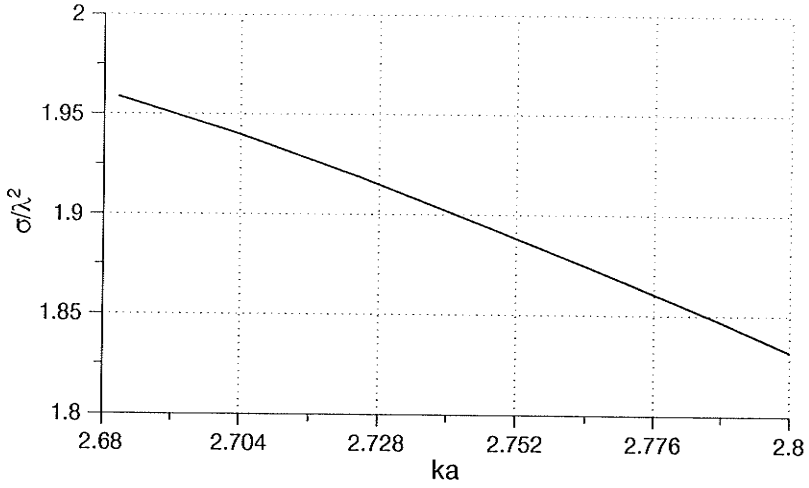

Figure 5.4: Back scattering behavior of a conducting sphere, at $\phi = 0^o$, $\theta = 90^o$ and $a = 0.437\lambda$.

5.4 Application to Antenna Radiation

In this section the FDTD technique is implemented to obtain the radiation pattern of three antenna configurations. First, a wire antenna mounted on a rectangular conducting box is considered, the wire antenna is assumed a quarter-wavelength monopole connected to the top of the rectangular box. The geometry is an approximation to a small hand-held radio unit with attached antenna. The effect of the box size on the radiation pattern is studied using two different size boxes. Radiation pattern results obtained using the developed FDTD algorithm are compared with the same results reported in [53] using method of moments.

The second configuration considered is a bent-slot antenna flush mounted on a rectangular conducting box modeled using FDTD. Two antenna configurations are modeled based on slot position. Kuboyama *et al.* [67] studied six types of such antenna. In their calculations, the equipment box was assumed rectangular, the surface of the box and the slot were modeled by wire grids. Method of moments was then applied to find both the electric and magnetic currents distributions on the slot. The two models examined in this paper agree very well with the results obtained by Kuboyama *et al.* [67].

The third antenna configuration considered is a quarter-wavelength monopole antenna mounted on an automobile's roof. Nishikawa and Asano [68] have replaced the model of the automobile by a theoretical model and then the geometrical theory of diffraction was applied to obtain the radiation pattern. The same model is used in the FDTD computation and the results obtained agreed with [68].

The feed for the three configurations under study can be modeled using three

different approaches [39]. First, an equivalent frill generator can be used by forcing the four tangential magnetic field components at the position of the feed surrounding the wire to a known function. This produces a current distribution on the surface of the wire. As the unit cell of the grid becomes small, the input current of the feed point can be estimated by evaluating the line integral of the four surrounding magnetic fields (Ampere's law). This will provide an accurate estimate of the input impedance of the antenna. Second, an equivalent delta-gap voltage generator can be used by forcing the normal component of the electric field at the feed point to have a sinusoidal form. In order to accomplish this, a unit cell of the FDTD grid must be reserved for this purpose. Third, an impressed current source can be incorporated into the FDTD equations. The feed will be modeled using an equivalent delta-gap generator.

Since this chapter deals only with the radiation pattern, the second type of feed will be employed in all simulations, such as,

$$E^n(i,j,k) = -V(n\Delta t)/\Delta \tag{5.10}$$

where Δ is the space increment and $V(t)$ is a sinusoidal voltage source given by,

$$V(t) = \sin \omega t \tag{5.11}$$

5.4.1 Monopole Mounted on a Box

The antenna under consideration is shown in Fig. 5.5. Kunz and Luebbers [53] have studied this type of antenna using the FDTD technique. The purpose of reproducing the same results is to show the validity of the computer code developed. Two different size boxes will be considered with the dimensions given in Fig. 5.5.

The antenna is modeled using a space increment $\Delta = \Delta x = \Delta y = \Delta z = 5\,mm$, this corresponds to 40 cells per wavelength $\lambda/40$. The time stepping is chosen as $\Delta t = \Delta/(2c)$.

For the box with $L_z = 130\,mm$ the space was modeled by $72 \times 62 \times 86$ cells, and far fields zone were calculated in one degree increments using the procedure discussed in Sec. 5.2. For $L_z = 200\,mm$ box, the problem space was $72 \times 62 \times 100$ cells. The conducting box of the antenna is modeled by forcing the tangential components of the electric fields on the surface of the box to zero. The monopole antenna is modeled using a wire of finite radius. Again the wire is modeled by forcing the axial electric field on the surface of the wire to zero. In order to incorporate the modeling of the monopole antenna in the finite-difference equations, the contour integral interpretation of Maxwell's integral equations can be applied over a wire subgrid model of the three dimensional wire antenna as discussed in Sec 4.2.

The radiation patterns were desired in the $\phi = 0^o$ $(x - z)$ plane, $\phi = 90^o$ $(y - z)$ plane and $\theta = 90^o$ $(x - y)$ plane. Radiation patterns were calculated for box sizes $L_z = 130\,mm$ and $L_z = 200\,mm$, with the monopole centered on the top of the box. Results obtained are shown in Fig. 5.6–Fig. 5.11. It is clear that the radiation patterns of the antennas is similar to the behavior of a wire antenna. They comply very well with the results obtained with the method of moments calculations.

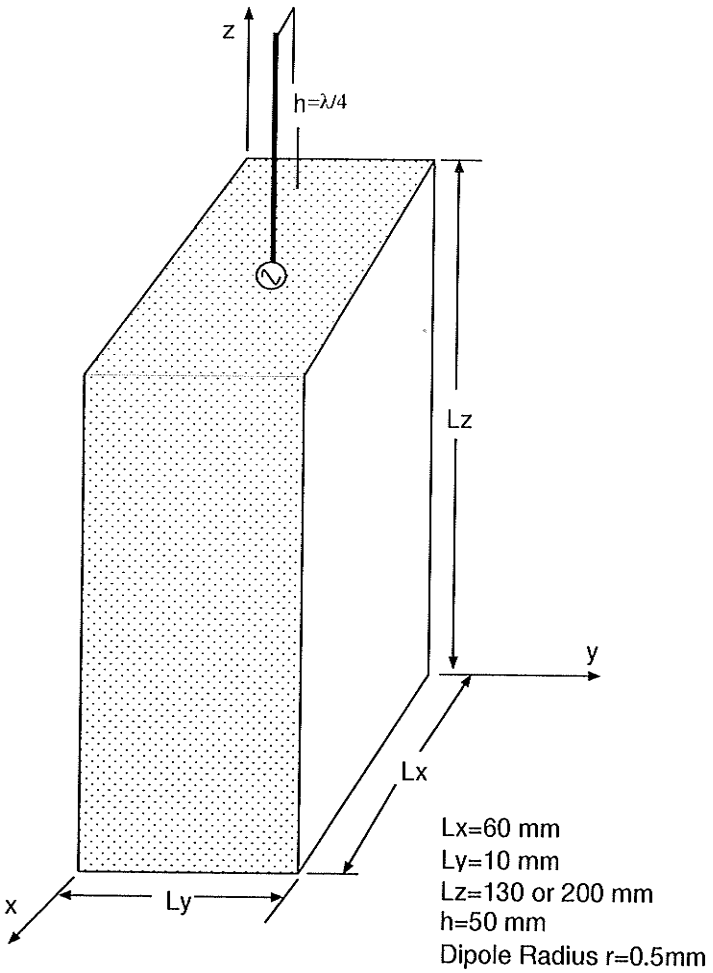

Figure 5.5: Monopole antenna on a rectangular box.

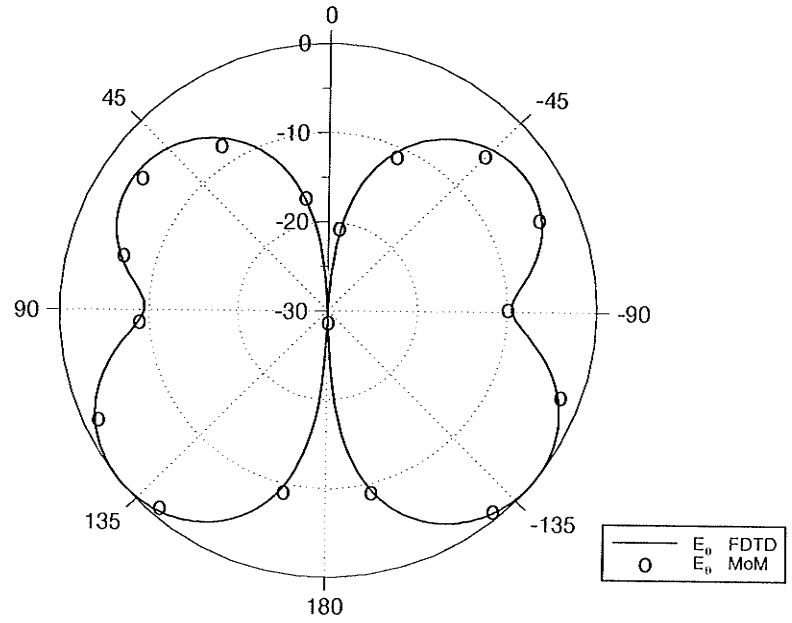

Figure 5.6: Radiation pattern of monopole antenna on a box, x-z plane, $\phi = 0^o$ and $L_z = 130mm$.

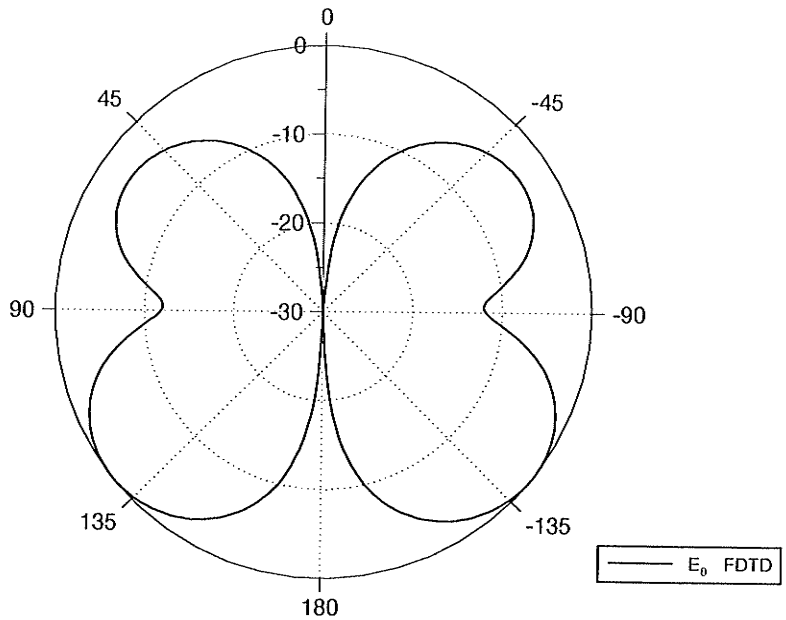

Figure 5.7: Radiation pattern of monopole antenna on a box, y-z plane, $\phi = 90^o$ and $L_z = 130mm$.

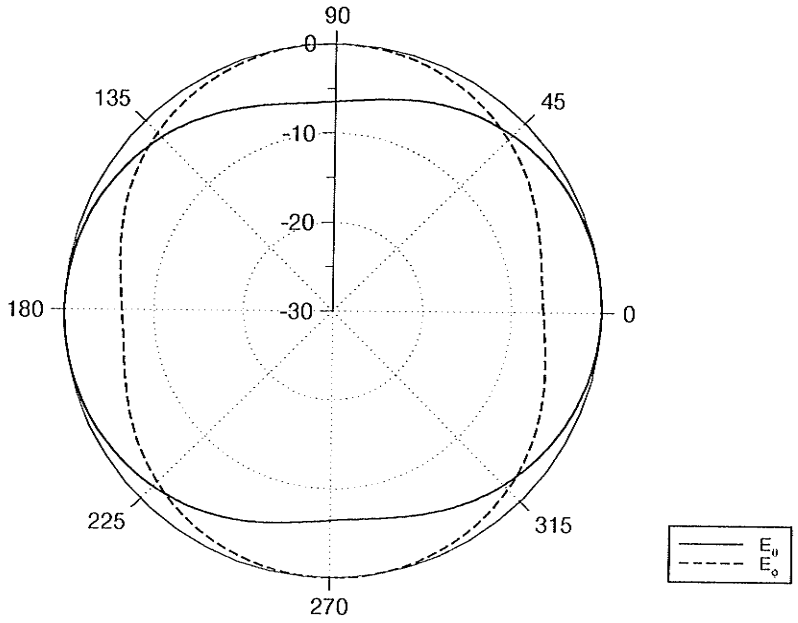

Figure 5.8: Radiation pattern of monopole antenna on a box, $\theta = 90^o$ and $L_z = 130mm$.

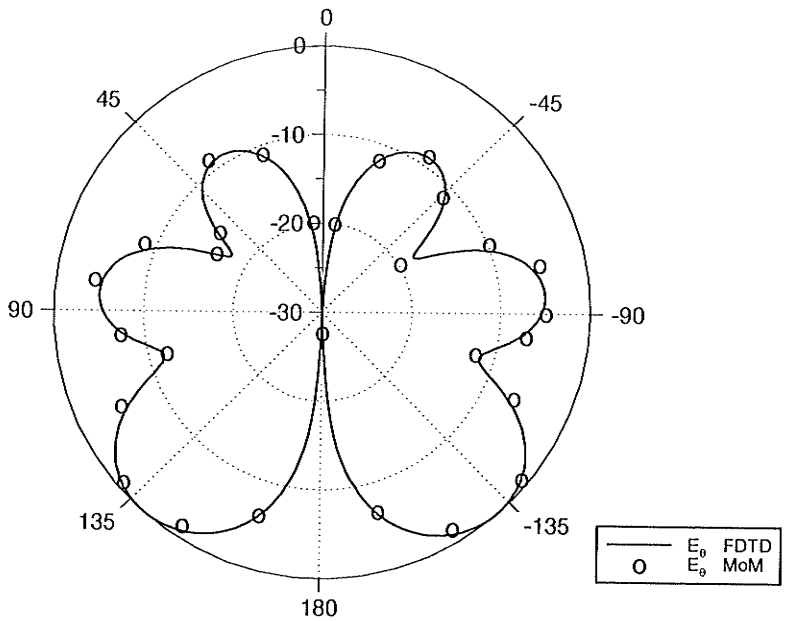

Figure 5.9: Radiation pattern of monopole antenna on a box, x-z plane, $\phi = 0^o$ and $L_z = 200mm$.

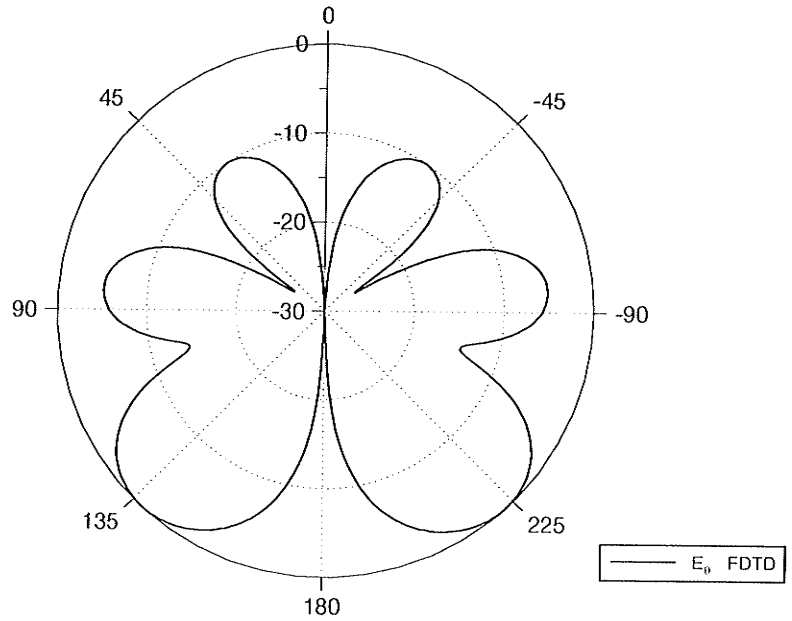

Figure 5.10: Radiation pattern of monopole antenna on a box, $\phi = 90^o$ and $L_z = 200mm$.

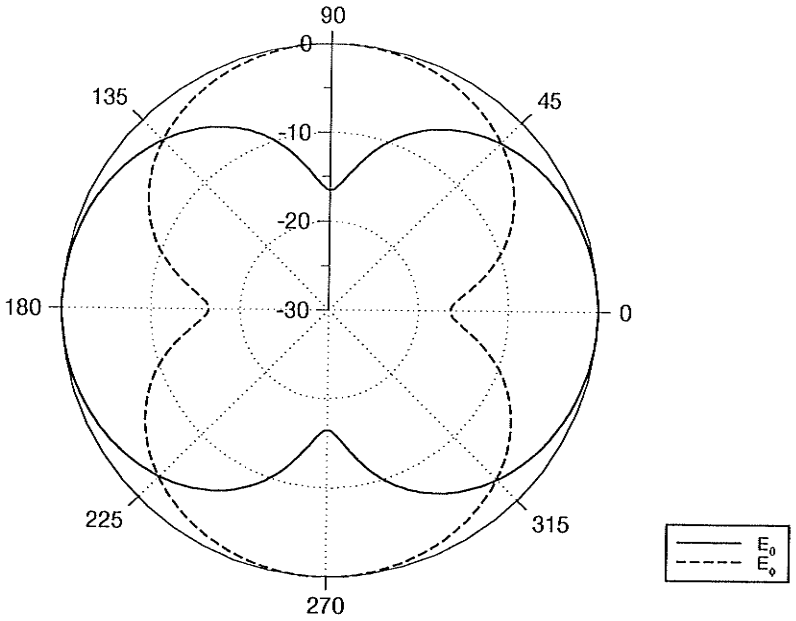

Figure 5.11: Radiation pattern of monopole antenna on a box, x-y plane, $\theta = 90^o$ and $L_z = 200mm$.

5.4.2 Bent-Slot Dipole

The bent-slot antenna was first developed by Kuboyama *et al.* [67] for UHF portable communication equipment. Two bent-slot antenna configurations are shown in Fig. 5.12. The box is assumed to be a rectangular conducting box.

Two of the six antenna configurations discussed in [67] will be modeled using the FDTD, Fig. 5.12. These two configurations are chosen based on the location of the slot. The other four configurations can be modeled directly with no difficulties and no special treatment is needed.

The conducting box in both types is modeled by forcing the tangential components of the electric fields on the surface of the box to zero, except for the portion of the surface that includes the slot. The slot is assumed to be of $\lambda/2$ length and the feed is modeled by exciting the center of the slot by a delta-gap voltage generator.

The computational space for type I is modeled by $70 \times 75 \times 95$ cells, which corresponds to $\Delta = 4\,mm$. This space increment is chosen so that the slot width is only one unit space step.

Fig. 5.13 shows E_ϕ and E_θ patterns in $x-y$ plane for a type I antenna. These patterns were generated by the vertical and horizontal parts of the slot, respectively, and are shown to be symmetrical figure-eight patterns orthogonal to each other. It is clear that the patterns obtained using the FDTD are perfectly symmetrical due to the symmetrical structure of the antenna. The E_ϕ and E_θ patterns in the vertical cut are shown in Fig. 5.14, it is clear that E_θ is nearly omnidirectional. The radiation patterns are normalized with respect to their maximum pattern value in each plane. Results obtained using FDTD match very well with the ones obtained by [67], with

a difference of about $1dB$ in the maximum beam direction.

Fig. 5.15 shows the radiation patterns for type II antenna. In the $x-y$ plane, the E_ϕ and E_θ patterns are nearly symmetrical figure-eight patterns orthogonal to each other. The asymmetrical patterns are due to the asymmetrical structure of the antenna. The E_θ pattern in the $x-z$ plane generated by the horizontal parts of the slot becomes nearly omnidirectional Fig. 5.16.

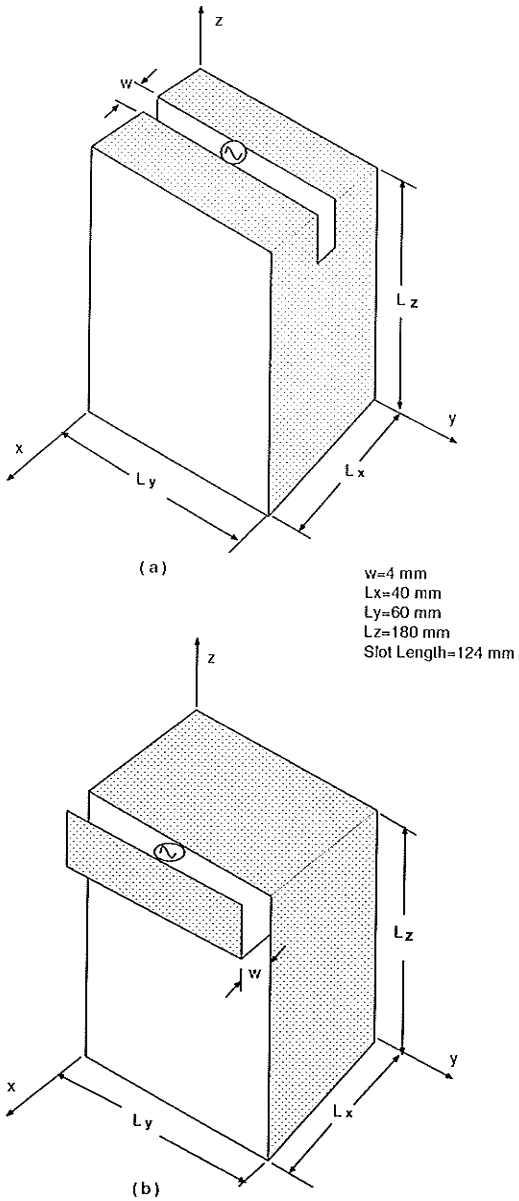

Figure 5.12: Bent-slot antenna on a rectangular box. (a) Type I. (b) Type II.

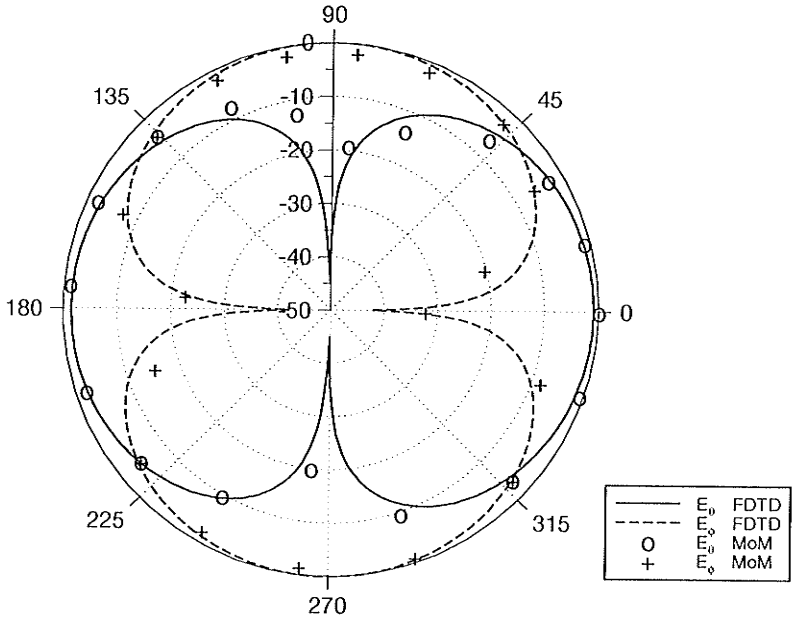

Figure 5.13: Radiation pattern due to bent-slot antenna, x-y plane, $\theta = 90^o$. Type I.

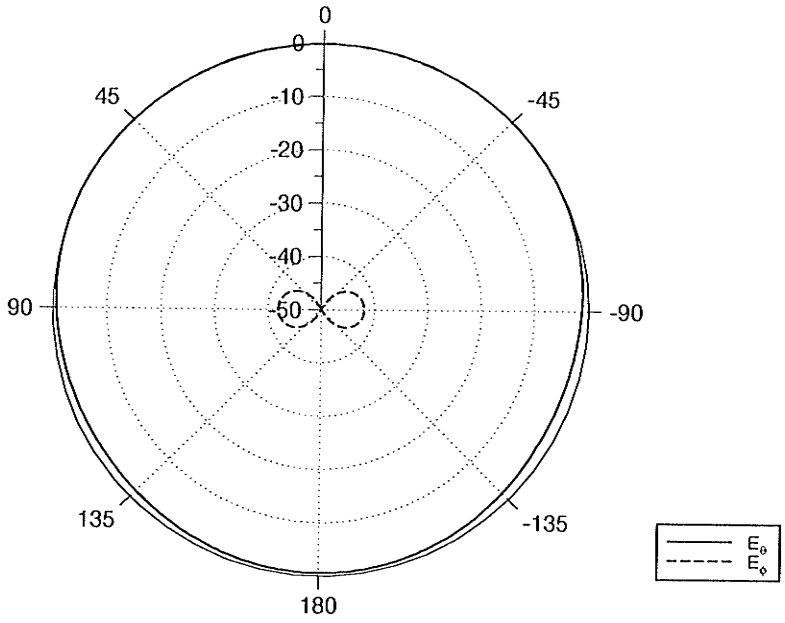

Figure 5.14: Radiation pattern due to bent-slot antenna, x-z plane, $\phi = 0^o$. Type I.

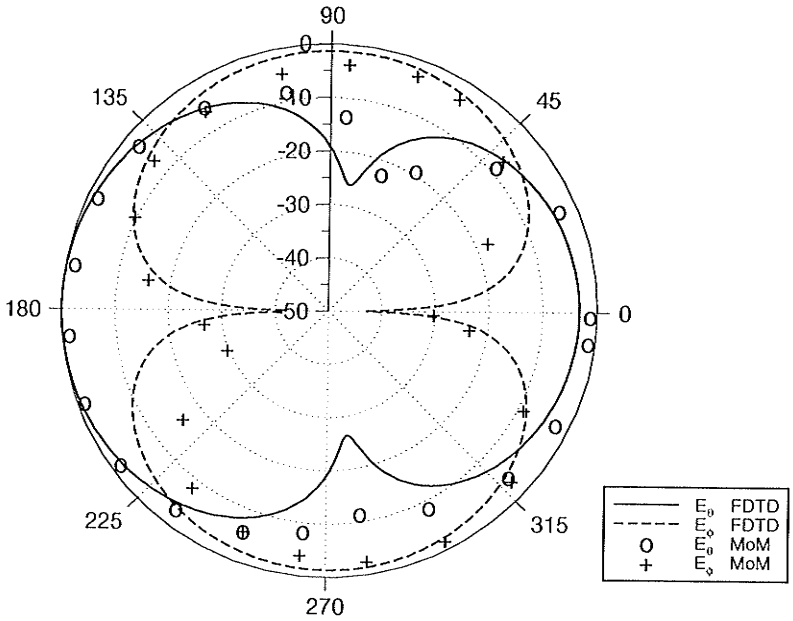

Figure 5.15: Radiation pattern due to bent-slot antenna, x-y plane, $\theta = 90^o$. Type II.

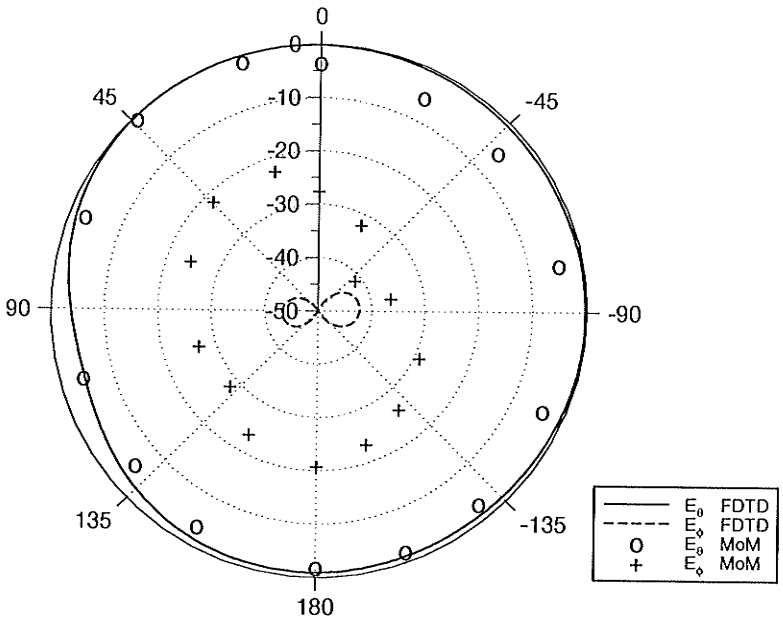

Figure 5.16: Radiation pattern due to bent-slot antenna, x-z plane, $\phi = 0^o$. Type II.

5.4.3 Monopole Mounted on a Car

The configuration of the automobile body and the monopole antenna is shown in Fig. 5.17. The antenna employed is a quarter-wavelength ($\lambda/4$) monopole and is located in the center of the roof. The bottom of the body is $0.4\,m$ high from the earth and the roof is $1.2\,m$ high from the earth. Nishikawa [68], used a simpler model in which he neglected the effect of the windshield and the interior of the automobile.

The radiation pattern is computed in two fundamental vertical planes, *i.e.* $x-z$ plane along the body length and $y-z$ plane along the body width. The vertical plane patterns are determined by the profile of the automobile body mounting the antenna. The FDTD geometrical model of Fig. 5.17 consists of three perfectly conducting plates representing the roof, engine hood and trunk hood of the body. Through all the simulations the engine hood and the trunk hood are assumed to lie in the horizontal (and thus are not slanted).

The FDTD computational space is taken as $153 \times 116 \times 68$ cells. The spatial stepping is taken to be ($\lambda/12$), which corresponds to $\Delta = 6.25\,cm$, the time stepping is taken to be, $\Delta t = \Delta/(2c)$ at $400MHz$ frequency.

Again the tangential components of the electric field on the conducting plates are set to zero, $E_x = E_y = 0$. Also the axial electric field tangential to the monopole surface is set to zero. The magnetic field components surrounding the wire is updated using the contour integral approach. The earth is simulated using a lossy material, the relative complex dielectric constant of the earth is given as $\varepsilon_g = \varepsilon_r - j\varepsilon_x$, where $\varepsilon_x = \sigma/(\omega\varepsilon_o)$, $\omega = 2\pi f$ with f the frequency of operation.

Fig. 5.18 and Fig. 5.19 show the radiation patterns of $\lambda/4$ monopole at the

center of the roof in the $x-z$ plane and $y-z$ plane, respectively. Results based on the GTD are also shown for comparison [68]. All patterns are normalized for the maximum value of the electric field in the $x-z$ plane. The value of ε_g for dry soil earth model used is $\varepsilon_g = 5 - j0.1$ at $400MHz$ frequency [68].

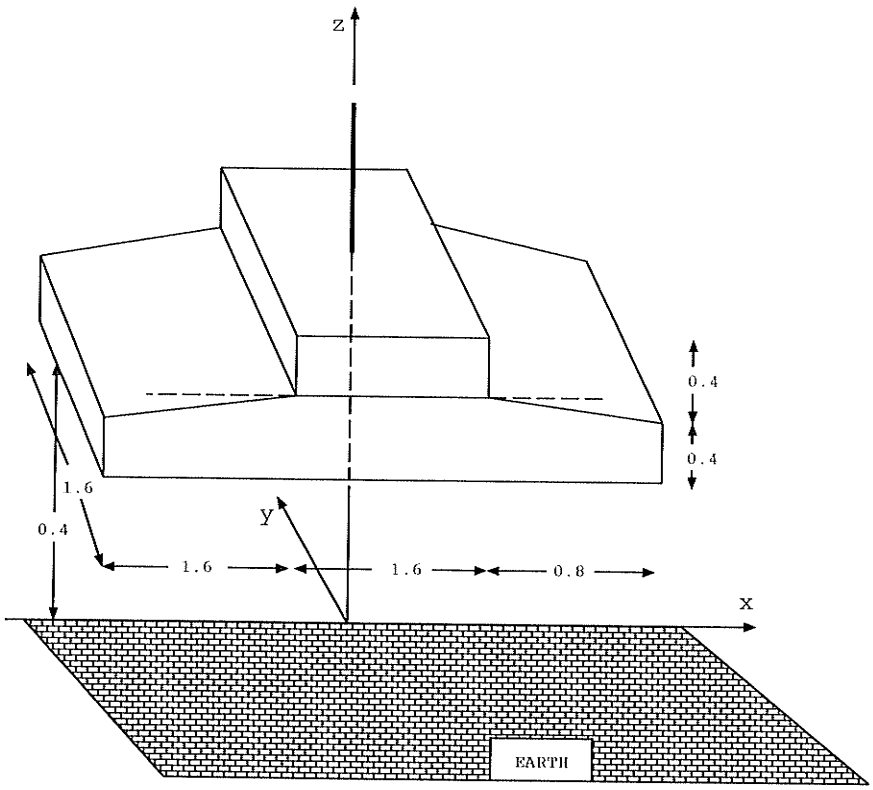

Figure 5.17: Mobile monopole antenna and Automobile model.

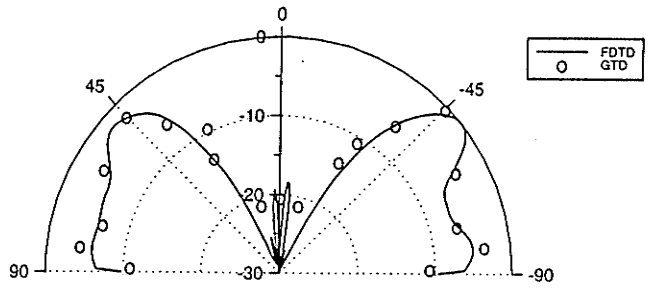

Figure 5.18: Radiation pattern E_θ from the automobile antenna, in the x-z plane

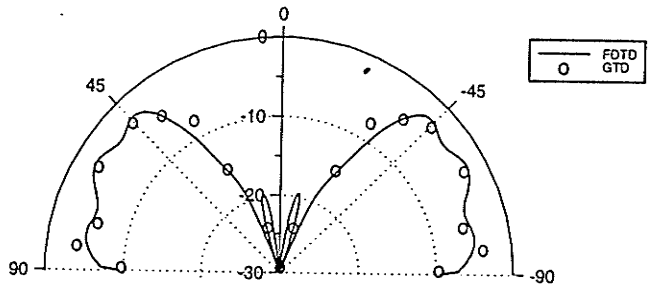

Figure 5.19: Radiation pattern E_θ from the automobile antenna, in the y-z plane

5.5 Antenna Radiated Power and Efficiency

The capabilities of the FDTD to calculate antenna radiation pattern and input impedance has been demonstrated successfully in previous chapters. This section proceeds to deal with antenna radiated power and efficiency. A pulse excitation will be used so that results for a wide range of frequency can be obtained from a single FDTD run.

The antenna used here is the same as the one discussed in Sec.4.4. The reason for choosing the dipole antenna is that comparison data can be obtained easily using the available MoM based Numerical Electromagnetic Code (NEC). The antenna structure and excitation will be repeated here for convenience only.

The dipole antenna is of 57 cm in length and 0.281 cm in radius. The problem space is $31 \times 31 \times 81$ cells, with the cell dimensions $\Delta x = \Delta y = \Delta z = 1.0cm$. Small radius approximation (contour integral method) is used to approximate the dipole radius. The dipole is center fed with a Gaussian pulse of $1.0V$ maximum amplitude, so that the electric field in the gap of the antenna is specified as,

$$E_z^n(i,j,k) = -V(n\Delta t)/\Delta z \tag{5.12}$$

where $V(t)$ is a Gaussian voltage source of the form,

$$V(t) = \exp -(t - t_o)^2/\tau^2 \tag{5.13}$$

with $t_o = 32\Delta t$ and $\tau = t_o/4$, and the pulse truncated for $t < 0$ and $t > 2t_o$. The time step was set to the Courant limit of $11.93ps$.

Using the same procedure discussed in Sec.4.4 the input current $I(t)$ and voltage $V(t)$ of the dipole antenna can be obtained using Eq. (4.14). Frequency domain data

can be obtained using a Fourier transform after all transients are dissipated. The equivalent steady-state input power is simply given at each frequency by,

$$P_{in}(\omega) = \frac{1}{2} Re\left[V(\omega) I^*(\omega)\right] \tag{5.14}$$

Dissipated power can also be computed in a simple way. Assuming that part of the antenna has a conductivity of σ and the electric field E_z is uniform within a single FDTD cell, then the equivalent steady-state power dissipated in a single cell is given by,

$$\begin{aligned} P_{dis}(\omega) &= \int_v \sigma \left|E_z(\omega)\right|^2 dv \\ &= \frac{\sigma \Delta x \Delta y}{\Delta z} \left|E_z(\omega) \Delta z\right|^2 \\ &= G \left|V_z(\omega)\right|^2 = \frac{1}{R} \left|V_z(\omega)\right|^2 \end{aligned} \tag{5.15}$$

where $E_z(\omega)$ is the Fourier transform of $E_z(i,j,k)$ at the location of the conductive cell. Therefore, it can be seen from (5.15) that the dissipated power can also be determined by considering the FDTD cell to contain a lumped resistor R with voltage V_z across the cell in the z-direction. When many FDTD cell locations contain dissipative materials Eq. (5.15) is repeated for each cell in each field component direction, and the total power dissipated is given by the sum. The efficiency of the system can be calculated as follows,

$$efficiency = \frac{P_{in} - P_{dis}}{P_{in}} \tag{5.16}$$

In order to illustrate this procedure a 50Ω resistance is placed 15 cells from the lower end of the dipole, the implementation of the resistance is done numerically. The input power is calculated using Eq. (5.14) and the result is compared with

that obtained using the MOM solution, Fig 5.20. The dissipated power in the 50Ω resistance and the total radiated power are shown in Figs. 5.21 and 5.22, respectively.

The result for the dipole efficiency is shown in Fig. 5.23 and compared with the result obtained using MoM solution. The agreement is quite good, except at the lower frequencies. The disagreement at lower frequencies can be attributed to the poor performance of the FDTD. This is because the antenna appears very shorts (electrically) and the voltage and current are almost 90° out of phase. Thus, a small error in the computed phase of the feed current will result in a large error in the value of P_{in}.

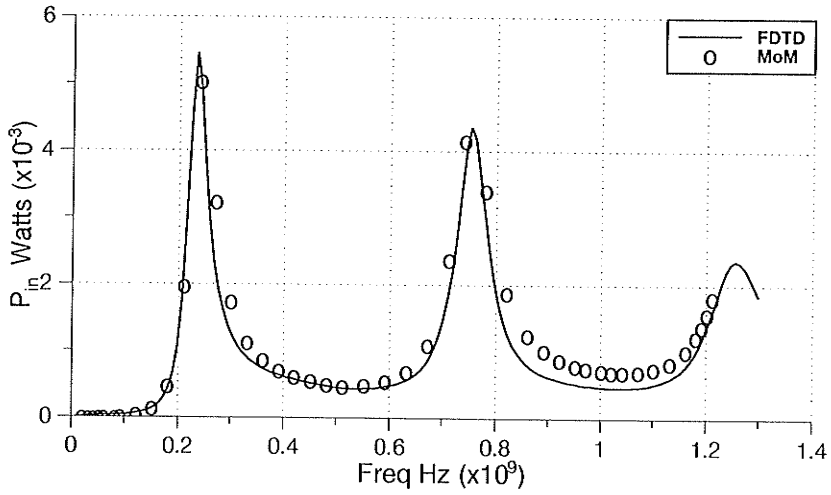

Figure 5.20: Input power for the dipole antenna.

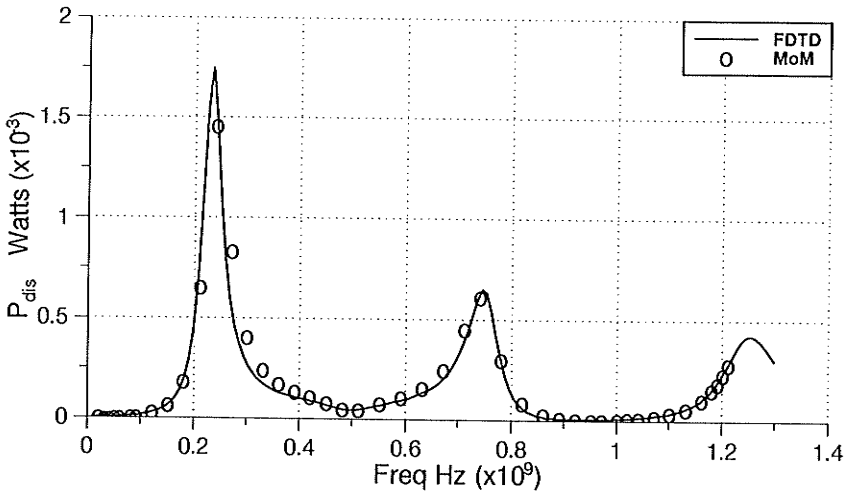

Figure 5.21: Power Dissipated in the 50 Ω resistance.

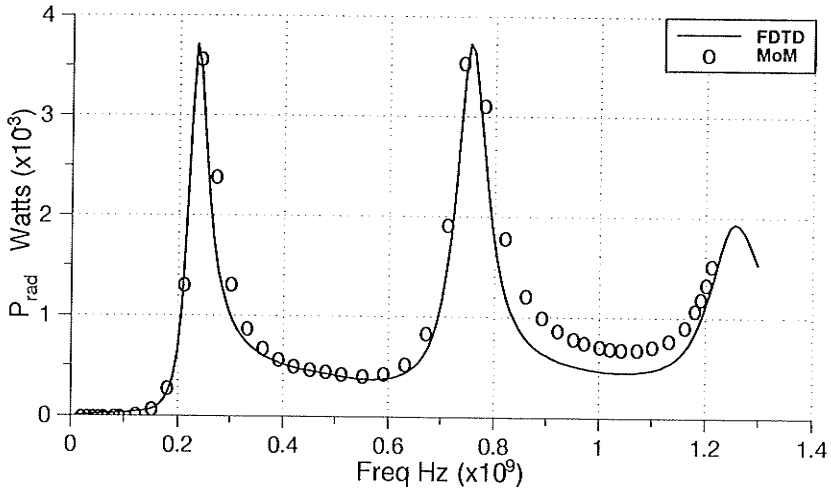

Figure 5.22: Dipole radiated power.

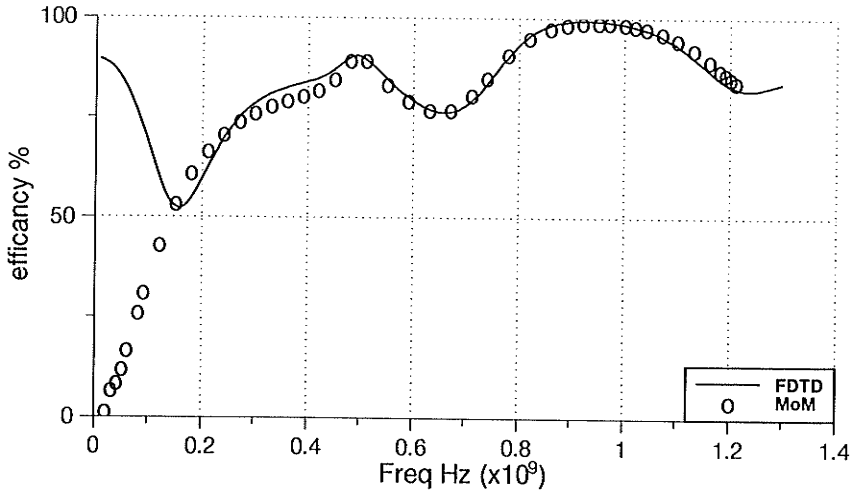

Figure 5.23: Antenna efficiency.

CHAPTER 6

Application to Planar Microstrip Circuits

6.1 Introduction

Microstrip antennas and planar printed circuits have gained a great deal of popularity in the past decade. This is due to a number of advantages such as low cost, low weight, low profile, conform-ability with existing structures, and ease of fabrication and integration of printed circuits with active devices.

Usually microstrip circuits and antennas are fabricated on a substrate, or on a number of substrates backed by a metallic sheet (conducting ground plane). For microstrip antennas the radiating elements consist of thin metallic patches or slots in a metallic sheet, located at an interface, commonly consisting of a dielectric and air. Practically, microstrip antennas can be classified into three categories based on the feed structure type. These are: a coaxial probe feed, a microstrip line feed, and an aperture-coupled feed. The coaxial-fed structure is often used with a single element or small array because of the ease of matching its characteristic impedance to that of the antenna. On the other hand, microstrip line-fed structures are more suitable for larger arrays due to the ease of fabrication and lower costs, however, the serious drawback of this feed structure is the strong parasitic radiation [69]. The aperture-coupled structure has all the advantages of the former two structures, and

isolates the radiation from the feed network, leaving the main antenna radiation uncontaminated. This feed structure was first proposed by Pozar [70].

Frequency domain analysis of microstip circuits has generally been done using planar circuit concepts in which the substrate is assumed to be thin enough that propagation can be considered in two dimensions by surrounding the microstrip with magnetic walls. Limitations of this method are that, fringing, coupling, and radiation must all be handled empirically. Also the accuracy is questionable when the substrate becomes thick relative to the width of the microstrip [36]. In order to fully account for these effects, it is necessary to use a full-wave solution.

Recently the FDTD method has been used by many authors to study the frequency-dependent characteristics of microstrip discontinuities [33] and [71]. Analysis of a line-fed microstrip patch antenna, a microstrip low-pass filter and a microstrip branch line coupler have been reported in [36]. The application of FDTD to the three types of feed structures has been reported in [72].

This chapter will discuss in details the choice of the excitation pulse and the application of the absorbing boundary conditions for microstrip applications. Later, three microstrip structures will be studied, these are a microstrip line, a microstrip line-fed patch antenna, and an aperture-coupled microstrip antenna.

6.2 Source Consideration and the Radiation Conditions

A sample microstrip structure used in most of the computation models is shown in Fig. 6.1. At time $t = 0$ all field quantities are assumed zero throughout the

computational domain. At time $t = 1$ an excitation pulse is launched underneath the microstrip line as shown in Fig. 6.1. The excitation pulse used in this study is a Gaussian pulse which has a smooth waveform in time, and its Fourier transform is also a Gaussian pulse centered at zero frequency. These characteristics make the Gaussian pulse a perfect choice for investigating the frequency-dependent characteristics of microstrip circuits.

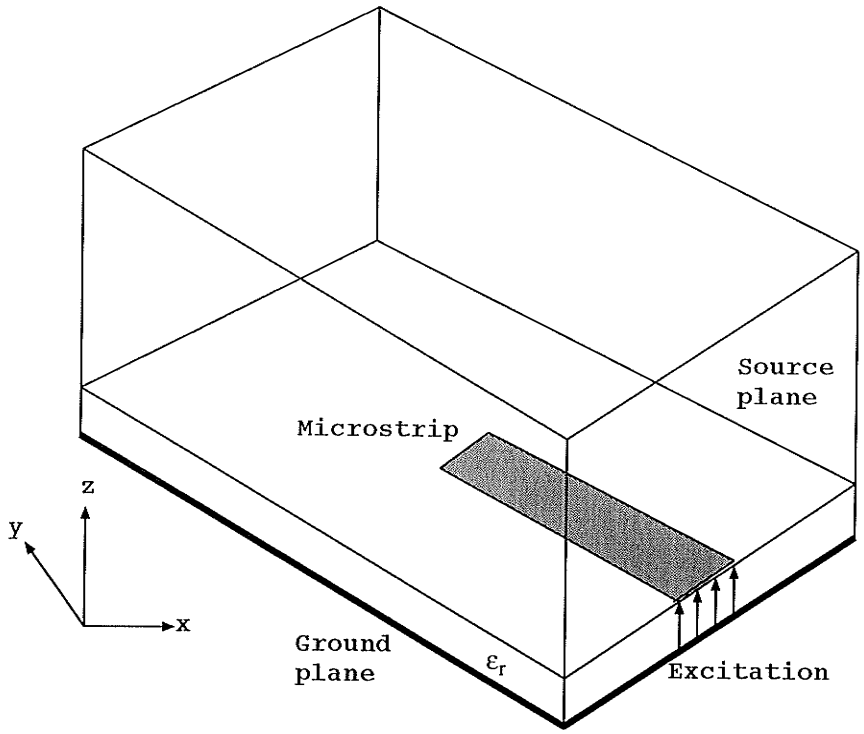

Figure 6.1: Microstrip geometry and computation domain.

An ideal Gaussian pulse which propagates in the positive y-direction takes the following expression [71],

$$E(t,y) = \exp\left[-\frac{\left(t - t_0 - \frac{y-y_0}{c}\right)^2}{T^2}\right] \tag{6.1}$$

where c is the velocity of the pulse in the specific medium, with the pulse maximum at $y = y_0$ at $t = t_0$. The choice of the parameters T, t_0 and y_0 are subject to two

requirements [71]. First, the pulse must be wide enough to contain enough space divisions for good resolution and at the same time to be narrow enough to maintain a substantial amplitude within the frequency range of interest. For that, the space discretization interval Δy has to be small enough to model the smallest dimension of the structure and the time increment has to be small enough to meet the stability criterion discussed in Chap. 2. If this requirement is not met a smaller Δy has to be used. The selected pulse width W is defined to be the width between the two symmetric points equal to 5 percent of the maximum value of the pulse. Therefore, T is given by

$$\exp\left[-\frac{(W/2)^2}{(cT)^2}\right] = exp(-3)(\approx 5\%) \tag{6.2}$$

or

$$T = \frac{1}{\sqrt{3}} \cdot \frac{10\Delta y}{c} \tag{6.3}$$

By making this choice of T, the maximum frequency which can be calculated is,

$$f_{max} = \frac{1}{2T} = \frac{1}{2}\frac{\sqrt{3}c}{10\Delta y} \tag{6.4}$$

The second requirement is that the choice of y_0 and t_0 be made such that the initial turn on of the excitation will be small and smooth.

Another important treatment which needs to be considered in modeling microstrip circuits is the absorbing boundary condition. As shown in Fig. 6.1, the structure consists of a ground plane and dielectric substrate toped with a thin conductor. These electric conductors are assumed to be perfectly conducting and have zero thickness. They are treated by setting the tangential components of the electric fields to zero. The edge of the conductor should be modeled with electric field

components tangential to the edge lying exactly on the edge of the microstrip. The remaining five boundaries have to be truncated using suitable absorbing boundary conditions. Due to the structure of the microstrip circuit, the pulses on the microstrip lines will be normally incident to the mesh walls. This leads to a simple approximation to the absorbing boundary conditions, that is the tangential fields on the outer boundaries obey the one-dimensional wave equation in the direction normal to the mesh walls. This leads to a Mur first order absorbing boundary condition as discussed in Sec. 3.2. It should be noted here that Mur second order absorbing boundary conditions which accounts for oblique incidence will not work on the mesh walls of the microstrip structure and yield an unstable solution. It should be noted also that the normal incidence assumption is not valid for fringing (evanescent) fields which are propagating tangential to the walls. Therefore, the sidewalls should be far away so that the fringing fields are negligible at the walls. Another way to improve the behavior of the absorbing boundary condition is to use the modified absorbing boundary condition discussed in Sec. 3.4, or to implement a dispersive boundary condition scheme, [73] and [74]. One final note regarding the absorbing boundary condition is, special care should be taken when applying the absorbing boundary at the source plane. During the launching period of the Gaussian pulse no absorbing boundary is assigned to the plane, however, once the pulse has passed the source plane and starts propagating inside the grid, the absorbing boundary should be switched on to absorb any incoming wave from the computational grid.

6.3 Microstrip Lines

Microstrip lines are considered an essential structure in microstrip antennas, and microstrip circuits. They are the basic building structure of these circuits. Consider the microstrip line given in Fig. 6.2, the 50Ω microstrip line is assumed match terminated in the y-direction.

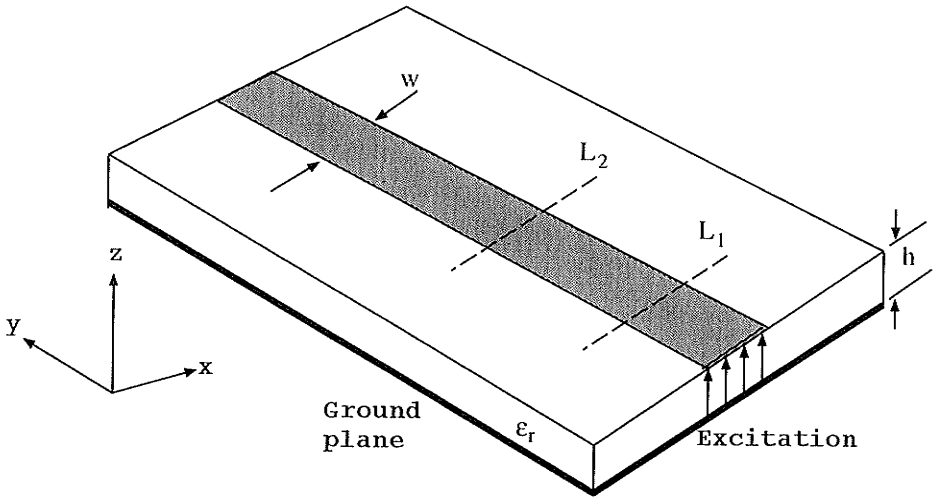

Figure 6.2: Microstrip line geometry.

This specific example is selected from [75]. The width of the strip line is $W = 2.54mm$ and the height of the substrate $h = 0.762mm$, with $\varepsilon_r = 2.22$. The substrate and the ground plane are modeled using two space cells, thus, $\Delta z = 0.381mm$. The other two dimensions are taken to be of the same length as Δz. The total mesh size used for this simulation is $60 \times 120 \times 30$ cells.

One important parameter that can be obtained from this simulation is the effective dielectric constant $\varepsilon_{reff}(\omega)$, which can be used to account for the dispersive characteristics of the microstrip line [33]. The effective dielectric constant $\varepsilon_{reff}(\omega)$ can be calculated by taking the Fourier transform of $E_z(t)$ at two different positions

underneath the center of the microstrip, with separation $L = L_2 - L_1$ along the propagation direction see Fig. 6.2,

$$E_z(\omega, y = L_1) = \int_{-\infty}^{\infty} E_z(t, y = L_1) e^{-j\omega t} dt \tag{6.5}$$

$$E_z(\omega, y = L_2) = \int_{-\infty}^{\infty} E_z(t, y = L_2) e^{-j\omega t} dt \tag{6.6}$$

Taking the ratio of (6.5) and (6.6), one gets the transfer function of this section of the microstrip line as follow,

$$e^{-\gamma(\omega)(L_2 - L_1)} = \frac{E_z(\omega, y = L_2)}{E_z(\omega, y = L_1)} \tag{6.7}$$

where

$$\gamma(\omega) = \alpha(\omega) + j\beta(\omega) \tag{6.8}$$

$\alpha(\omega)$ is the attenuation constant and can be neglected due to the fact that the microstrip line is assumed perfectly conducting. Therefore, $\varepsilon_{reff}(\omega)$ is defined through $\beta(\omega)$ as,

$$\varepsilon_{reff}(\omega) = \frac{\beta(\omega)^2}{\omega^2 \varepsilon_o \mu_o} \tag{6.9}$$

The propagation behavior of the vertical electric field component E_z at different positions along the propagation direction just underneath the microstrip line is provided in Fig. 6.7. The dispersive properties of the microstrip line are observed in the distortion of the pulse as it propagates away from the plane source. The variation of the effective dielectric constant with frequency is given in Fig. 6.8 along with a comparison obtained using the empirical formulas discussed in [76]. It is clear that the FDTD results agree very well with [76] over most of the frequency range.

The variation of the characteristic impedance with frequency, $Z_c(\omega)$, is obtained through the relation $V_{in}(\omega)/I_{in}(\omega)$. Here $I_{in}(\omega)$ is the Fourier transform of the input current defined as the loop integral of the magnetic fields surrounding the metal microstrip. $V(\omega)$ is calculated by taking the Fourier transform of the line integral of the vertical electric field, $E_z(t)$, under the center of the microstrip. Fig 6.9 shows the spectrum of $Z_c(\omega)$ of the microstrip line.

Now reconsider the above microstrip line, with the exception that the line is open circuited rather than match terminated, Fig 6.3 (a). The transient response of the electric field E_z just underneath the microstrip line is given in Fig 6.10. It is clear that the incident pulse has reflected with minimum amount of distortion. The magnitude of the reflected pulse is slightly lower than that of the incident pulse, indicating some loss due to radiation from the unmatched open end.

The scattering matrix of the open end microstrip line contains one element only, S_{11}, and it is defined as [71],

$$S_{11}(\omega) = \frac{V_{ref}(\omega)}{V_{inc}(\omega)} \tag{6.10}$$

where $V_{ref}(\omega)$ is the transformed reflection voltage at the open end discontinuity, and $V_{inc}(\omega)$ is the transformed incident voltage at the same position. In this calculation, $V_{ref}(\omega)$ is observed at the reference plane $T-T'$, $30\Delta y$ from the source plane, Fig 6.3 (a), which is located far enough from the discontinuity to allow the separation of the incident and reflected pulses. Thus, transmission line formula (6.10) can be calculated as [71],

$$S_{11}(\omega) = \frac{V_{ref}(\omega)e^{\gamma(\omega)L}}{V_{inc}(\omega)e^{-\gamma(\omega)L}} \tag{6.11}$$

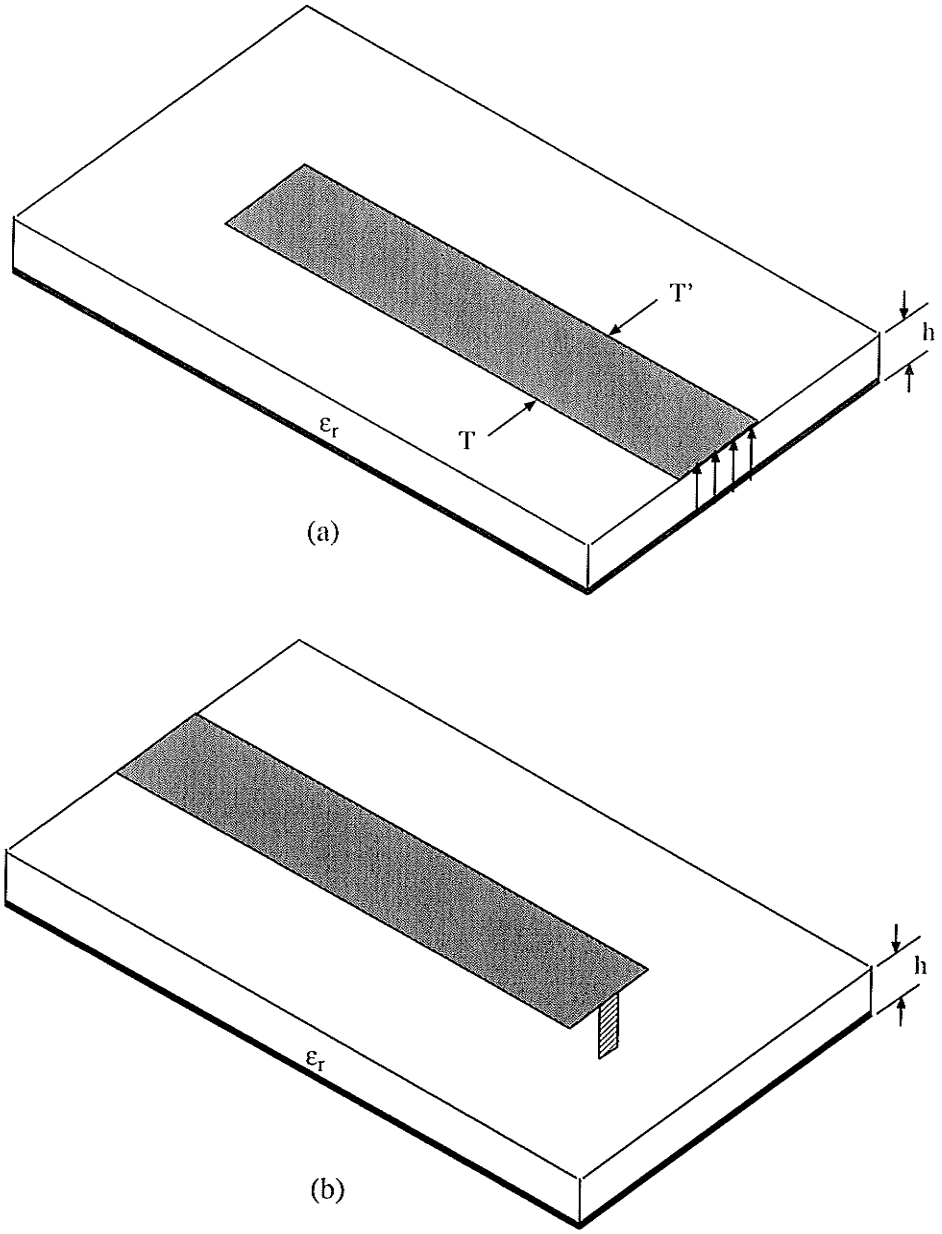

Figure 6.3: Geometry of, (a) open end microstrip line, (b) matched open-end microstrip line.

where L is the displacement of the reference plane from the discontinuity. Fig. 6.11 shows the calculated results of the magnitude and the phase of $S_{11}(\omega)$ for the open end microstrip line under consideration.

The last experiment in this section is to match terminate the open-end microstrip line by a 50Ω lumped resistance Fig 6.3 (b). The implementation of the lumped resistance is accomplished using the technique discussed in Sec. 4.3. The termination effect is evident in Fig. 6.12, where the reflected pulse observed in Fig. 6.10 is almost eliminated.

6.4 Microstrip Line-Fed Patch Antenna

The detailed geometry of the line-fed rectangular microstrip antenna is given in Fig. 6.4. This antenna can be easily modeled using FDTD. The height of the

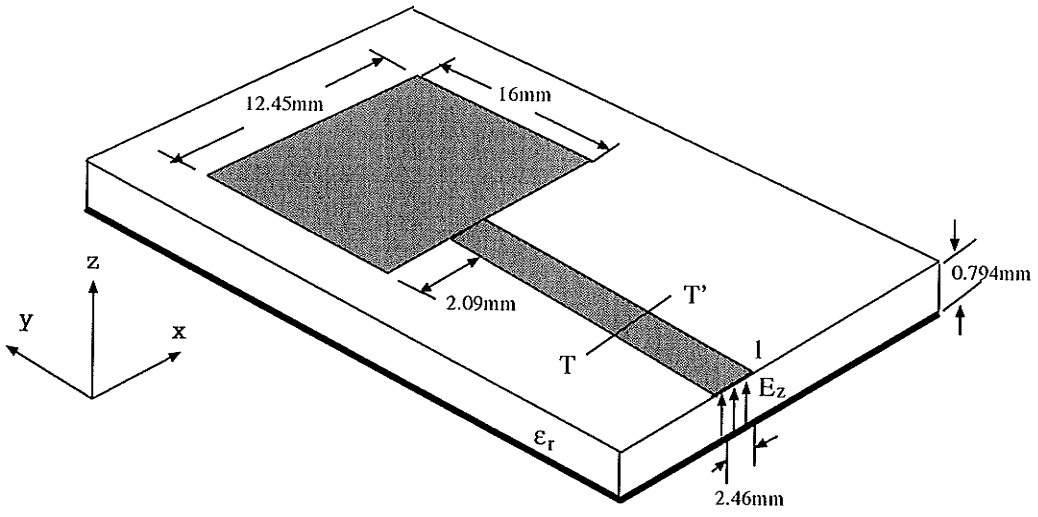

Figure 6.4: Line-fed rectangular microstrip antenna.

substrate is modeled using three cells, therefore, $\Delta z = 0.265\ mm$. In order to

model the dimensions of the patch correctly in the x and y directions, Δx and Δy are chosen so that an integer number of nodes will fit the patch. Thus, the remaining space increments are, $\Delta x = 0.389\ mm$ and $\Delta y = 0.4\ mm$, which results in patch dimensions of $32\Delta x \times 40\Delta y$. The width of the microstrip line is modeled using 6 cells in the x direction, and 50 cells are used to model its length. The total mesh dimensions used to model the antenna and the surrounding space are $60 \times 100 \times 16$ in the x, y, and z directions, respectively. The time step Δt is chosen such that $\Delta t = \Delta z/(2c) = 0.4416pS$. A Gaussian pulse with $T = 34\Delta t$ and $t_0 = 3T$ is launched at $t = 0$ underneath the microstrip line and switched off immediately after it passes the source plane. The simulation continued for 7500 time step. The application of the absorbing boundary condition at the source plane has been implemented five cells away from the source plane. This will eliminate any undesirable effects of switching from source to absorbing boundary.

The return loss $S_{11}(\omega)$ is calculated using (6.10) at reference plane $T-T'$ which is displaced a distance of $40\Delta y$ form the edge of the patch. The spatial distribution of $E_z(x, y, t)$ just beneath the microstrip patch at $200, 300, 400,$ and600 time steps are shown in Fig. 6.13. The transient response of the electric field E_z, just underneath the strip line, used in calculating $S_{11}(\omega)$, is shown in Fig. 6.14. The return loss results are provided in Fig. 6.15, with the operating resonance at 7.5 GHz almost exact while additional resonances are observed and they are in very good agreement with [36].

The input impedance of the antenna can be calculated from $S_{11}(\omega)$, by trans-

forming the reference plane to the edge of the microstrip patch *i.e.*,

$$Z_{in}(\omega) = Z_c \frac{1 + S_{11} e^{2jkL}}{1 - S_{11} e^{2jkL}} \tag{6.12}$$

where k is the wave number on the microstrip, L is the length from the reference plane $T - T'$ to the edge of the microstrip patch, and Z_c is the characteristic impedance of the microstrip line, assumed constant at 50 Ω with an effective permittivity of 1.9 is used to calculate the wave number. Input impedance results near the operating frequency are shown in Fig. 6.16, it is noticed that at the resonance frequency the input impedance is close to 50 Ω.

6.5 Aperture-Coupled Microstrip Antenna

The treatment of the aperture coupled microstrip antenna is similar to that of the microstrip line-fed patch antenna, except for the coupled microstrip antenna the microstrip patch is located on one substrate and the feed network is on another substrate Fig 6.5. These two substrates are separated by a conducting ground plane with a slot on it to allow for power coupling from the feed network to the patch antenna. The example used for the FDTD simulation is selected after [77]. Both substrates are defined to have the same permittivity, $\varepsilon_{ra} = \varepsilon_{rb} = 2.54$, the height of both substrates is assumed equal, $h_a = h_b = 1.66\ mm$. The other antenna dimensions, which are clarified in Fig. 6.6 are as follow, $W_L = 4.8mm, W_a = 1.66mm, L_a = 11.2mm, L_s = 20.4mm, L_x = 40.0mm$ and $L_y = 30.4mm$. The total grid size used for this simulation is $60 \times 130 \times 30$ cells with $\Delta x = \Delta y = \Delta z = 0.8mm$. Similar to the microstrip line-fed patch antenna, a Gaussian pulse with $T = 20\Delta t$ and $t_0 = 4T$

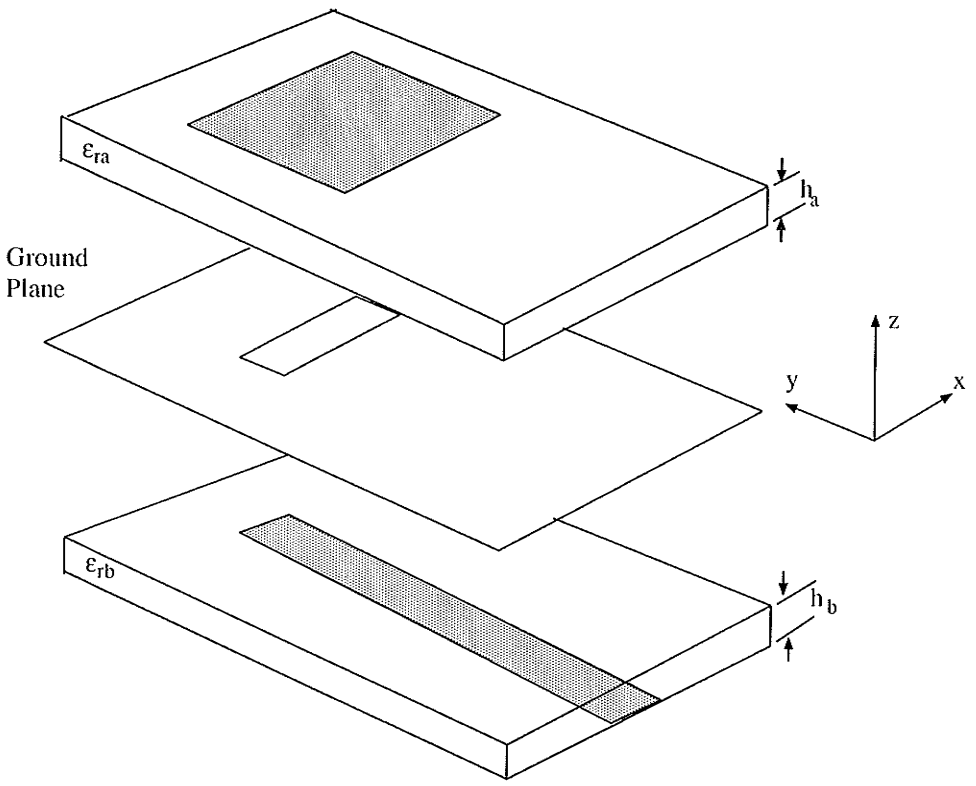

Figure 6.5: 3-D geometry of aperture-coupled microstrip patch antenna.

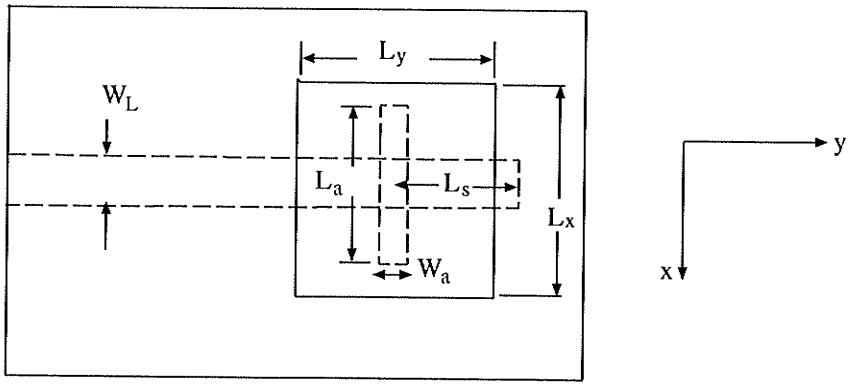

Figure 6.6: Geometry of aperture-coupled microstrip patch antenna, x-y plane.

is launched at $t = 0$ underneath the ground plane and above the microstrip line. The time step Δt is chosen such that $\Delta t = \Delta z/(2c)$.

The spatial distribution of $E_z(x, y, t)$ just beneath the microstrip patch at $200, 300, 400$, and 600 time steps are shown in Fig. 6.17. The transient response of the electric field E_z on the microstrip line close to the slot is given in Fig. 6.18. One can easily observe that the first pulse is due to the incident pulse, followed by the first reflected pulse due to the slot, and the second reflected pulse due to the open end strip line.

The return loss results are provided in Fig. 6.19 and were obtained using Eq. (6.10). The first resonance is observed at the design frequency of $2.2GHz$ and the other one is observed at $6.27GHz$.

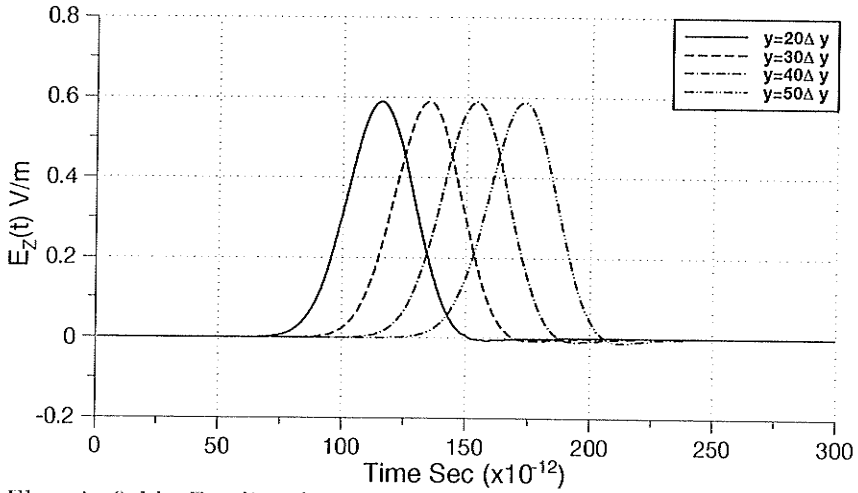

Figure 6.7: Electric field, E_z, distribution just underneath the strip line at different positions a long the y-axis.

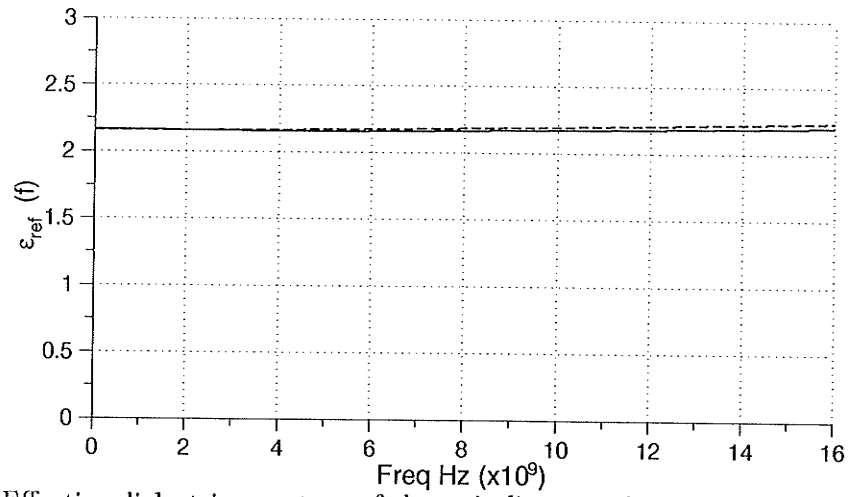

Figure 6.8: Effective dielectric constant of the strip line as a function of frequency, FDTD (solid) and microstrip theory (dashed).

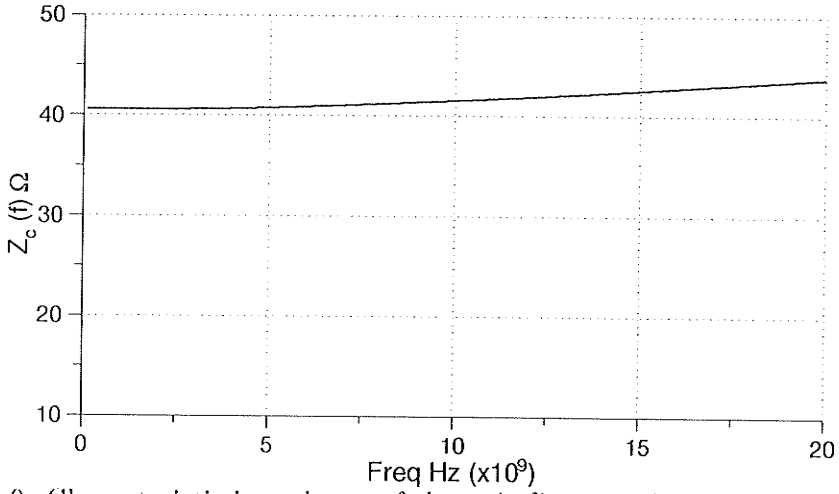

Figure 6.9: Characteristic impedance of the strip line as a function of frequency.

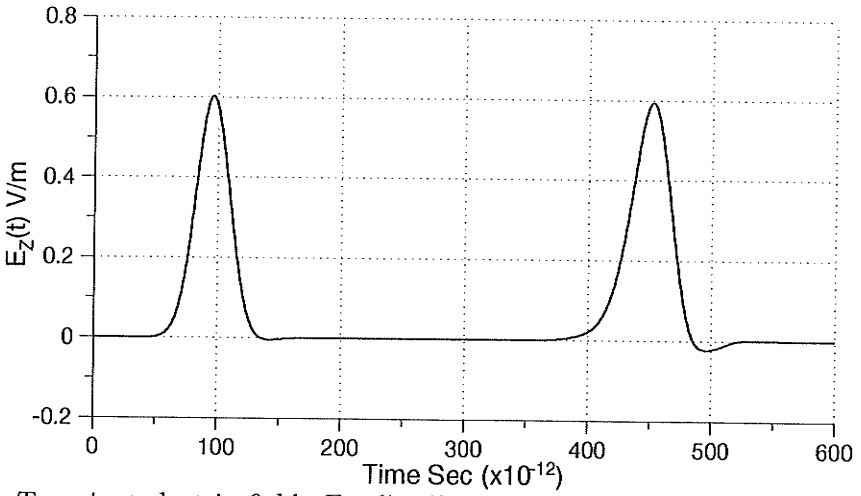

Figure 6.10: Transient electric field, E_z, distribution just beneath the open end strip line at a distance $L = 3.81mm$.

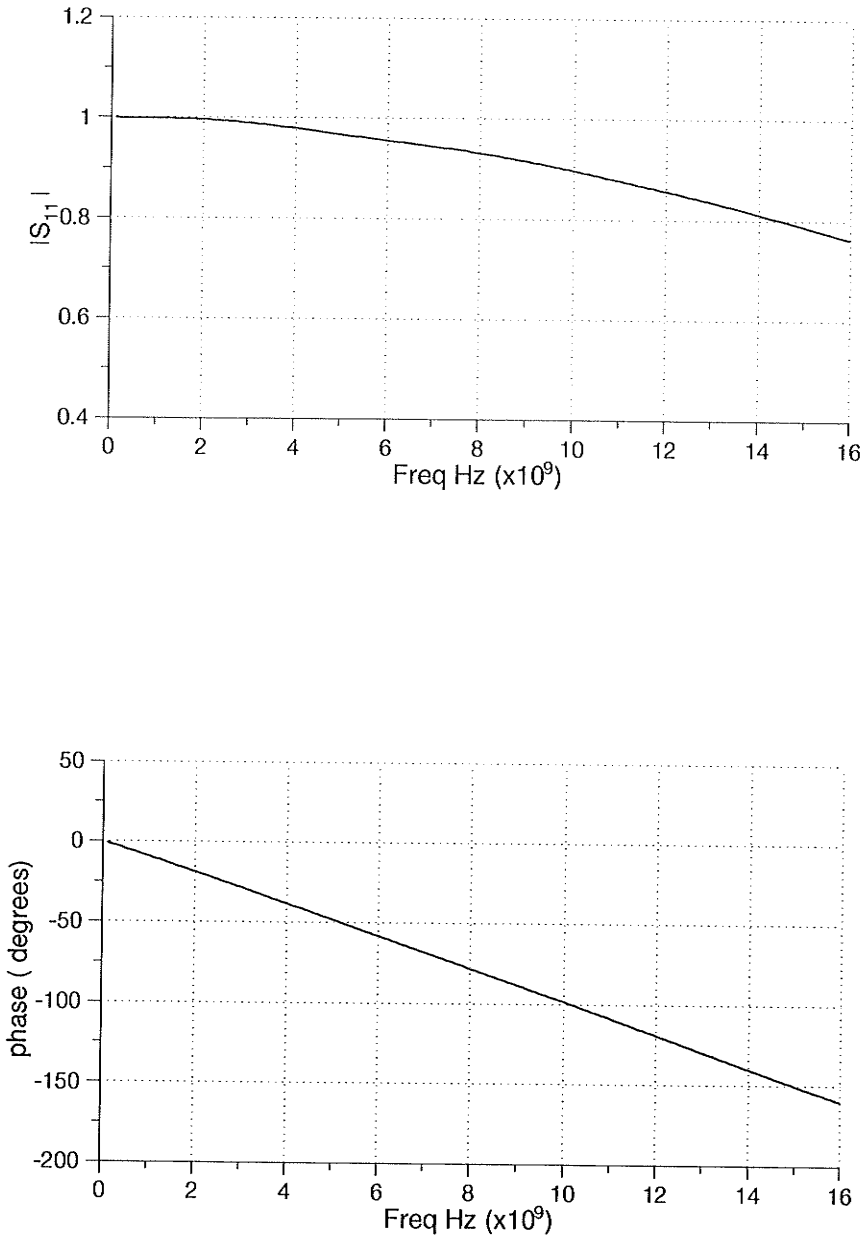

Figure 6.11: Magnitude and phase of the frequency dependent S_{11} parameter of the open end strip line.

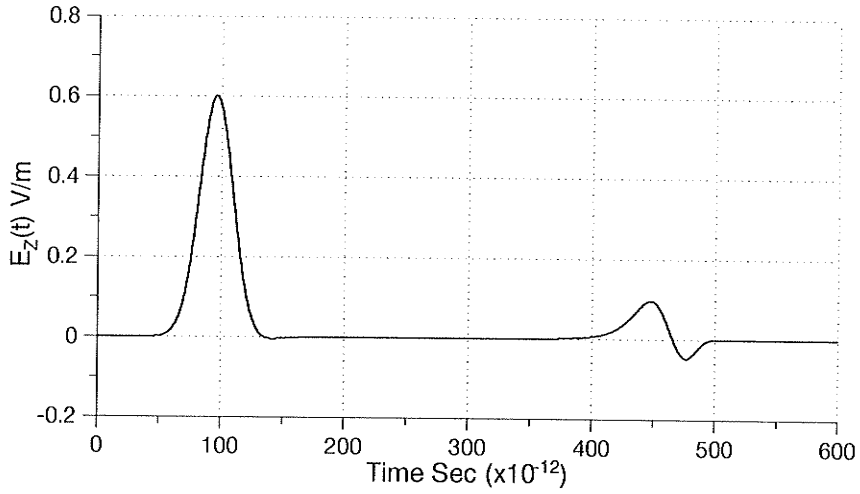

Figure 6.12: Transient electric field, E_z, distribution just beneath the open end 50Ω match terminated strip line at a distance $L = 3.81mm$.

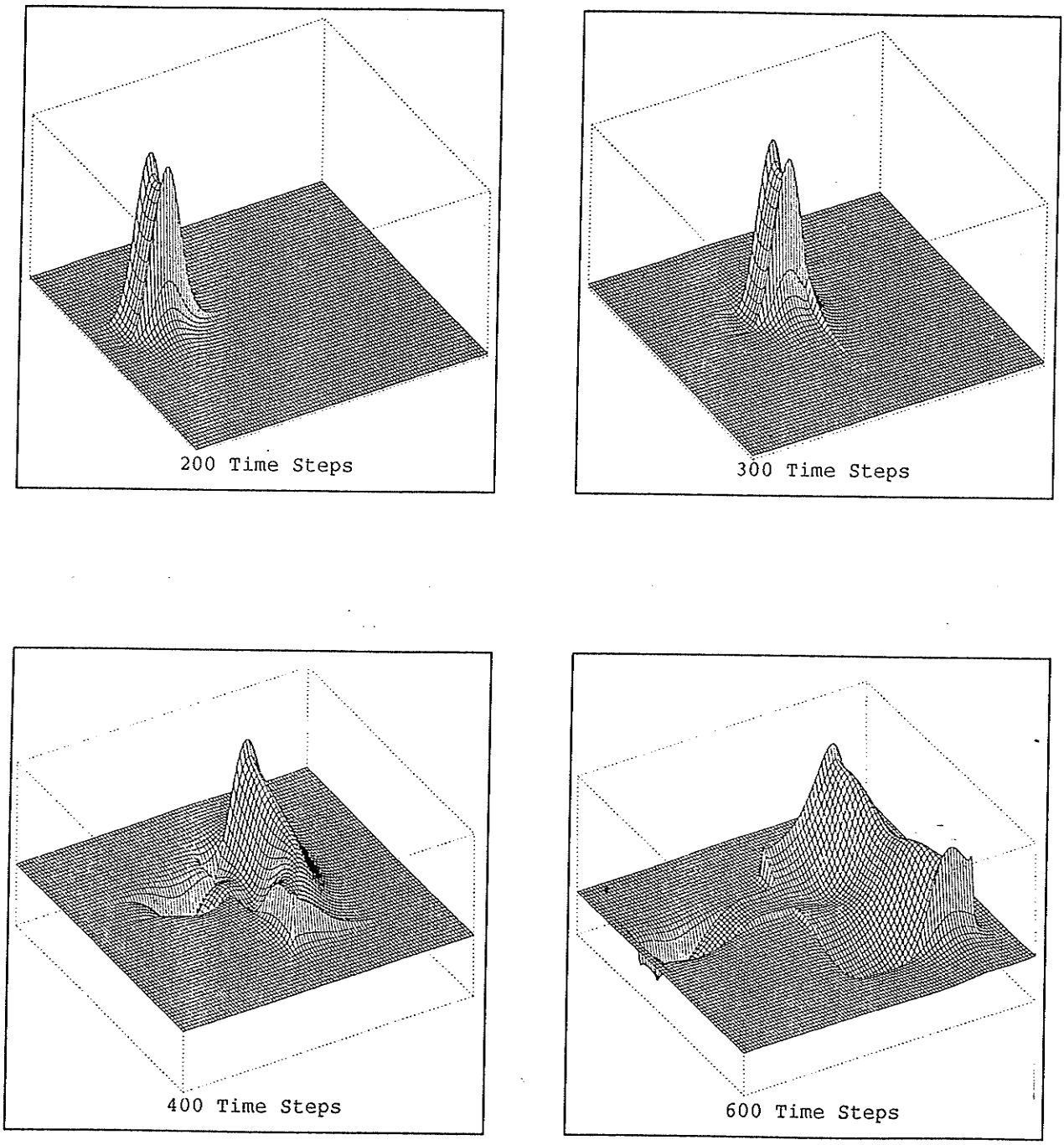

Figure 6.13: Distribution of $E_z(x, y, t)$ just underneath the dielectric interface of the line-fed microstrip patch antenna at 200, 300, 400 and 600 time steps.

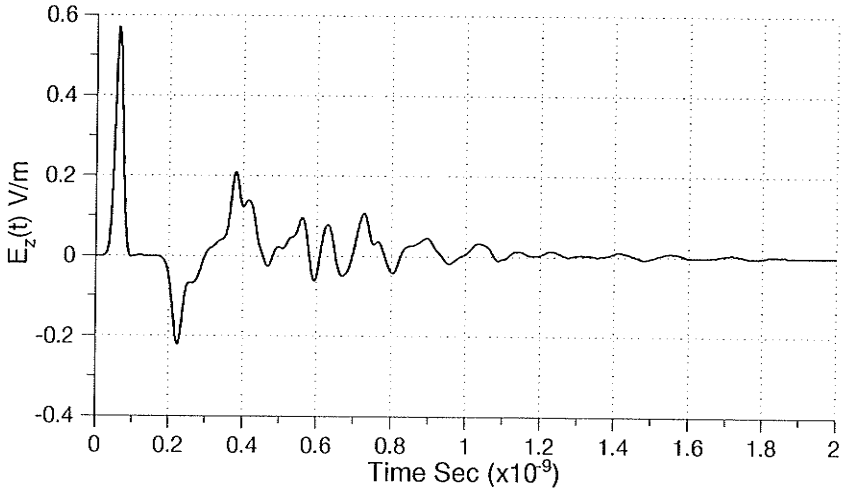

Figure 6.14: Transient electric field, E_z, distribution just beneath the strip line of the microstrip patch at a distance $L = 40\Delta y$ from the patch edge.

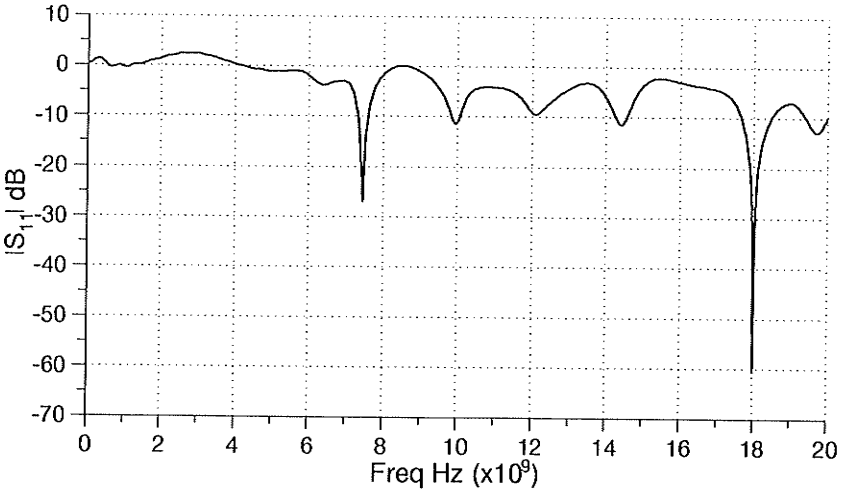

Figure 6.15: Return loss S_{11} of the microstrip patch antenna.

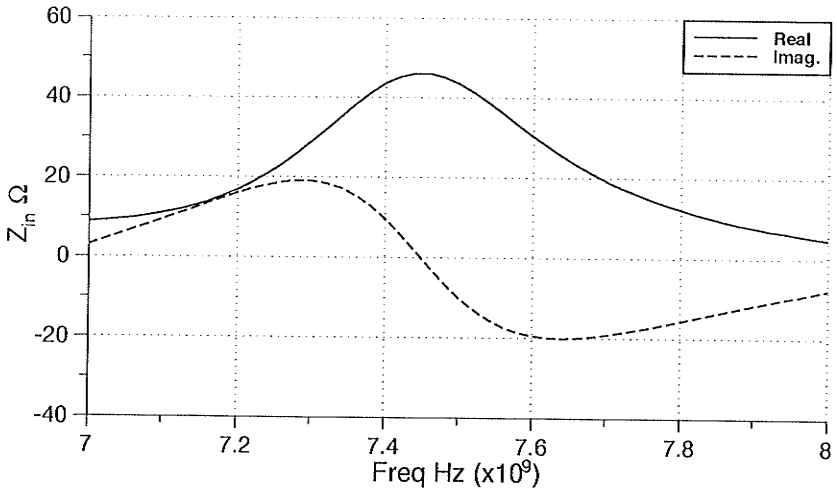

Figure 6.16: Input impedance of the microstrip patch antenna near the operating resonance at $7.475GHz$.

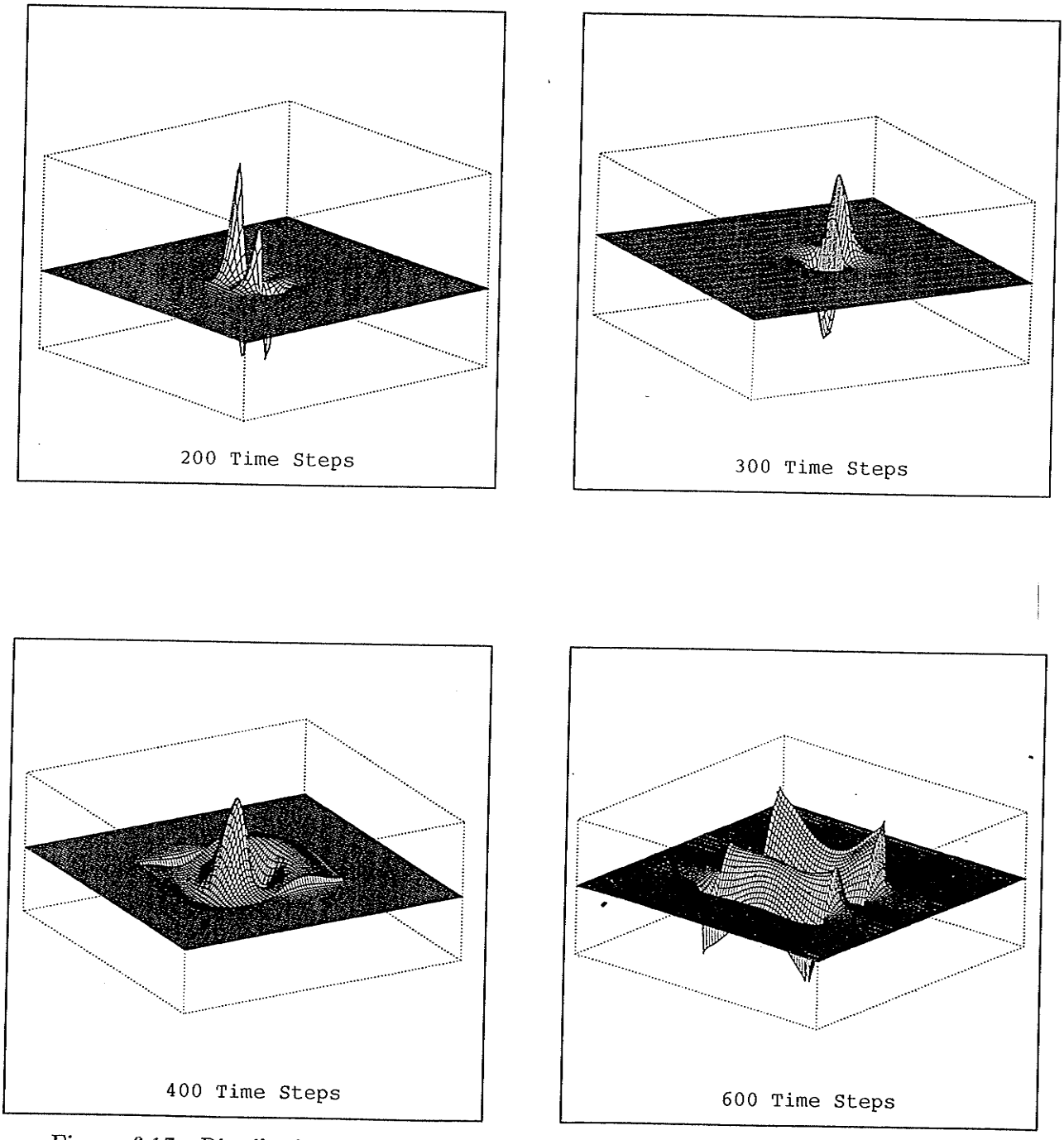

Figure 6.17: Distribution of $E_z(x, y, t)$ just underneath the dielectric interface of the microstrip patch of the aperture-coupled microstrip antenna at 200, 300, 400 and 600 time steps.

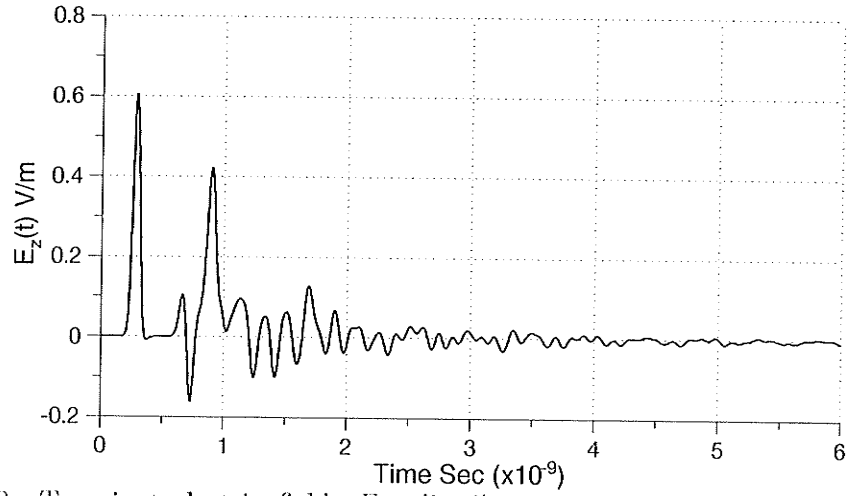

Figure 6.18: Transient electric field, E_z, distribution just above the strip line of the aperture-coupled microstrip antenna at a distance $L = 80\Delta y$ from the open end of the strip line.

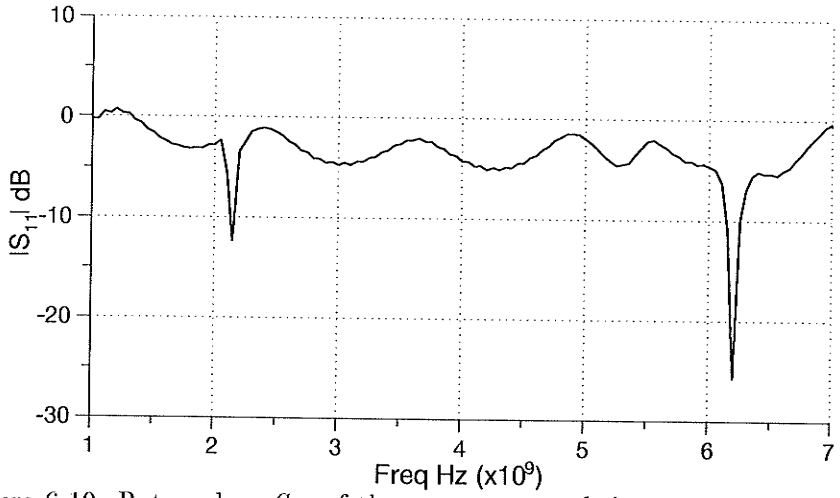

Figure 6.19: Return loss S_{11} of the aperture-coupled microstrip antenna.

CHAPTER 7

Application to EM Interference and Compatibility

7.1 Introduction

Many environments have high levels of electromagnetic radiation due to a concentration of transmitting devices. Other types of electrical equipment generate leakage of electromagnetic radiation during operation even though it is not their function to radiate. Unwanted radiation from sources such as these can interfere with the operation of many electrical equipment. A very good example of such interference is that experienced by a navigation system on board of a ship.

All ships have a navigation and communication system on board, which operates at high frequencies in the HF and VHF ranges, in addition to the presence of commercial computing and monitoring equipment, as well as power generation and propulsion equipment. All these equipments add to the complexity of the operating environment. High VHF signal power levels interfere with the computing equipment and corrupt collected navigation data. Coupling of high level RF signals into the computing equipment occurs via power and interface cables, and via direct entry through cabinet or enclosure apertures. Time varying magnetic fields generated by

rotating machinery could influence and degrade the performance of a nearby high resolution color monitor.

The immunity of electrical equipment against any electromagnetic interference is known as the susceptibility of the system. It is thus important to test electrical equipment to determine how well it functions when subjected to unwanted electromagnetic radiation, and how will is it shielded against unintentional electromagnetic interference, EMI.

Another victim of EMI is printed circuit boards, PCB. The EMI emission source that most modern digital electronic devices have in common is the direct current (DC) bus that supplies and distributes necessary electric power to integrated circuits. DC buses are used in almost all digital electronic devices, including satellite transmitters and receivers, electronic tools for medical research and care, personal computers, cellular and cordless telephones, and electronic games and toys. The DC bus becomes an unintentional radiating antenna when minute residual switching signals are emitted from the ICs. The simultaneous switching current at 200 MHz or at higher rates will induce on the DC bus a considerable current fluctuation at the clock frequency rate. Therefore, the DC bus plays a crucial role in coupling EMI from switching solid-state devices to both conducted and radiated paths. Predicting EMI from DC buses in digital equipment is a vast topic, a literature review on EMI in printed circuit boards has been done by Gravelle and Wilson [78]. The study provides a very good discussion on the EMI sources and the measures needed to insure voltage and current waveform integrity throughout the interconnecting paths. The suppression of conducted and radiated emission, and hardening against

susceptibility failure are also discussed.

Thus, the problem of EMI/EMC can be classified into two classes. The first class is an intrasystem problem, for which the EMI may come from within the system. The causes of such EMI may be owed to printed circuits, clock, and switching transients. The second class of EMI is the intersystem problem, which may come from outside causes and applications such as radio transmitters, microwave relay, air craft, local oscillator, radar transmitters, power lines and generators, and lightning strokes.

Electromagnetic test chambers were developed to provide shielding from external electromagnetic radiation, and to provide an environment in which standardized electromagnetic radiation test procedures could be developed for many types of radiation sources. In order to determine the susceptibility of a device to radiation using these test chambers, the device must be subjected to the radiation frequencies and field strengths that are representative of the environment in which the device will operate. However, measurement equipment itself can produce changes in the test environment which may be critical in the interpretation of the results. Therefore, an overall characterization of the EMC test or actual operational environment is necessary for a complete study of EMC.

There is a great deal of complexity in the shape, interconnections and details of actual real life equipment and systems. Modeling such equipment is not an easy task. Some of the features necessary in the modeling method suitable for EMC studies are discussed in [79], [80], they are:

- it must be capable of modeling complex shapes,
- it must permit simultaneously the modeling of regions inside and outside a

shield,

- it must be capable of modeling wire like structures,
- it must be suitable for modeling space with inhomogeneous properties,
- it must be capable of dealing with open boundary problems,
- its application and interpretation must retain as much physical meaning as possible, to allow the user some feel of the nature of simplifications and assumptions necessary in any exercise of such complexity.

No numerical method can score the maximum in all items in the list above, however, some methods are better suited to EMC problems, *ex.*, Method of Moments, finite difference time domain and transmission-line modeling.

7.2 Field to Wire Coupling

A generic EMC problem can be described as an equipment shield, which may consist of metallic or carbon-fiber composite parts and open slits (apertures). Part of the EM energy penetrates through parts of the shield and couples into the system (device) wiring and often through other penetrations of the shield such as power cables, add further paths where EM radiation can couple into equipment.

An ideal EMC problem is given in Fig. 7.1 with the goal here to study the field coupling to a wire placed inside a shielded enclosure, where such a problem requires simultaneous modeling of the regions internal and external to the enclosure, apertures and wires. Two examples are considered for this application. In the first

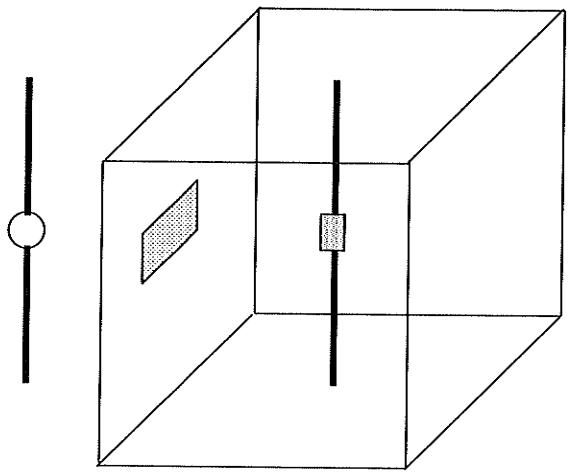

Figure 7.1: Generic EMC problem geometry.

example a perfectly conducting box of dimensions $0.36 \times 0.6 \times 0.4$ meters is placed on a perfectly conducting ground. The box has an opening of dimensions 8×12 cm and a conducting wire of a radius $r = 1mm$ is placed at the center of the box with the upper end short-circuited to the box and the lower end terminated with 50Ω. A pulsed plane wave with the electric field polarized parallel to the wire is incident on this box. The transient current in the 50Ω resistance is observed and recorded in Fig 7.2. Results obtained using the FDTD simulation are in good agreement with the experimental result produced by [79].

The second example of the application of FDTD to this type of problem is considered for the configuration shown in Fig. 7.1. A perfectly conducting box of dimensions $0.546 \times 0.546 \times 0.546$ meters is place in free space. A center fed dipole antenna of length 0.156 meter is placed a distance of 1 meter form the center of the conducting box, while a wire of the same length as the dipole antenna is placed at the center of the box with its center loaded by a 50Ω resistor. The wire and the dipole antenna both are assumed to have a radius of $2.6mm$. The box has an opening

in the $x-z$ plane of dimensions 13×7.8 cm. The wire and the space surrounding it are modeled using FDTD. The space cell dimensions used in the modeling of the problem are $2.6 \times 2.6 \times 2.6$ cm, and the box is modeled by assuming the surface tangential components of the electric field to be zero. The small radius wires, the dipole antenna and the wire, are modeled using the contour integral approximation. A Gaussian pulse is used to excite the dipole antenna, and the time step $\Delta t = \Delta/2c$ is used.

In order to get a good understanding of the EMI/EMC relationship three different simulations will be implemented . The first simulation to be implemented, is to model the configuration in Fig. 7.1 without the box. The separation between the antenna and the wire is kept the same as described above. The effect of the dipole antenna presence on the wire is observed in Fig. 7.3, where the current through the 50Ω resistance is recorded. The shielding effect of the conducting box is recorded in Fig. 7.4, again the current through the 50Ω resistance is recorded, and it is clear that the box has reduced the EMI generated by the dipole antenna. Lastly, the slot in the conducting box is covered with a lossy absorbing material. The material has a permittivity $\varepsilon_r = 2.5$ and a conductivity $\sigma = 0.04$. It is evident from Fig. 7.5 that the absorbing material placed at the slot has reduced the coupling effect substantially.

The effect of the shield presence on the degree of electromagnetic interference is needed, this will help in the design of proper enclosures and cabinets. To illustrate this effect, the structure in Fig. 7.1 is modeled without the wire. The same space increments and time stepping is used, then the field, in this case the E_z component,

is observed at a position near the center of the box, for two simulations. In the first simulation the box is removed and the time-domain field response is recorded, see Fig 7.6. Then the same field component is observed at the same position in the presence of the box, Fig 7.7. It is clear from the two figures that the presence of the metallic box has reduced the interference generated from the external source. The frequency response of the two observations is recorded in Fig. 7.8 and Fig. 7.9, respectively. The effect of the shield presence is demonstrated by taking the ratio of $E_z(f)$ with shield and $E_z(f)$ with no shield, the results obtained are provided in Fig. 7.10. One can conclude that the metallic box did provide a good shield except at selected frequencies, thus the designer should avoid having any of these frequencies as the operating frequency in the equipment needed to be enclosed by this specific enclosure.

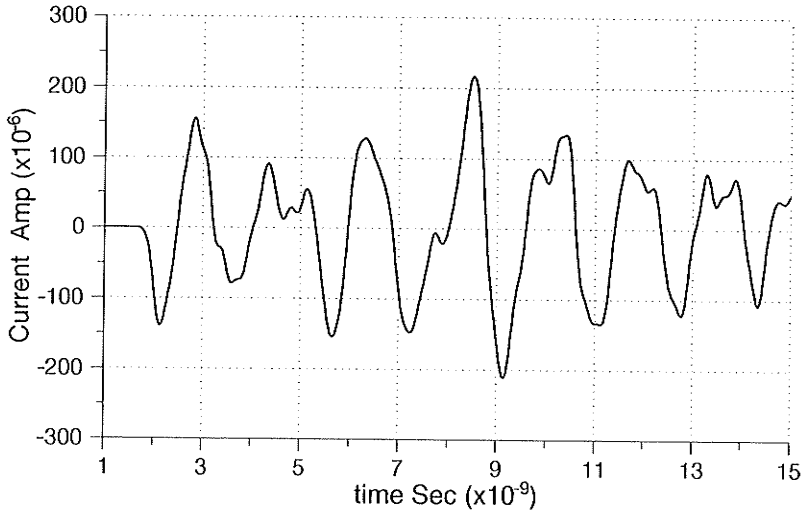

Figure 7.2: Current in the 50Ω resistance due to coupling with the field due to plane wave excitation.

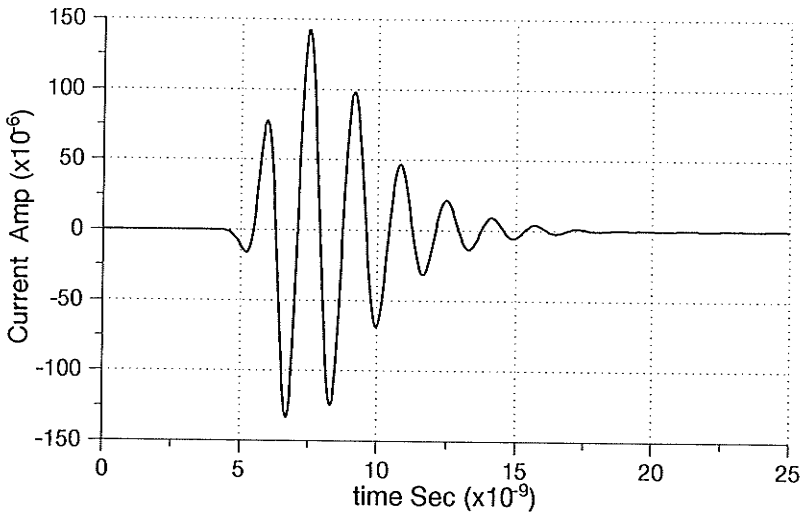

Figure 7.3: Current in the 50Ω resistance due to coupling with the dipole field, with no box.

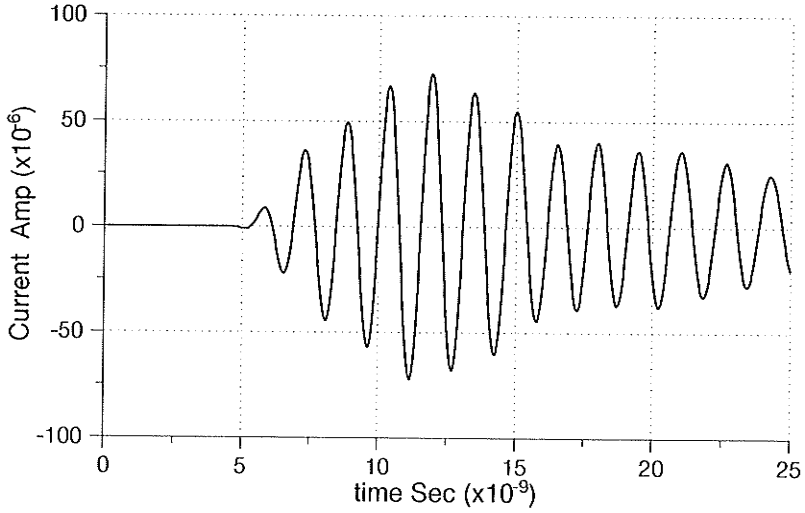

Figure 7.4: Current in the 50Ω resistance due to coupling with the dipole field, with box and slot.

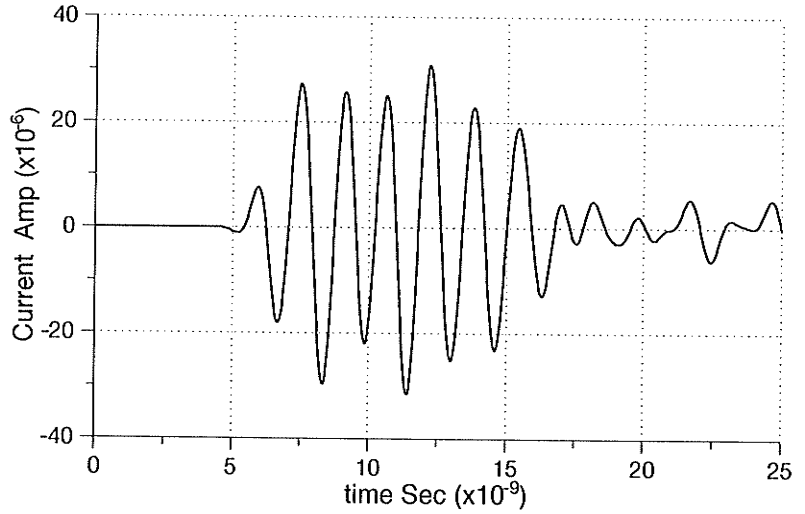

Figure 7.5: Current in the 50Ω resistance due to coupling with the dipole field, with box and slot covered with absorbing material.

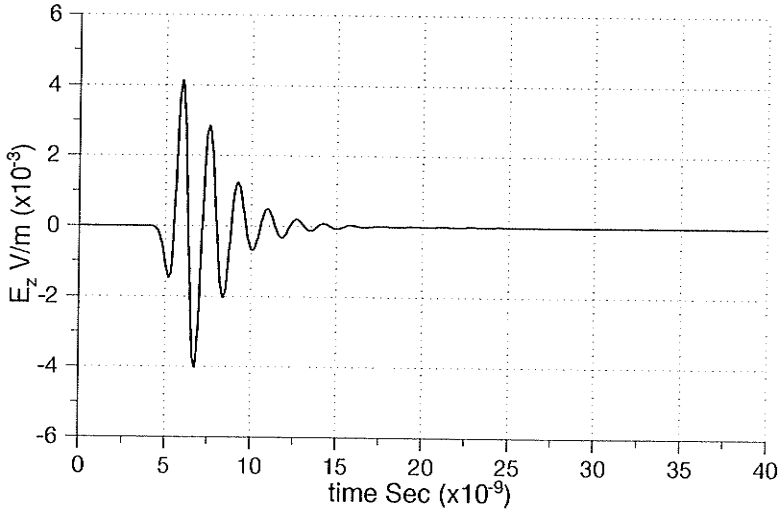

Figure 7.6: Time-domain E_z response near the center of the box position, with no box present.

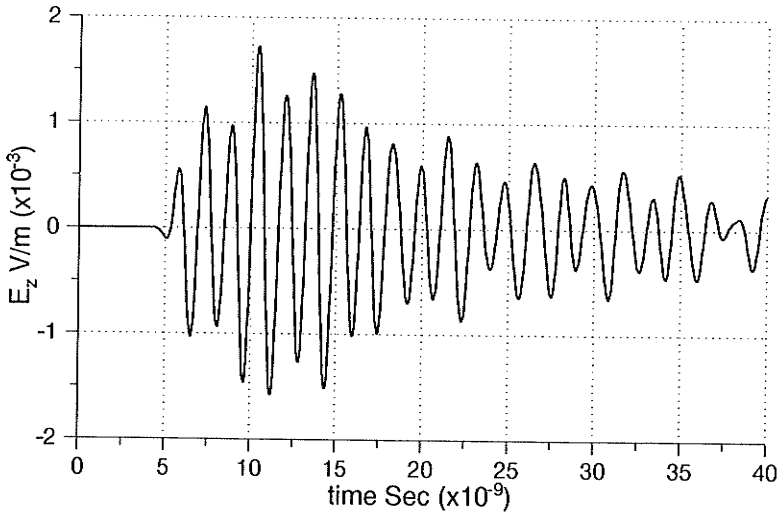

Figure 7.7: Time-domain E_z response near the center inside the box.

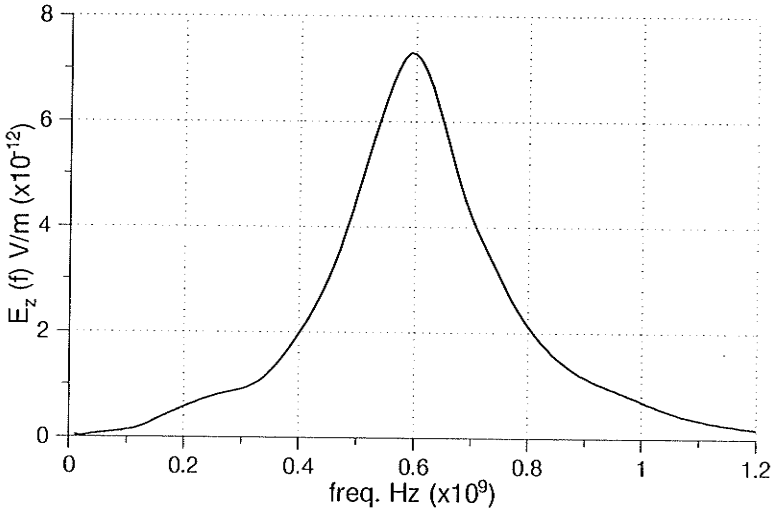

Figure 7.8: Frequency response of the field near the center of the box position, with no box present .

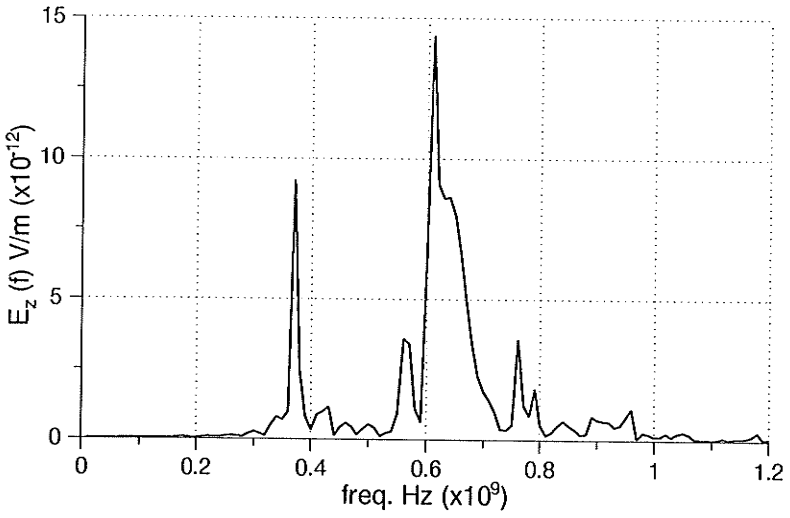

Figure 7.9: Frequency response of the field near the center inside the box.

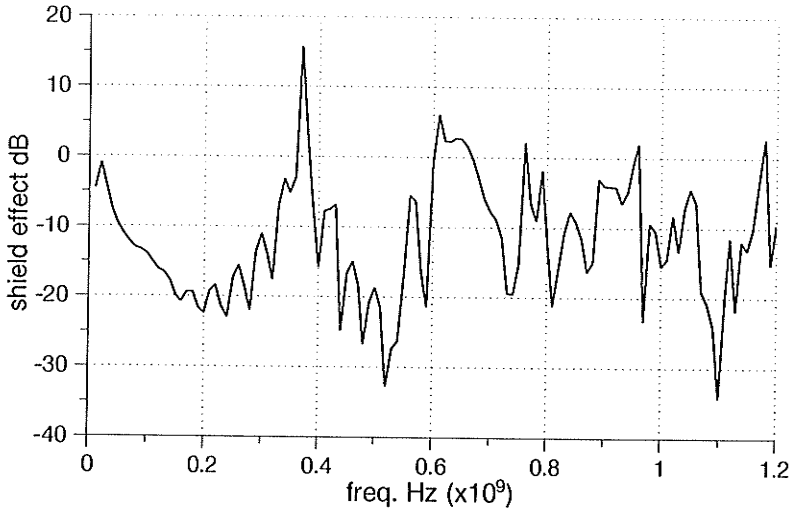

Figure 7.10: Shielding effect of the conducting box with a slot.

7.3 EMC Test Environment

Practical EMC problems possess a great deal of complexity such that it is impossible for an available analytical and numerical technique to handle it without a number of assumptions and simplifications. This in turn requires the verification and validation of a number of careful measurements and tests. Currently the testing of equipment and devices for EMC is necessary both for validation purposes and in order to comply with EMC regulations.

However, EMC testing is not an easy task, actually the complexity is much more involved, since one major requirement is that testing equipment and measuring process should not affect or distorted the measured quantity. This requirement is difficult to meet, especially at high frequencies, where the equipment under test (EUT) and the measurement system form a closely integrated interaction system. Therefore, the equipment and environment of testing must be modeled together with EUT in order to obtain accurate results from the simulation.

7.3.1 Effect of Testing Equipment on EMC Environment

In this section the effect of testing equipment on screened EMC rooms is studied. The screened room dimensions are taken as $2.35 \times 4.55 \times 2.45$ meters. The space is modeled using a FDTD cell of dimensions $\Delta x = \Delta y = \Delta z = 5.0$ cm. The walls of the screened room are assumed perfectly conducting and are modeled by setting the tangential components of the electric field to zero. An impulse E_z field excitation is applied along a line from the floor to the ceiling of the room, 1 m away from one end of the narrow wall. The resonances and the field profile are then obtained for

a number of configurations. First the screened room is considered empty and the resonant frequencies are calculated by observing the E_z component of the electric field near the center of the room. The time domain E_z field is then transformed into frequency domain using Fourier transformation. Fig. 7.11 illustrates the resonance behavior of the screened room. Resonance is observed at, $f = 75.5$, 99.5, 125.5, 200, 223 and $246MHz$, over the range from DC to $250MHz$. The second experiment involves a small measuring dipole of 15 cm length placed one meter a way from the other narrow wall. The resonance behavior of the field inside the room is illustrated in Fig. 7.12. The effect of the small dipole on the amplitude and resonant frequency is almost insignificant compared with Fig. 7.11. However, a significant change in the amplitude and resonant frequency is observed when a dipole of 1 meter length is used, this is demonstrated in Fig. 7.13.

Another important aspect is the effect that the measuring dipole would have on the field profile inside the screened room. To illustrate this, the E_z field strength at the center of the room is obtained over the $x - y$ plane at one of the resonant frequencies. Figure 7.14 illustrates the field behavior at $f = 125MHz$ for an empty room. Figure 7.15 demonstrate the effect of the small dipole on the field profile at the same frequency as the previous case. The field profile of the long dipole is given in Fig. 7.16 at $96MHz$. It is clear from this figure that changes are induced by large dipoles. These effects become more pronounced at higher frequencies.

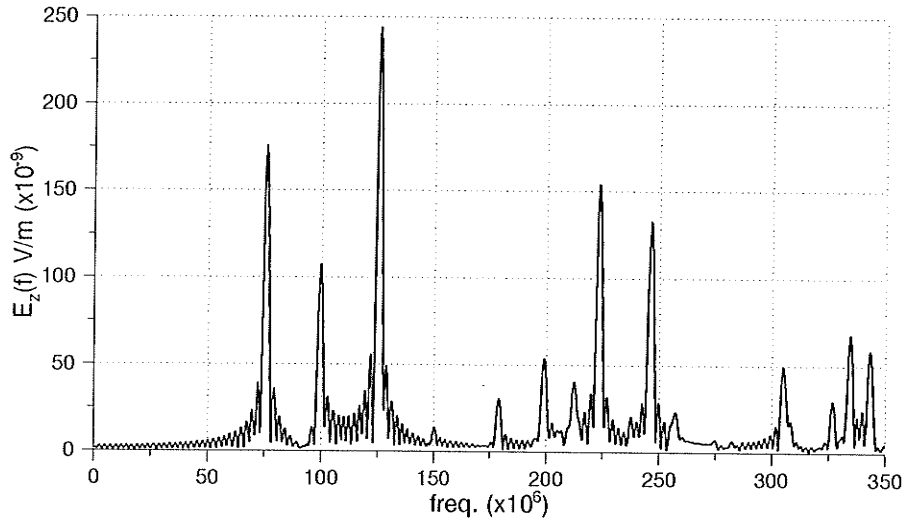

Figure 7.11: Resonance inside a screened empty room.

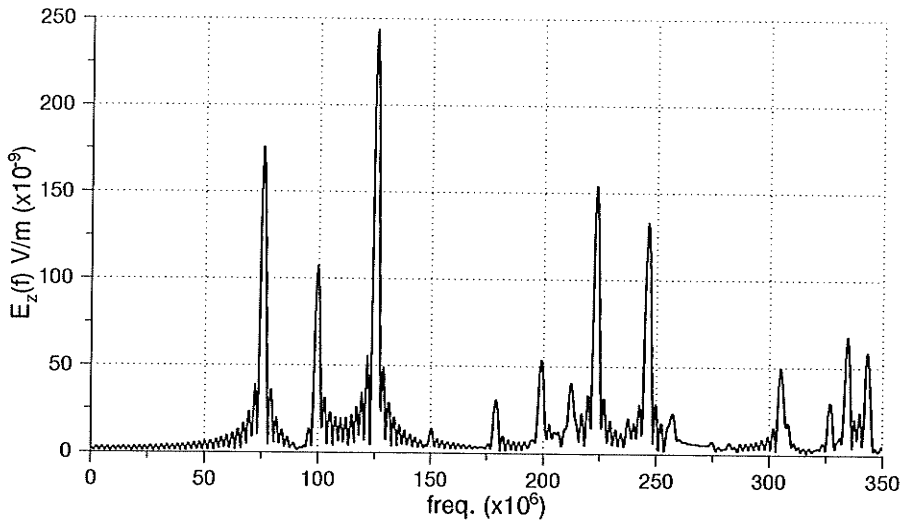

Figure 7.12: Resonance inside a screened room with a $15cm$ long wire.

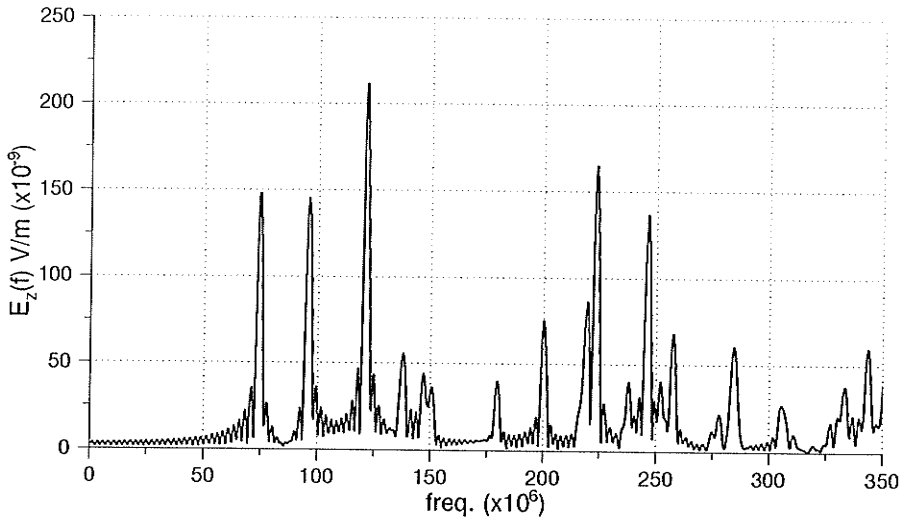

Figure 7.13: Resonance inside a screened room with a $1m$ long wire.

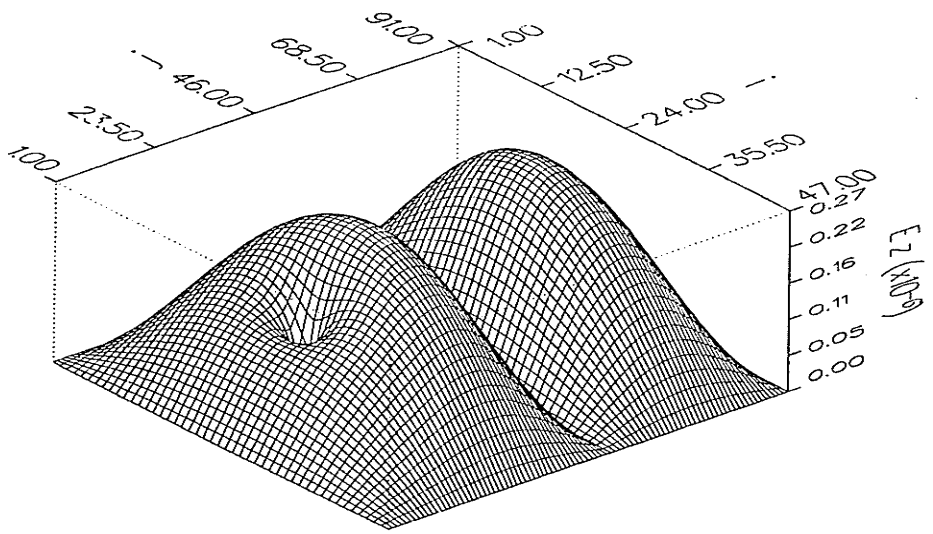

Figure 7.14: E_z profile on a plane midway and parallel to the ground plane for an empty room.

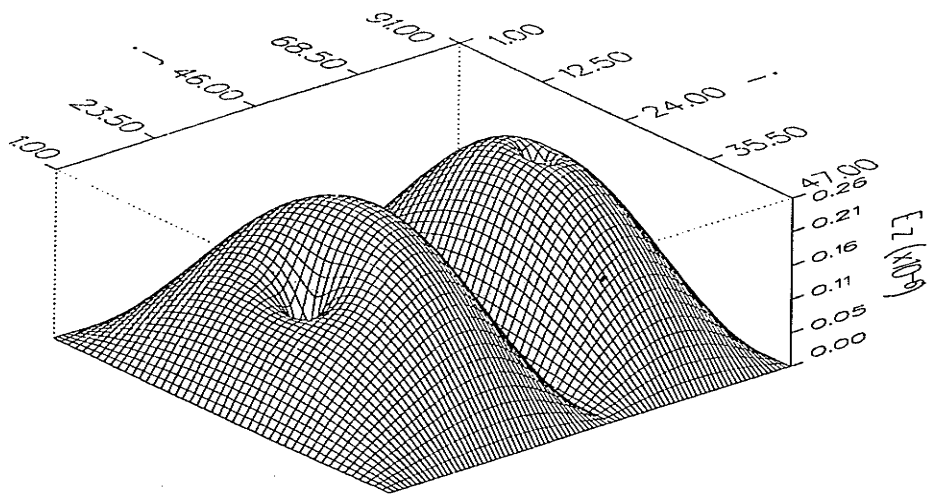

Figure 7.15: E_z profile on a plane midway and parallel to the ground plane for room with small dipole.

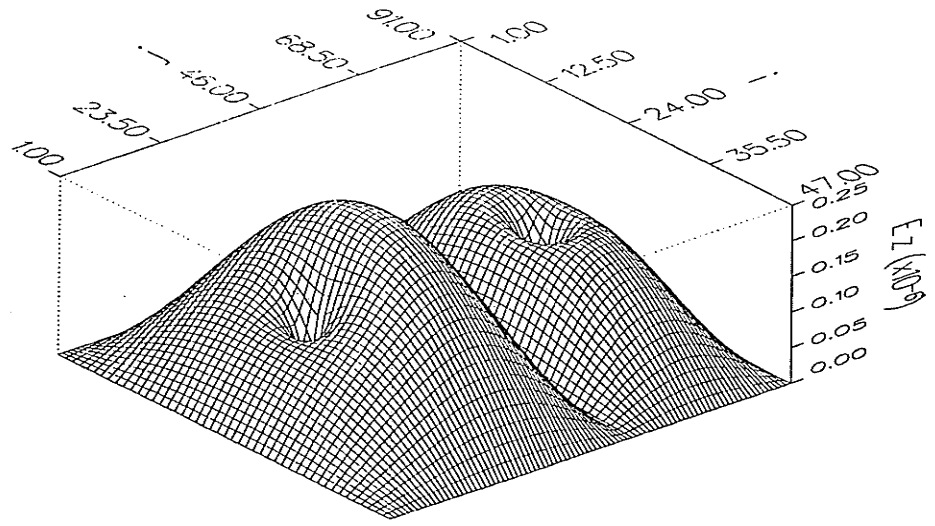

Figure 7.16: E_z profile on a plane midway and parallel to the ground plane for room with long dipole.

7.3.2 Screened and Anechoic Rooms

Practically there are three major EMC test environments which are, an open area test site (OATS), a screened room and an anechoic chamber. However, each of these facilities has some basic drawback. The OATS is neither source nor environmentally controlled. Screened rooms exhibit a strongly resonant behavior at high frequencies, and this complicates the interpretation of measurements. On the other hand the anechoic chamber displays resonant behavior at low frequencies where the effectiveness of the radiation absorbing material (RAM) is limited.

The screened room used for the simulation in this study is of dimensions $4.8 \times 6.1 \times 2.4$ meters. The excitation line is place at the center of the simulation space and the field pattern for the screened room obtained at one of the resonant frequencies, $f = 119MHz$, is shown in Fig. 7.17. It is clear that in this environment and at this frequency any EMC measurement will be highly affected by the position of of the equipment under test (EUT) and measurement equipment due to the resonance behavior of screened room. One way to reduce this effect is to place artificial absorbing boundaries at the walls and the ceiling. Fig. 7.18 illustrates the use of Mur's absorbing boundary conditions at the walls and the ceiling, the floor on the other hand is left as perfectly conducting. It is clear that the field pattern obtained is more representative of an open site condition.

In practice RAM consists of a synthetic material loaded with conducting particles. It is usually shaped in blocks of a conical form and is placed on the walls, floor and ceiling of the screened room. As mentioned earlier, the effectiveness of this material is limited at low frequencies and in order to improve its performance very

thick blocks of RAM are necessary.

The numerical implementation of the RAM can be done based on two assumptions. First, the details of the conical shape were not modeled directly. Instead the RAM is modeled by uniform cubical blocks placed on top of each other with a thickness of 10 cells. Secondly, the electrical properties of the RAM material are assumed constant and do not vary with position. Therefore, in the simulation the RAM is assumed to have a permittivity $\varepsilon_r = 2.5$ and conductivity $\sigma = 0.04$ which correspond to electric resistivity $\rho = 25\Omega m$. Based on these parameters and assumptions, the profile of the electric field E_z is obtained and shown in Fig. 7.19, the room in this case is fully lined with RAM, the peak near the center corresponds to the excitation point and the plot is for the same frequency as in the previous case.

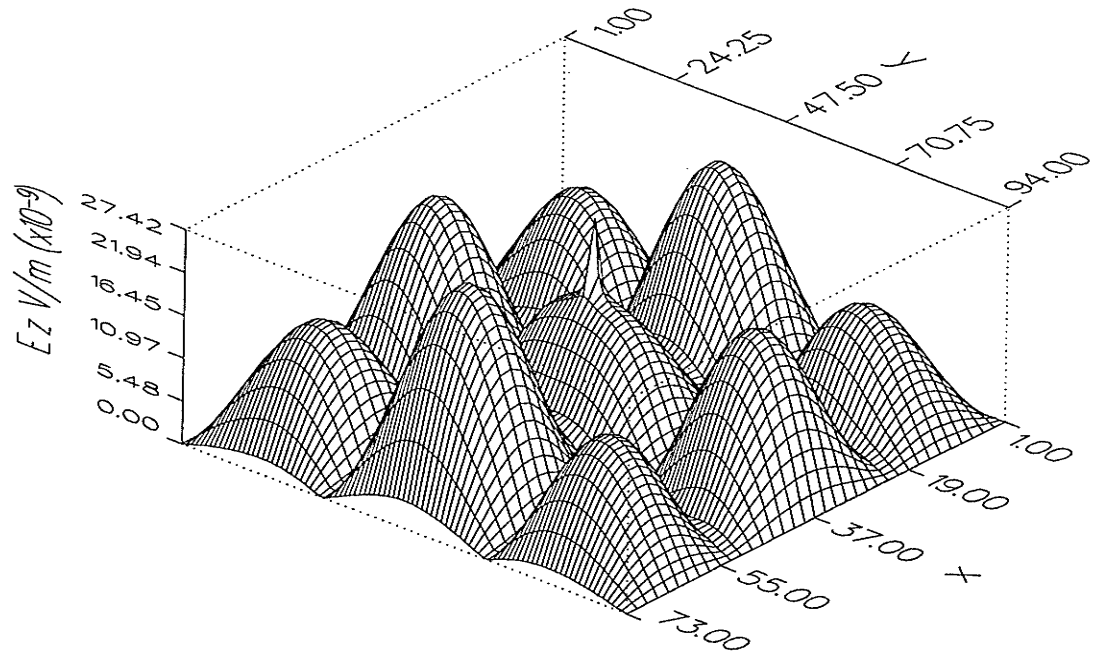

Figure 7.17: E_z field midway a above the ground plane for screened room.

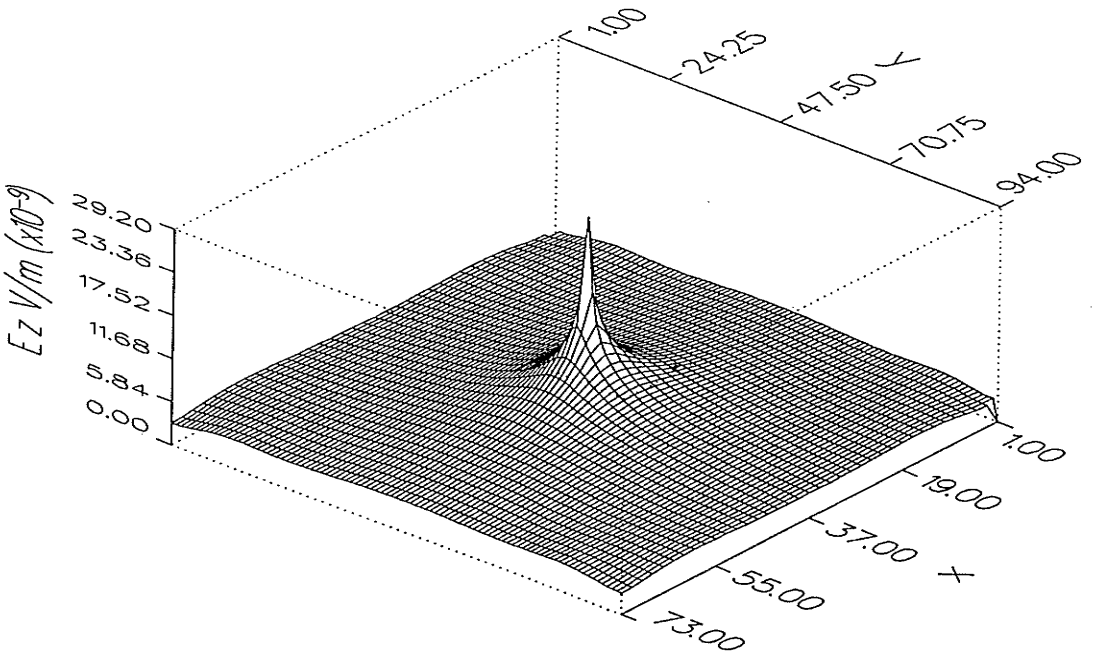

Figure 7.18: E_z field midway a above the ground plane with Mur's absorbing boundaries.

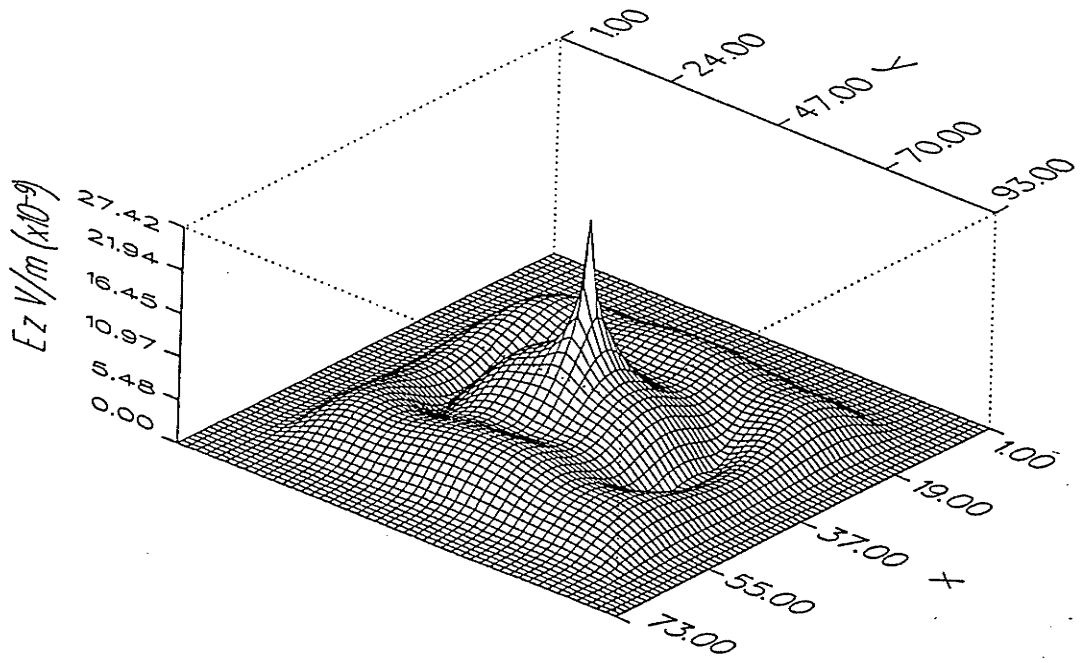

Figure 7.19; E_z field midway a above the ground plane for screened room lined with RAM.

CHAPTER 8

Conclusions and Recommendations

8.1 Conclusions

A review for some of the available numerical techniques has been conducted in an effort to select a suitable approach capable of modeling, simulating and analyzing electromagnetic phenomena. Comparison criteria were based on versatility, accuracy, efficiency and cost.

The FDTD technique offers many advantages as an electromagnetic modeling, simulation and analysis tool. Its capabilities include, arbitrary 3-D modeling, interaction of EM waves with objects of any conductivity and frequency-dependent material. It is capable of predicting any type of response such as scattered field, radiation pattern, radar cross-section, current, penetration and interior coupling. Nevertheless, the FDTD technique is easy to implement.

A key advantage on preferring the use of FDTD over other numerical techniques such as MoM and FE, is its simplicity and ease of implementation. For example, the MoM is regarded as an integral equation technique, which requires the need of using specialized Green's function for each specific problem. These Green's functions are geometry dependent and sometimes are hard to obtain. Nevertheless, the use of MoM or FE techniques usually ends up with a system of matrix equations. This

will add to the complexity of the two techniques. Another important key advantage of using FDTD is its capability of handling time-domain based problems. On the other hand, the MoM and FE techniques have to be modified in order for them to handle such feature, and usually the time dependent terms are treated using the finite difference technique.

The FDTD technique is based on the two Maxwell's curl equations in a derivative form in time-domain. Only nearest-neighbor interaction, interpolation and extrapolation, need to be considered without matrix inversion or integration requirements.

A general 3-D code has been developed based on the Yee cell formulation. The code also uses the contour integral method which is capable of modeling very thin structures such as wires and very narrow apertures. Three outer radiation boundary conditions are studied and employed for open space problems in order to truncate the computational space. The capabilities of the code extend to include the modeling of lumped linear/nonlinear circuit elements both, passive and active. The modeling equations for lumped circuit elements have been derived for passive and active lumped elements. FDTD results have been verified and compared well with circuit theory results.

A general far-field routine has been developed to obtain far field information from FDTD near-field data. The code capabilities have been demonstrated through several electromagnetic applications including 3-D scattering by conducting and dielectric objects. In the area of antenna radiation, three antenna configurations have been modeled. These are a monopole mounted on a conducting box, a bent-slot antenna flush-mounted on a conducting box and a quarter-wavelength monopole

mounted on an automobile's roof. Radiation pattern results obtained for the three configurations are in a very good agreement with published results.

Furthermore, the capabilities of the FDTD technique in modeling planar microstrip circuits have been demonstrated via the calculation of a microstrip line effective dielectric constant and its characteristic impedance. The code has been successfully used to model line-fed microstrip patch and aperture coupled microstrip patch antennas.

In the area of EMI/EMC, the code has been used to study electromagnetic coupling with wires inside shielded enclosure. The shielding effect of a metallic cabinet and an enclosure has been obtained. Simulation and testing of the EMC test environment has been studied by simulating open-sight, screened rooms, and screened rooms lined with radiation absorbing materials (RAM). The capability of the FDTD to model EMI/EMC problems makes it a potential substitute to the available expensive EMC test sites and environments.

8.2 Recommendations

The FDTD technique has been developed, tested and applied successfully to several electromagnetic problems, however, still there are several areas which need to be investigated and improved. Potential areas of improvement can be summarized as follows:

- Investigation of the application of more accurate numerical RBC is one potential area for improving the accuracy of the FDTD code. A successful RBC

will result in a reduction of memory and time requirements of simulations.

- A second important area which would improve the capabilities and the accuracy of the FDTD technique is the use of hybrid techniques, *i.e.*, mixed FDTD and MoM, or FDTD and boundary element (BEM). Such implementation will eliminate the need of RBC.

- Another area which will lead to an improvement in the capabilities of the FDTD is the use of conformed cells in place of the traditional Yee's cubic cells. One suggestion is the use of the FE conformed cell. Such development will improve the capability of the FDTD in modeling complex and arbitrary structures.

Nevertheless, the current FDTD code could be used to investigate and study more advanced electromagnetic problems such as,

- The effect and the hazard of electromagnetic waves on biological tissues and structures.

- Electromagnetic interference and cross-talk in printed circuit boards and VLSI interconnects.

- The use of circuit simulators such as SPICE, to model complex lumped circuit elements which could be integrated with the FDTD code.

REFERENCES

[1] J. H. Richmond. "Digital computer solution of the rigorous equations for scattering problems". *IEEE Proc.*, vol. 57, pp. 796, 1965.

[2] J. H. Richmond. "A wire-grid model for scattering by conducting bodies". *IEEE Trans. Antennas Propagat.*, vol. 14, pp. 782, 1966.

[3] R. F. Harrington. "Matrix method for field problems". *IEEE Proc.*, vol. 55, pp. 136, 1967.

[4] R. F. Harrington. *"Field Computation by Moment Methods"*. Macmillan, New York, 1968.

[5] J. B. Keller. "Geometrical theory of diffraction". *J. Opt. Soc. Am.*, vol. 52, pp. 116, 1962.

[6] S. A. Davidson and G. A. Thiele. "A hybrid method of moments-GTD technique for computing electromagnetic coupling between two monopole antennas on a large cylindrical surface". *IEEE Trans. Electromagn. Compat.*, vol. 26, pp. 90–97, 1984.

[7] R. Gomez, A. Salinas, A. Rubio Bretores, and M. Martin. "Time-domain integral equation for EMP analysis transmission-line system". *Int. J. Num. Mod.*, vol. 4, pp. 153–162, 1991.

[8] C. E. Baum. *"The singularity expansion method"*. in Topics in Applied Physics, vol 10: Transient Electromagnetic Fields. L. B. Felsen, Spring-Verlag, New York, 1976.

[9] S. K. Chang and K. Mei. "Application of unimoment method to electromagnetic scattering of dielectric cylinder". *IEEE Trans. Antennas Propagat.*, vol. 24, pp. 35, 1976.

[10] S. Castillo, Z. Pantiac, and R. Mittra. "Finite-element analysis of multiconductor printed-circuit transmission-line system". *Int. J. Num. Math. Engrg.*, vol. 29, pp. 1033–1047, 1980.

[11] D. E. Merewether and R. Fisher. "Finite-difference analysis of EM fields inside complex cavities driven by large apertures". *IEEE Trans. Electromagn. Compat.*, vol. 24, pp. 406–410, 1982.

[12] M. J. Beaubien and A. Wexler. "An accurate finite-difference method for higher order waveguide modes". *IEEE Trans. Microwave Theory Techniques*, vol. 16, pp. 1007–1017, 1968.

[13] A. Cangellar, C. lin, and K. Mei. "Point-matched time-domain finite-element method for electromagnetic radiation and scattering". *IEEE Trans. Antennas Propagat.*, vol. 35, pp. 1160–1173, 1987.

[14] S. Akhtarzad and P. B. Johns. "Solution of Maxwell's equations in three space dimensions and time by the TLM method of numerical analysis". *Proc. IEE*, vol. 122, pp. 1344–1348, 1975.

[15] A. Fettweis. "Multidimensional wave digital filters for discrete-time modelling of Maxwell's equations". *Int. J. Num. Mod.*, vol. 5, pp. 183–201, 1992.

[16] K. Yee. "Numerical solution of initial value problems involving Maxwell's equations in isotropic media". *IEEE Trans. Antennas Propagat.*, vol. 14, pp. 302–307, 1966.

[17] A. Taflove and K. Umashankar. "Review of FD-TD numerical modeling of electromagnetic wave scattering and radar cross section". *IEEE Proc.*, vol. 77, pp. 682–699, 1989.

[18] A. Taflove and K. Umashankar. "The finite-difference time-domain method for numerical modeling of electromagnetic wave interactions". *Electromagn.*, vol. 10, pp. 105–126, 1990.

[19] P. A. Tirkas and K. R. Demarest. "Modeling thin dielectric structures using the finite-difference time-domain techniques". *IEEE Trans. Antennas Propagat.*, vol. 39, pp. 1338–1344, 1991.

[20] C. L. Britt. "Solution of electromagnetic scattering problems using time domain techniques". *IEEE Trans. Antennas Propagat.*, vol. 37, pp. 1181–1192, 1989.

[21] A. Taflove, K. Umashankar, B. Beker, F Harfush, and K. Yee. "Detailed FD-TD analysis of electromagnetic fields penetrating narrow slots and lapped joints in

thick conducting screens". *IEEE Trans. Antennas Propagat.*, vol. 36, pp. 247–257, 1988.

[22] K. Demarest. "A finite-difference time-domain technique for modeling narrow apertures in conducting scatterers". *IEEE Trans. Antennas Propagat.*, vol. 35, pp. 826–831, 1987.

[23] D. J. Riley and C. D. Turner. "Hybrid this-slot algorithm for the analysis of narrow appertures in finite-difference time-domain calculations". *IEEE Trans. Antennas Propagat.*, vol. 38, pp. 1943–1950, 1990.

[24] J. A. Shaw, H. D. Durney, and D. A. Cristensen. "Computer-aided design of two-dimensional electric-type hyperthermia applicators using the finite-difference time-domain method". *IEEE Trans. Biomed. Eng.*, vol. 38, pp. 861–870, 1991.

[25] P. J. Dimbylow. "Finite-difference time-domain calculations of absorbed power in the ankle for 10-100 MHz plane wave exposure". *IEEE Trans. Biomed. Eng.*, vol. 38, pp. 423–428, 1991.

[26] D. M. Sullivan. "Mathematical methods for treatment planning in deep regional hyperthermia". *IEEE Trans. Microwave Theory Techniques*, vol. 39, pp. 864–872, 1991.

[27] J. Gilbert and R. Holland. "Implementation of the thin-slot formalism in the finite-difference EMP code TREDII". *IEEE Trans. Nuclear Sci.*, vol. 28, pp. 4589–4591, 1981.

[28] R. Holland and L. Simpson. "Finite difference analysis of EMP coupling to thin struts and wires". *IEEE Trans. Electromagn. Compat.*, vol. 23, pp. 88–97, 1981.

[29] R. Holland, L. Simpson, and K. S. Kunz. "Finite difference analysis of EMP coupling to lossy dielectric structures". *IEEE Trans. Electromagn. Compat.*, vol. 22, pp. 203–209, 1980.

[30] K. S. Kunz and K. Lee. "A three-dimensional finite-difference solution of the external response of an aircraft to a complex transient EM environment: Part

I–The method and its implementation". *IEEE Trans. Electromagn. Compat.*, vol. 20, pp. 328–333, 1978.

[31] K. S. Kunz and K. Lee. "A three-dimensional finite-difference solution of the external response of an aircraft to a complex transient EM environment: Part II–Comparison of predictions and measurements". *IEEE Trans. Electromagn. Compat.*, vol. 20, pp. 333–341, 1978.

[32] J. F. Lee, R. Palandech, and R. Mittra. "Modeling three-dimensional discontinuities in waveguides using nonorthogonal FDTD algorithm". *IEEE Trans. Microwave Theory Techniques*, vol. 40, pp. 346–352, 1992.

[33] X. Zhang, J. Fang, K. Mei, and Y. Liu. "Calculation of the dispersive characteristics of microstrips by the time-domain finite-difference method". *IEEE Trans. Microwave Theory Techniques*, vol. 36, pp. 263–267, 1988.

[34] T. G. Jurgens, A. Taflove, K. Umashankar, and T. G. Moore. "Finite-difference time-domain modeling of curved surfaces". *IEEE Trans. Antennas Propagat.*, vol. 40, pp. 357–366, 1992.

[35] A. Reineix and B. Jecko. "Analysis of microstrip patch antennas using finite-difference time-domain method". *IEEE Trans. Antennas Propagat.*, vol. 37, pp. 1361–1369, 1989.

[36] D. M. Sheen, S. M. Ali, M. D. Abouzehra, and J. A. Kong. "Application of the three- dimensional finite-difference time-domain method to the analysis of planar microstrip circuits". *IEEE Trans. Microwave Theory Techniques*, vol. 38, pp. 849–857, 1990.

[37] J. G. Maloney, G. S. Smith, and W. R. Scott. "Accurate computation of the radiation from simple antennas using the finite-difference time-domain method". *IEEE Trans. Antennas Propagat.*, vol. 38, pp. 1059–1068, 1990.

[38] D. S. Kats, M. J. Picket-May, A. Taflove, and K. Umashankar. "FDTD analysis of electromagnetic radiation from system containing horn antennas ". *IEEE Trans. Antennas Propagat.*, vol. 39, pp. 1203–1212, 1991.

[39] P. Tirkas and C. Balanis. "Finite-Difference time-domain method for antenna radiation". *IEEE Trans. Antennas Propagat.*, vol. 40, pp. 334–340, 1992.

[40] M. Hussein and A. Sebak. "Application of the Finite-Difference Time-Domain Method to the Analysis of Mobile Antennas". *Accepted for publication at IEEE Trans. Vehicular Technology*, 1995.

[41] R. Holland. "Finite-difference solution of Maxwell's equations in generalized nonorthogonal coordinates". *IEEE Trans. Nuclear Sci.*, vol. 30, pp. 4589–4591, 1983.

[42] M. Fusco. "FDTD algorithm in curvilinear coordinates". *IEEE Trans. Antennas Propagat.*, vol. 38, pp. 76–89, 1990.

[43] V. Shankar, W. Hall, and A. Mohammadian. "A time-domain differential solver for electromagnetic scattering problems". *IEEE Proc.*, vol. 77, pp. 709–721, 1989.

[44] V. Shankar, A. Mohammadian, and W. Hall. "A time-domain finite-volume treatment for the Maxwell's equations ". *Electromagn.*, vol. 10, pp. 127–145, 1990.

[45] N. K. Madsen and R. W. Ziolkowski. "Numerical solution of Maxwell's equations in the time domain using irregular nonorthogonal grids". *Wave Motion*, vol. 10, pp. 583–596, 1988.

[46] N. K. Madsen and R. W. Ziolkowski. "A three-dimensional modified finite volume technique for Maxwell's equations". *Electromagn.*, vol. 10, pp. 147–161, 1990.

[47] R. Holland, V. Cable, and L. Wilson. "Finite-volume time-domain (FVTD) technique for EM scattering". *IEEE Trans. Electromagn. Compat.*, vol. 33, pp. 281–294, 1991.

[48] T. G. Jurgens and A. Taflove. "Three-dimensional contour FDTD modeling of scattering from single and multiple bodies". *IEEE Trans. Antennas Propagat.*, vol. 41, pp. 1703–1708, 1993.

[49] W. Sui, D. A. Christensen, and C. H. Durney. "Extending the two-dimensional FDTD method to hybrid electromagnetic systems with active and passive lumped elements". *IEEE Trans. Microwave Theory Techniques*, vol. 40, pp. 724–730, 1992.

[50] K. A. Chamberlin, J. D. Morrow, and R. J. Luebbers. "Frequency-domain and finite-difference time-domain solution to a nonlinearally-terminated dipole: Theory and validation". *IEEE Trans. Electromag. Compat.*, vol. 34, pp. 416–422, 1992.

[51] M. Hussein and A. Sebak. "Modeling of antennas with lumped impedance loading using FDTD". In *Proc. Antenna Technology and Applied Electromagnetics Symp., ANTEM 94*, pp. 362–365, August 1994.

[52] M. Piket-May, A. Taflove, and J. Baron. "FD-TD modeling of digital signal propagation in 3-D circuits with passive and active loads". *IEEE Trans. Microwave Theory Techniques*, vol. 42, pp. 1514–1523, 1994.

[53] K. Kunz and R. Luebbers. *"Finite difference time domain method for electromagnetics"*. CRC Press, Boca Raton, FL, 1993.

[54] G. Mur. "Absorbing boundary conditions for the finite-difference approximation of the time-domain electromagnetic field equations". *IEEE Trans. Electromag. Compat.*, vol. 23, pp. 377–382, 1981.

[55] C. Furse, S. Mathur, and OM P. Gandhi. "Improvements to finite-difference time-domain method for calculating the radar cross section of a perfectly conducting target". *IEEE Trans. Microwave Theory Techniques*, vol. 38, pp. 919–927, 1990.

[56] A. Taflove and K. Umashankar. "Radar cross section of general three-dimensional structures". *IEEE Trans. Electromag. Compat.*, vol. 25, pp. 433–440, 1983.

[57] A. Taflove and M. Brodwin. "Numerical solution of steady state electromagnetic scattering problems using the time-dependent Maxwell's equations". *IEEE Trans. Microwave Theory Techniques*, vol. 23, pp. 623–630, 1975.

[58] J.-P Berenger. "Aperfectly matched layer for the absorbtion of electromagnetic waves". *In press, J. Computational Phys.*, 1994.

[59] D. S. Katz, E. T. Thiele, and A. Taflove. "Validation and extension to three dimensions of the Berenger PML absorbing boundary boundary condition for FD-TD meshes". *IEEE Micr. Guid. Lett.*, vol. 4, pp. 268–270, 1994.

[60] B. Engqist and A. Majda. "Absorbing boundary conditions for the numerical simulation of waves". *Math. Comput.*, vol. 31, pp. 629–651, 1977.

[61] T. Moore, J. Blaschak, A. Taflove, and G. Kriegsmann. "Theory and application of radiation boundary operators". *IEEE Trans. Antennas Propagat.*, vol. 36, pp. 1797–1811, 1988.

[62] P. Tirkas and C. Balanis. "Higher order absorbing boundary condition for the finite-difference time-domain method". *IEEE Trans. Antennas Propagat.*, vol. 40, pp. 1215–1222, 1992.

[63] L. N. Trefethen and L. Halpern. "Well-posedness of one-way wave equation and absorbing boundary conditions". *Math. Comput.*, vol. 47, pp. 421–435, 1986.

[64] Kenneth K. Mei and J. Fang. "Superabsorption–a method to improve absorbing boundary conditions". *IEEE Trans. Antennas Propagat.*, vol. 40, pp. 1001–1010, 1992.

[65] S. A. Schelkunoff. "Field equivalence theorems". *Commun. Pure Appl. Math.*, vol. 4, pp. 43–59, 1951.

[66] R. F. Harrington. *"Time Harmonic Electromagnetic Fields"*. McGraw Hill, New York, 1961.

[67] H. Kuboyama, K. Fujimoto, and K. Hirasawa. "UHF bent-slot antenna system for portable equipment-I". *IEEE Trans. Vehicular Technology*, vol. 36, pp. 78–85, 1987.

[68] K. Nishikawa and Y. Asano. "Vertical radiation patterns of mobile antenna in UHF band". *IEEE Trans. Vehicular Technology*, vol. 35, pp. 57–62, 1986.

[69] K. L. Wu, M. Spenuk, J. Litva, and D. G. Fang. "Theoretical and experimental study of feed network effects on the radiation pattern of series-fed microstrip antenna arrays". *Inst. Elect. Eng. Proc.*, vol. 138, pp. 238–242, 1991.

[70] D. M. Pozar. "Microstrip antenna aperture-coupled to a microstrip-line". *Electron. Lett.*, vol. 21, pp. 49–50, 1985.

[71] X. Zhang and K. Mei. "Time-domain finite-difference approach to the calculation of the frequency-dependent characteristics of microstrip discontinuities". *IEEE Trans. Microwave Theory Techniques*, vol. 36, pp. 1775–1787, 1988.

[72] C. Wu, K. L. Wu, Z. Q. Bi, and J. Litva. "Accurate characterization of planar printed antennas using finite-difference time-domain method". *IEEE Trans. Antennas Propagat.*, vol. 40, pp. 526–534, 1992.

[73] Z. Q. Bi, K. L. Wu, C. Wu, and J. Litva. "A dispersive boundary condition for microstrip components analysis using FD-TD method". *IEEE Trans. Microwave Theory Techniques*, vol. 40, pp. 774–777, 1992.

[74] J. Fang. "Absorbing boundary conditions applied to model wave propagation in microwave integrated-circuits". *IEEE Trans. Microwave Theory Techniques*, vol. 42, pp. 1506–1513, 1994.

[75] N. Simmons. *Development and application of differential-equation based numerical techniques to electromagnetic scattering and radiation problems.* PhD dissertation, University of Manitoba, Electrical and Computer Engineering Department, May 1994.

[76] J. R. James and P. S. Hall. *"Handbook of Microstrip Antennas"*. IEE, London, 1989.

[77] M. Himdi, J. P. Daniel, and C. Terret. "Analysis of aperture-coupled microstrip antenna using cavity method". *Electron. Lett.*, vol. 25, pp. 391–392, 1989.

[78] L. B. Gravelle and P. F. Wilson. "EMI/EMC in printed circuit boards- a literature review". *IEEE Trans. Electromagn. Compat.*, vol. 34, pp. 109–116, 1992.

[79] J. Herring, P. Naylor, and C. Christopoulos. "Transmission-line modeling in electromagnetic compatibility studies". *Int. J. Num. Mod.*, vol. 4, pp. 143–152, 1991.

[80] B. Keiser. *"Principles of electromagnetic compatibility"*. Artech House, MA USA, 1987.

APPENDICES

APPENDIX A

Realtion of Electric and Magnetic Fields for RBC Application

To study the relation between the electric and magnetic field components assume that the electric and magnetic components are of the following form:

$$E_u = E_{u0} e^{\hat{j}(\omega n\Delta t - k_x i\Delta - k_y j\Delta)} \tag{A.1}$$

$$H_v = H_{v0} e^{\hat{j}(\omega n\Delta t - k_x i\Delta - k_y j\Delta)} \tag{A.2}$$

where the subscripts u and v corresponds to x, y, or z components, and $\hat{j} = \sqrt{-1}$. Assuming the problem under consideration is a TM $2-D$, thus, one can assume $E_x = E_y = 0$ and $H_z = 0$. Upon substituting (A.1) and (A.2) into the difference equations (3.22) and (3.23), the following relations will be obtained.

$$H_x \sin \omega\Delta t/2 = c_2 E_z \sin k_y \Delta/2 \tag{A.3}$$

$$H_y \sin \omega\Delta t/2 = -c_2 E_z \sin k_x \Delta/2 \tag{A.4}$$

Therefore,

$$\frac{H_x}{E_z} = \frac{c_2 \sin k_y \Delta/2}{\sin \omega\Delta t/2} \tag{A.5}$$

and

$$\frac{H_y}{E_z} = -\frac{c_2 \sin k_x \Delta/2}{\sin \omega \Delta t/2} \tag{A.6}$$

Similarly for the TE case where $H_x = H_y = E_z = 0$ the following relations are obtained,

$$\frac{E_x}{H_z} = -\frac{c_1 \sin k_y \Delta/2}{\sin \omega \Delta t/2} \tag{A.7}$$

and

$$\frac{E_y}{H_z} = \frac{c_1 \sin k_y \Delta/2}{\sin \omega \Delta t/2} \tag{A.8}$$

The signs on the right hand side of (A.5), (A.6), (A.7) and (A.8) may change for wave propagating in the other directions, such as if the wave is assumed to have the following expression,

$$E_u = E_{u0} e^{\hat{j}(\omega n \Delta t + k_x i \Delta - k_y j \Delta)} \tag{A.9}$$

$$H_v = H_{v0} e^{\hat{j}(\omega n \Delta t + k_x i \Delta - k_y j \Delta)} \tag{A.10}$$

then

$$\frac{H_y}{E_z} = \frac{c_2 \sin k_x \Delta/2}{\sin \omega \Delta t/2} \tag{A.11}$$

for TM waves propagating in the (-) x direction.

APPENDIX B

Discrete Fourier Transformation

The magnitude and phase of the envelope of pulsed FDTD are determined by taking the discrete Fourier transform of the time-domain waveform. The discrete Fourier transform (DFT) is given by

$$G(k\Delta f) = \Delta t \sum_{n=0}^{N-1} g(n\Delta t) e^{\left(\frac{-j2\pi kn}{N}\right)} \qquad k = 0, 1, 2, \cdots, NF \tag{B.1}$$

Where $g(n\Delta t)$ is the discrete time-domain field value (from FDTD), n is the time step index, N is the length of the DFT (number of available frequencies), Δf is the frequency resolution, and k is the frequency index. j is complex number, $j = \sqrt{-1}$.

The magnitude and phase of $G(k\Delta f)$ are equivalent to the magnitude and phase of the steady-state envelope for frequency $F = k\Delta f$. The summation in (B.1) is updated at every FDTD time step, and the final values are normalized by the DFT of the incident pulse. The complex value $G(k\Delta f)$ must be stored for every field components at each frequency of interest and at every cell where the frequency response is calculated. For single frequency calculation, the storage overhead for pulsed FDTD is smaller than for continuous wave (CW) FDTD. The overhead for pulsed FDTD increases linearly with the number of frequencies.

It is worth noting that the DFT algorithm is more efficient than the fast Fourier transform (FFT) algorithm for computing the frequency response from pulsed FDTD when only a limited number of available frequencies are of interest. Since N must always be greater or equal to the number of FDTD time steps, therefore, in all far-field computation N is taken equal to the FDTD time step.